NUMERICAL SIMULATION OF NONLINEAR RAYLEIGH WAVE BEAMS EVALUATING DIFFRACTION, ATTENUATION AND REFLECTION EFFECTS IN NON-CONTACT MEASUREMENTS

A Thesis
Presented to
The Academic Faculty

by

Matthias P. Uhrig

In Partial Fulfillment
of the Requirements for the Degree
Master of Science in
Engineering Science and Mechanics in the
School of Civil and Environmental Engineering

Georgia Institute of Technology
December 2015

NUMERICAL SIMULATION OF NONLINEAR RAYLEIGH WAVE BEAMS EVALUATING DIFFRACTION, ATTENUATION AND REFLECTION EFFECTS IN NON-CONTACT MEASUREMENTS

Approved by:

Professor Laurence J. Jacobs, Advisor
School of Civil and Environmental Engineering
Georgia Institute of Technology

Dr. Jin-Yeon Kim
School of Civil and Environmental Engineering
Georgia Institute of Technology

Dr. Jianmin Qu
Department of Civil and Environmental Engineering
Northwestern University

Date Approved: 21. August 2015

ACKNOWLEDGEMENTS

There are a lot of people I would like to thank for their support in the writing of my thesis. First of all I want to thank my advisor Professor Laurence J. Jacobs for his help. His great ideas during my thesis work as well as his open ear to study related questions was very helpful during my time in Atlanta. On top of that, he enabled me to participate in the QNDE conference held in Minneapolis, MN, which was an outstanding experience during my personal academic career.

Furthermore I want to thank Dr. Jin-Yeon Kim for his professional and profound advise concerning any technical questions in the field of wave propagation.

I also want to thank Professor Lothar Gaul and Christian Ehrlich of the University of Stuttgart, who gave me the chance to participate in the ISAP exchange program with the Georgia Institute of Technology.

Additionally I am very grateful for the financial support of the Deutscher Akademischer Austauschdienst (DAAD) and the Studienstiftung des Deutschen Volkes.

Last but not least I want to thank my family who exceptionally supported me during the last years.

Contents

ACKNOWLEDGEMENTS . . . . . **iii**

LIST OF TABLES . . . . . **vii**

LIST OF FIGURES . . . . . **viii**

LIST OF SYMBOLS AND ABBREVIATIONS . . . . . **xiv**

SUMMARY . . . . . **xv**

I INTRODUCTION **1**

1.1 Motivation and Objective 1

1.2 Outline 2

II THEORY **4**

2.1 Linear Wave Propagation 4

2.1.1 Linear Elastodynamics in an Unbounded Medium 4

2.1.2 Plane Waves 6

2.1.3 Reflection and Transmission of Ultrasonic Waves 7

2.1.4 Rayleigh Waves 9

2.2 Nonlinear Wave Propagation 11

2.2.1 Nonlinear Elastodynamics in an Unbounded Medium 11

2.2.2 Nonlinear Rayleigh Wave Beams 13

2.3 Leaky Rayleigh Waves 16

2.3.1 Formation of Plane Angled Pressure Waves 16

2.3.2 Attenuation of Pressure Waves in Air 18

III NONLINEAR AIR-COUPLED RAYLEIGH WAVE MEASUREMENTS **20**

3.1 Experimental Setup 20

3.1.1 Components 20

3.2 Generation of Experimental Results 25

3.2.1 Calibration 25

3.2.2 Relative Nonlinearity Parameter β' 26

IV MODELING 27

4.1 Overview 27

4.2 Geometry 28

4.2.1 Wedge Geometry 28

4.2.2 Specimen Geometry 28

4.2.3 Fluid Volume Geometry 29

4.3 Preprocessing 30

4.3.1 Element Selection and Meshing 30

4.3.2 Loading and Boundary Conditions 32

4.3.3 Material Properties 36

4.4 Solving 39

4.4.1 Time Increments 39

4.4.2 Explicit Procedure 39

4.4.3 Hardware and Computation 40

4.5 Post Processing 40

4.5.1 Graphical Presentation of Output Data 40

4.5.2 Material Model and Excitation Source Optimization 42

V RESULTS AND DISCUSSION 44

5.1 Numerical Description of Fluid-Structure Interaction 44

5.1.1 Simulation of an Air-Column 44

5.1.2 Pressure Distribution at the Active Receiver Surface 47

5.2 Experimental Considerations 49

5.2.1 Amplitude Progression 49

5.2.2 Diffraction 54

5.3 Influence of the Air-Coupled Receiver 55

5.3.1 Transformation into the Receiver “Perspective” 56

5.4 Numerical Description of Nonlinear Rayleigh Waves 60

5.4.1 Experimental Validation 60
5.4.2 Influence of the Specimen Width 64
VI CONCLUSION AND FUTURE WORK 76
6.1 Conclusion 76
6.2 Future Work 77
Appendix A — MODELING DETAILS 79
Appendix B — ADDITIONAL RESULTS 82
REFERENCES 85

List of Tables

4.1 Linear elastic material properties of solid components 37

4.2 Material properties of air 37

5.1 Results of the coupled structural acoustic analysis and comparison to analytical values 47

List of Figures

2.1 Reflection and transmission of waves at a solid-solid interface for an incident P-wave . . . 7

2.2 Particle motion of a propagating Rayleigh surface wave: (a) displacement in propagation direction; (b) out-of-plane displacement and (c) resulting elliptical particle motion . . . 10

2.3 Generation of higher harmonic waves due to material nonlinearity . . 11

2.4 Fit of the final FE-data to the analytical solution for nonlinear Rayleigh wave beams (a) and resulting wave beams for fundamental and second harmonic components (b) . . . 15

2.5 Conversion of Rayleigh waves to plane angled pressure waves at a solid-air interface . . . 16

2.6 Acoustic sound pressure distribution of fundamental (f_1 = 2.1 MHz) (a) and second harmonic (f_2 = 4.2 MHz) (b) components along the active surface of the air-coupled receiver . . . 19

3.1 Experimental setup for nonlinear ultrasonic measurements . . . 21

3.2 X-Ray of an Ultran NCG50-D25-P76 non-contact receiver [7] . . . 23

3.3 Investigated specimen with different widths and other dimensions of the experimental setup . . . 24

4.1 Overview of the FE-model generation . . . 27

4.2 Geometry of the wedge and the specimen . . . 29

4.3 Element selection for different parts of the model . . . 31

4.4 Properties of the prescribed displacement applied at the sloped surface of the wedge . . . 33

4.5 Boundary conditions in the FE-model . . . 34

4.6 Analytical excitation of Rayleigh waves in the FE-model . . . 36

4.7 Steps performed to graphically present FE-model output data . . . 41

4.8 Optimization process of the material model and the excitation source properties . . . 43

5.1 Simulation of an air column to determine attenuation effects . . . 45

5.2 Attenuation of acoustic pressure for fundamental (a) and second (b) harmonic components . . . 46

5.3 Arriving pressure amplitudes at the receiver surface for the fundamental (a) and second (b) harmonic component 48

5.4 Experimental wave beams of fundamental (a) and second harmonic (b) components for specimen with different widths, normalized to the corresponding $A_1(x = 25$ mm) 50

5.5 Resulting profile of the ratio A_2/A_1^2 of the experimental wave beams . 52

5.6 Resulting profile of the ratio A_2/A_1^2 after alignment of the propagation directions of the experimental wave beams (a) and analytical solution (b) 53

5.7 Diffraction of the experimental wave beams 55

5.8 Influence of the air-coupled receiver on the measured amplitudes along propagation (a) and width (b) axis 57

5.9 Influence of a point-to-average transformation on the wave beams of fundamental (a) and second harmonic (b) component 59

5.10 Comparison of diffraction of numerical point, averaged numerical and experimental wave beams 61

5.11 Comparison of amplitude profiles (a) and resulting ratio A_2/A_1^2 (b) of numerical point, averaged numerical and experimental values 63

5.12 Amplitude progression of the first (primary y-axis) and second (secondary y-axis) harmonic components along the optical axis for "infinite" and narrow geometry 65

5.13 Amplitude profiles of the first (a) and the second (b) harmonic components and superimposition (c) for "infinite" and narrow geometry . 67

5.14 Relative distance in propagation direction $\Delta\tilde{x}$ of a single Rayleigh wavefront in the "infinite" (a) and the narrow (b) geometry 69

5.15 Evolution of the relative distance in propagation direction $\Delta\tilde{x}$ of a Rayleigh wavefront in the "infinite" (a) and the narrow (b) geometry 71

5.16 Oscillating interaction with the specimen's edges in the case of the narrow width geometry 72

5.17 Oscillating pressure waves leaked into adjacent air in the case of the narrow width geometry 74

B.1 Approximation of source nonlinearity (in percent of the fundamental amplitude) 83

B.2 Influence of source nonlinearity dependent on the initial phase difference of the fundamental and second harmonic component 84

LIST OF SYMBOLS AND ABBREVIATIONS

Symbol	Description
FE	finite element
FEM	finite element method
DFT	discrete Fourier transform
DP	double precision
NDE	nondestructive evaluation
NLU	nonlinear ultrasound
PMMA	Polymethylmethacrylate
P-wave	longitudinal wave
POR	acoustic sound pressure
S-wave	shear wave
SNR	signal-to-noise ratio
TOEC	third order elastic constant
2D	two dimensional
3D	three dimensional
a_n	Gaussian half width
Al	aluminum
A_n	wave amplitude
A_n^{ave}	averaged amplitude
A_n^{el}	detected electrical wave amplitude
A_n^{point}	amplitude of point measurement
$\boldsymbol{A}$	direction of particle movement
A_i, B_i	amplitudes
A, B, C	third-order elastic constants

Symbol	Description
$\boldsymbol{B}$	left Cauchy-Green strain tensor
c	wave velocity
c_P, c_S, c_R	longitudinal, shear, Rayleigh wave velocity
c_{air}	sound speed air
C_{ijkl}	fourth order elastic tensor
C_p	heat capacity
$C_{10}, C_{01}, C_{11}, D_1$	coefficients of hyperelastic material model
$\boldsymbol{E}$	Green strain tensor
E	Young's modulus
f	frequency
f_i	external body force
F	force
$\boldsymbol{F}$	deformation gradient
i	imaginary unit
$\boldsymbol{I}$	identity matrix
I_1, I_2, I_3	invariants of the Green strain tensor
$\bar{I}_1, \bar{I}_2$	isochoric invariants of the left Green-Cauchy strain tensor
J	elastic volume change
k_n	wavenumber
$\boldsymbol{k}$	wavenumber vector
k_P, k_S, k_R	longitudinal, shear, Rayleigh wavenumber
K	bulk modulus
K_0	initial bulk modulus
l_{air}	propagation distance of pressure waves
l_{max}	maximum element edge length

Symbol	Description
l_{min}	minimum element edge length
l_{off}	lift off distance
L_p	sound pressure level
p	pressure
p	acoustic sound pressure
$p_{rec,n}$	sound pressure at the receiver surface
$\tilde{p}_{ref}$	reference value for sound pressure level
$p_{0,n}$	initial sound pressure
P_{ij}	Piola-Kirchhoff stress tensor
R_{stress}	reflection coefficient for stress amplitues
$\hat{\boldsymbol{s}}$	unit propagation vector
t	time
T_{stress}	transmission coefficient for stress amplitudes
T	temperature
u_i	displacement
$\ddot{u}_i$	acceleration
V	volume
v_z	out-of-plane velocity
v_0	peak source amplitude
$v_{0,2}$	peak source amplitude second harmonic
X	Lagrangian coordinates
w_{min}	minimum width
W_s	strain energy density
$x_{0,n}$	Rayleigh distance
x	propagation direction
$\boldsymbol{x}$	position vector

Symbol	Description
y	width direction
z	direction out of finite half space
Z	acoustic impedance
α_n	attenuation coefficient
β	nonlinearity parameter
β'	relative nonlinearity parameter
δ	volumetric drag
ϵ_{ij}	strain tensor
γ	ratio of specific heats
η	shear viscosity
κ	thermal conductivity
θ	angle of leaked pressure waves
θ_i	incident/reflection/transmission angle
θ_D, θ_R	angle of longitudinal, Rayleigh wave
θ_{wedge}	angle of the acrylic wedge
λ, μ	Lamé constants
λ	wavelength
λ_R	Rayleigh wavelength
μ	shear modulus
μ_0	initial modulus
∇	nabla operator
ν	Poisson's ratio
ν	kinematic viscosity
ρ	density
σ_{ij}	Cauchy stress tensor
τ_i, τ_r, τ_t	incident, reflected, transmitted stress

Symbol	Description
Φ	scalar potential
φ_n	phase
Ψ	vector potential
ω	angular frequency

SUMMARY

Non-contact measurements of nonlinear Rayleigh surface waves have shown sensitivity to microstructural changes in a material through the generation of higher harmonic components in an initially monochromatic ultrasonic signal. The objective of this research is to numerically describe the propagation of nonlinear surface wave beams. To ensure accuracy, the model should agree with experimentally observed trends and analytical solutions. The goal is to understand the influence of the inherent physical attributes of the air-coupled receiver on the measured acoustic signal. Finally, a finite element (FE) model is used to determine the causes of previously observed experimental issues with a narrow width specimen.

Experiments are conducted as a starting point for this study. A wedge transducer excites Rayleigh surface waves and an air-coupled receiver detects the fundamental (A_1) and second (A_2) harmonic wave components. Measurements along the propagation and specimen width directions give detailed information about Rayleigh wave amplitude progression and diffraction behavior. These are the critical wave attributes to be matched in the FE-model, optimizing material and source properties. A hyperelastic constitutive law describes material nonlinearity, based on a built-in model of the commercial FE-solver, ABAQUS. The comparison of experimental and numerical results requires the consideration of frequency dependent attenuating pressure waves in air and averaged signal detection by the non-contact, air-coupled receiver. Therefore, a MATLAB code transforms nodal output values into the receiver "perspective" by weighted numerical integration, based on simulated fluid-structure interaction. Subsequently, the validated model is applied to a narrow width specimen (18.5 mm), to investigate the reasons for oscillating behavior in amplitudes previously observed in

experimentally measured signals. Comparison of "infinite" and narrow sample width highlights significant differences. The finite specimen boundaries constrain the expanding wavefronts laterally, which leads to a more significant decrease in amplitudes at the center of the waveguide. Furthermore, interaction of the wavefronts with the specimen edges causes oscillating variations of the Rayleigh wavefronts. When these oscillating signals leak into the adjacent air, height differences of the pressure waves occur, which are detected by the air-coupled receiver.

The results indicate that the inherent response of the non-contact receiver strongly influences the measured characteristic ratio A_2/A_1^2 and its slope. Moreover, the narrow width adversely affects these already sensitive measurements and identifies key issues regarding the consistent measurement of material nonlinearity in certain geometries.

Chapter I

INTRODUCTION

1.1 Motivation and Objective

Nonlinear ultrasonic (NLU) techniques have the potential to detect material damage and microstructural changes, such as low cycle fatigue [11], [48], thermal aging [22] or stress corrosion cracking [50], with very high sensitivity. Changes in the microstructure lead to a nonlinear stress strain relationship and the generation of higher harmonic waves from an initially monochromatic signal. The nonlinearity parameter $\beta \propto A_2/(A_1^2 x)$ relates fundamental (A_1) and second harmonic (A_2) amplitude and has shown to be a reliable measure for material changes and damage.

The use of Rayleigh surface waves offers two advantages. First, acoustic energy is concentrated near the surface, where the material damage is usually initiated. Second, the waves can be excited and detected on the same side of the specimen.

In previous research, Thiele [44] demonstrates that non-contact detection determines the nonlinearity parameter β more consistently when compared to contact methods. However, it is still unclear how the underlying physical attributes of air-coupled non-contact detection affect the nonlinear experimental results. In order to achieve absolute values, critical factors have to be investigated and understood.

While showing higher consistency in the case of a specimen with "infinite" width, things change for narrow samples (18.5 mm width). For these narrow samples, oscillating amplitude progression is observed for both the first and second harmonic frequencies along the propagation distance, causing variability in the measured nonlinearity parameter β [23]. The observation of width influence contradicts findings of Cegla [4] who investigated wavefront-boundary interaction of Lamb wave modes

numerically and experimentally. His results indicate that for frequency-widths products above 15 MHzmm the acoustic energy concentrates at the center of rectangular waveguides, allowing wave propagation undisturbed by the width. This is less than half of the frequency-width product causing problems in nonlinear Rayleigh wave measurements (2.1 MHz $\times$ 18.5 mm = 38.85 MHzmm) as observed by Morlock [23]. The objective of this research is to describe the non-contact, air-coupled measurement technique of nonlinear Rayleigh waves with a 3D numerical finite element (FE) model. The FE-simulation needs to properly match analytical findings, as well as the results of experiments conducted, concerning diffraction and amplitude progression of the first and the second harmonic signal. The goal of this research is to adjust material model and source properties according to experimental data available. This study aims to quantitatively evaluate the influence of the air-coupled receiver on the characteristic ratio A_2/A_1^2 and its resulting slope along the propagation distance. The analysis especially focuses on the frequency dependent attenuation of leaked pressure waves propagating through air, and the resulting signal averaging over the active receiver surface ($\varnothing$12.5 mm). The relevance of the model developed is demonstrated by experimental findings to subsequently investigate the width influence of the narrow wave guide. Finally, the overall objective of this research is to determine the reasons for the oscillating inconsistencies by a comparison of wave propagation behavior in "infinite" and narrow geometry.

1.2 Outline

The structure of this thesis is as follows. Chapter 2 introduces the underlying physics of linear and nonlinear wave propagation, derives the nonlinearity parameter β and considers two dimensional diffraction and attenuation of nonlinear Rayleigh wave

beams. Furthermore the principles of air-coupled, non-contact detection are presented. Chapter 3 focuses on the setup used to conduct experiments, which are necessary to develop and validate the FE-model. Chapter 4 describes model generation, constrained by the geometry of the presented setup and physics of nonlinear Rayleigh wave propagation. Chapter 5 presents and evaluates the results of the present research. Based on insights of fluid-solid interaction, experimental findings can be compared to numerically simulated, nonlinear Rayleigh wave beams. Subsequently, propagation in a narrow wave guide is considered, investigating oscillating inconsistencies observed in experiments. Finally, result interpretation leads to conclusion and possible future work in Chapter 6.

Chapter II

THEORY

This chapter presents some basic theoretical considerations in the field of wave propagation. Special attention is given to Rayleigh waves concerning nonlinear effects and leakage of acoustic energy into the adjacent air.

2.1 Linear Wave Propagation

The detection of propagating waves offers the capability to capture changes in the material micrsotructure and is therefore interesting in the field of nondestructive material evaluation. The following sections briefly derive the governing equations of propagating waves, introduces a special form of surface wave, the Rayleigh wave and concludes in the definition of the nonlinearity parameter β which is an important measure of material nonlinearity and of great importance for this research.

2.1.1 Linear Elastodynamics in an Unbounded Medium

The following section is based on Achenbach [1] and Shearer [31], but only outlines the main points. A more detailed description and the mathematical proof of the solutions presented, can be found in the given references.

The equations describing the motion of a homogeneous, isotropic, linear elastic body are the stress equation of motion:

$$\rho \ddot{u}_i = \delta_j \sigma_{ij} + \rho f_i, \tag{2.1}$$

Hooke's law:

$$\sigma_{ij} = C_{ijkl} \epsilon_{kl}, \tag{2.2}$$

and the strain displacement relations:

$$\epsilon_{ij} = \frac{1}{2}(u_{i,j} + u_{j,i}), \tag{2.3}$$

where σ_{ij} is the symmetric stress tensor at one point, ϵ_{ij} the strain tensor, C_{ijkl} the fourth order stiffness tensor, u_i the displacement vector, f_i an external body force per unit volume and ρ the density. For an isotropic, linear elastic material the stiffness tensor C_{ijkl} reduces to two material constants, e.g. the Lamé constants μ and λ or, more popular the Young's Modulus E and the Poission's ratio ν. Using this simplification and substituting Equations (2.2) and (2.3) into Equation (2.1), leads to the Navier elastodynamic equation, which is given in vector notation (neglecting external body forces) by Equation (2.4):

$$\rho\ddot{\boldsymbol{u}} = (\lambda + 2\mu)\nabla\nabla \cdot \boldsymbol{u} - \mu\nabla^2\boldsymbol{u}, \tag{2.4}$$

where ∇ is the "nabla" operator. If the Helmholtz decomposition of the displacement vector:

$$\boldsymbol{u} = \nabla\Phi + \nabla \times \Psi, \tag{2.5}$$

is substituted into Equation (2.4), applying $\nabla \cdot \nabla\Phi = \nabla^2\Phi$ and $\nabla \cdot \nabla \times \Psi = 0$, two solutions are obtained:

$$\nabla^2\Phi - \frac{1}{c_P^2}\ddot{\Phi} = 0, \tag{2.6}$$

$$\nabla^2\Psi - \frac{1}{c_S^2}\ddot{\Psi} = 0, \tag{2.7}$$

leading to the phase velocities of the compression wave c_P and the shear wave c_S given as:

$$c_P = \sqrt{\frac{\lambda + 2\mu}{\rho}} \tag{2.8}$$

and

$$c_S = \sqrt{\frac{\mu}{\rho}}, \tag{2.9}$$

which only depend on the Lamé constants λ and μ and the density ρ. Thus, $c_P > c_S$ is valid for any material.

2.1.2 Plane Waves

The concept of plane waves describes a solution of the wave equation in which the displacement varies only in the propagation direction. The motion is written as follows:

$$\boldsymbol{u} = \boldsymbol{A} f(ct - \hat{\boldsymbol{s}} \cdot \boldsymbol{x}), \tag{2.10}$$

where $\boldsymbol{x}$ is the position vector at a time t, and the wave propagates in the unit direction $\hat{\boldsymbol{s}}$ with the velocity c. $\boldsymbol{A}$ stands for the direction of the particle movement [31]. Substituting Equation (2.10) into the elastodynamic Navier Equation (2.4) the following expression is obtained:

$$0 = (\lambda + \mu)(\hat{\boldsymbol{s}} \cdot \boldsymbol{A})\hat{\boldsymbol{s}} + (\mu - \rho c^2)\boldsymbol{A}. \tag{2.11}$$

This equation suggests that there are two possible solutions, representing either a longitudinal plane wave ($\boldsymbol{A} = \pm\ \hat{\boldsymbol{s}}$) or a shear wave ($\boldsymbol{A} \cdot \hat{\boldsymbol{s}} = 0$). The plane wave approximation is valid if the wavefronts are flat or locally flat (e.g. in the far field). In this research a special importance is given to plane waves, since the investigated non-contact detection relies on the leaking of plane pressure waves into the adjacent fluid (Section 2.3).

Harmonic Waves Harmonic waves can be termed as monochromatic waves for a constant angular frequency ω and consequently also fulfill Equation (2.10). The expression for a plane harmonic wave is given in Equation (2.12):

$$\boldsymbol{u} = \boldsymbol{A} sin(\boldsymbol{k}\boldsymbol{x} - \omega t), \tag{2.12}$$

where $\boldsymbol{k} = (\omega/c)\hat{\boldsymbol{s}}$ is the wavenumber vector that points in the propagation direction of the wave. The term harmonic wave is especially important in nonlinear wave propagation, which investigates the generation of higher harmonics from a monocromatic signal (see Section 2.2.1).

2.1.3 Reflection and Transmission of Ultrasonic Waves

The equations derived above describe the propagating wave in an unbound infinite medium. However, in the case of ultrasonic waves there is usually an interaction with boundaries or interfaces given. Furthermore the principle of the Rayleigh wave excitation with the wedge technique (see Section 2.1.4) relies on the refraction of waves at a solid-solid interface. Figure 2.1 shows the principle of reflected and transmitted waves at a solid-solid interface for an incident P-wave P_i with an angle θ_{pi}. The wave speeds of solid 2 are higher than those of solid 1, as it is given in the case of the wedge-specimen assembly.

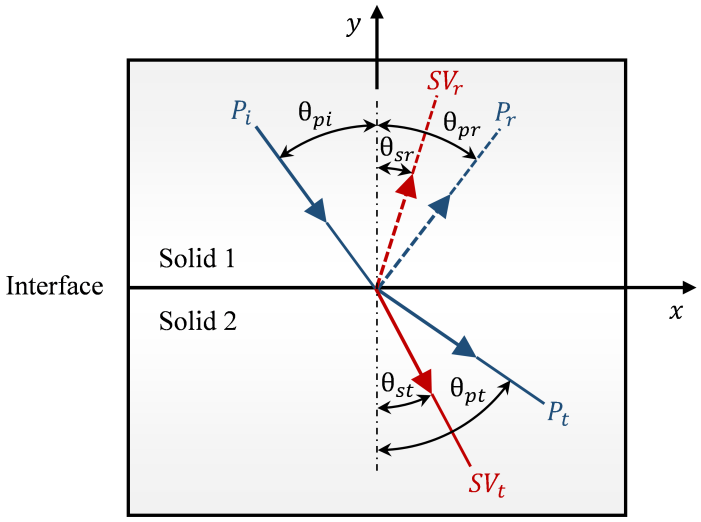

Figure 2.1: Reflection and transmission of waves at a solid-solid interface for an incident P-wave

The angled P-wave incidence results in reflected and transmitted P-waves as well as reflected and transmitted SV-waves. Thereby the depicted angles are dependent on the specific wave velocities in each solid, as defined by Snell's law of refraction:

$$\frac{sin(\theta_{pi})}{c_{P,1}} = \frac{sin(\theta_{pr})}{c_{P,1}} = \frac{sin(\theta_{sr})}{c_{S,1}} = \frac{sin(\theta_{pt})}{c_{P,2}} = \frac{sin(\theta_{st})}{c_{S,2}} \tag{2.13}$$

For the case of the wedge-specimen assembly, which is used to experimentally excite Rayleigh waves, the angle of the sloped wedge surface is calculated using Equation 2.13. A piezoelectric transducer which is fixed on the sloped surface excites an incident P-wave. Thus, the angle of incidence corresponds to the angle of the wedge θ_{wedge}. To excite surface waves the angle of transmission θ_{sw} has to be 90°. The wave speeds of the wedge and the specimen are defined by the material properties (see Table 4.1). Consequently the angle of the wedge θ_{wedge} can be determined as follows:

$$\theta_{wedge} = arcsin\left(\frac{c_{P,wedge}}{c_R}\right), \tag{2.14}$$

where c_R is the speed of the Rayleigh surface wave (see Equation (2.20)).

The non-trivial derivation of the reflection and transmission coefficients which depend on both the angle of incidence and the acoustic impedance ($Z = \rho c_P$) can be found in [1]. In case of a stress free boundary, which is given if solid 2 in Figure 2.1 is replaced by a vacuum, there is no transmission but only reflection of the incident wave. The assumption of the stress free boundary is used to derive the characteristic Rayleigh wave equation (see Section 2.1.4).

For normal incidence, as in case of the pressure waves arriving at the active receiver surface (see Section 2.3), there is no mode conversion and consequently the reflection (Equation (2.15)) and transmission (Equation (2.16)) coefficients for stress or pressure amplitudes R_{Stress} and T_{stress}, only depend on the acoustic impedance.

$$R_{stress} = \frac{\tau_r}{\tau_i} = \frac{\rho_2 c_{P,2} - \rho_1 c_{P,1}}{\rho_2 c_{P,2} + \rho_1 c_{P,1}} \tag{2.15}$$

$$T_{stress} = \frac{\tau_t}{\tau_i} = \frac{2\rho_2 c_{P,2}}{\rho_2 c_{P,2} + \rho_1 c_{P,1}} \tag{2.16}$$

Apparently the reflection coefficient R_{stress} can either be positive, if the impedance of material 2 is larger than the impedance of material 1 (e.g. air-piezo ceramic interface), or negative in the opposite case (e.g. steel-air interface). The negative sign indicates that the reflected wave is shifted by π to the incident wave.

2.1.4 Rayleigh Waves

A detailed description of the Rayleigh wave theory can be found in Victorov [47] or Achenbach [1]. The following remarks are based on these publications and only outline the main characteristics.

Per definition, Rayleigh waves propagate along a stress free surface of an elastic half space. The particle motion contains longitudinal and transversal components which exponentially decay in the depth direction. The derivation of the governing equations starts with the Helmholtz decomposition of the displacement (see Equation (2.5)). The potential functions, which satisfy the Navier elastodynamic Equation (2.4) are derived with the simplification of a plane, harmonic wave propagating in the x-z-plane along the x-direction and are written as follows:

$$\Phi = Ae^{K_p z}e^{i(k_R x-\omega t)} \tag{2.17}$$

$$\Psi = Be^{K_s z}e^{i(k_R x-\omega t)}, \tag{2.18}$$

where $K_p = \sqrt{k_R^2 - k_p^2}$, $K_s = \sqrt{k_R^2 - k_s^2}$ and k_p, k_s and k_R are the wavenumbers of longitudinal, shear and Rayleigh wave with $k_p < k_s < k_R$. If the assumption of a stress free boundary is applied, the characteristic Rayleigh wave equation can be derived as:

$$(K_s^2 + k_R^2)^2 - 4K_s K_p k_R^2 = 0. \tag{2.19}$$

The approximate solution for the Rayleigh wave speed only depends on the Poisson's ratio ν of the material and is given as:

$$c_R = \left(\frac{0.87 + 1.12\nu}{1+\nu}\right)c_S. \tag{2.20}$$

In order to get an expression for the displacements in x- and z- direction the wavenumber of the characteristic equation k_R is taken to simplify the ratio of the potential function amplitudes which can be written as follows:

$$\frac{B}{A} = -i\sqrt{\frac{K_p}{K_s}} \stackrel{def}{=} -i\zeta. \tag{2.21}$$

Using this definition, the normal and tangential displacement components calculate to:

$$u_x = \frac{\partial \Phi}{\partial x} - \frac{\partial \Psi}{\partial z} = iA(k_R e^{K_p z} - \zeta K_s e^{K_s z}) \tag{2.22}$$

$$u_z = \frac{\partial \Phi}{\partial z} + \frac{\partial \Psi}{\partial x} = -A(K_p e^{K_p z} - \zeta k_R e^{K_s z}). \tag{2.23}$$

Both equations express the exponential decay in the negative z-direction (depth-direction). Furthermore a phase shift of π is observable leading to an elliptical particle movement. The FE-plots in Figure 2.2 show the phase shift of u_x (part a)) and u_z (part b)) and the resulting elliptical particle movement in part c).

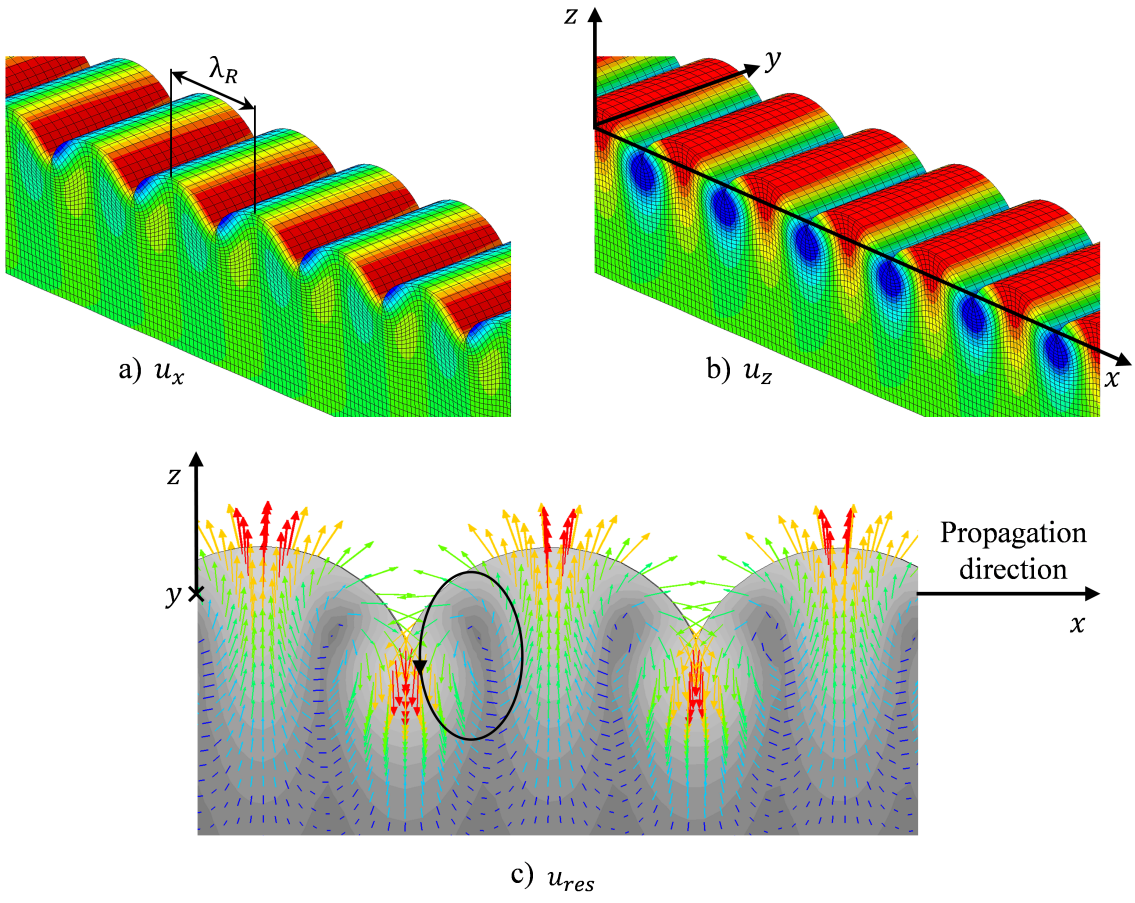

Figure 2.2: Particle motion of a propagating Rayleigh surface wave: (a) displacement in propagation direction; (b) out-of-plane displacement and (c) resulting elliptical particle motion

2.2 Nonlinear Wave Propagation

This research considers the generation of higher harmonics from a monochromatic signal due to material nonlinearities. The principle is shown in Figure 2.3. In a linear elastic material the input frequency equals the output frequency. If the material has a nonlinear stress-strain relationship, higher harmonic wave components of the input signal are generated. In nonlinear measurements a special interest is given to the second harmonic wave component.

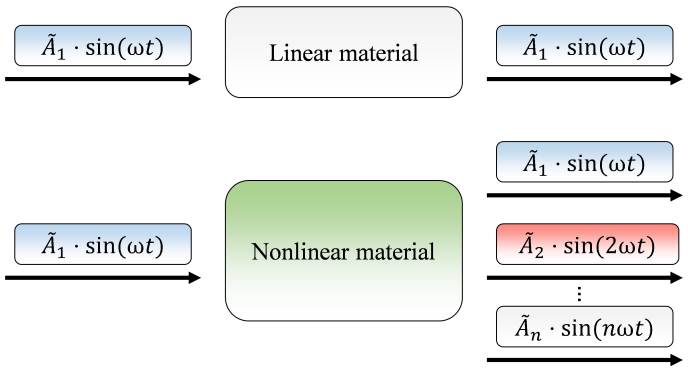

Figure 2.3: Generation of higher harmonic waves due to material nonlinearity

2.2.1 Nonlinear Elastodynamics in an Unbounded Medium

This section briefly presents the concepts of nonlinear wave propagation. A more detailed consideration is given by Hamilton and Blackstock [10].

Nonlinear elasticity in solids is usually formulated in terms of Lagrangian coordinates (material reference system X) instead of Eularian (spatial reference system x) coordinates, since it is reasonable to assume that the material nonlinearity depends on local stretching and volume change. The correlation of coordinate systems is given by the deformation gradient tensor $\boldsymbol{F}$:

$$\mathbf{F} = \frac{\partial x}{\partial X}. \tag{2.24}$$

Equation (2.1) can be written in Lagrangian coordinates as:

$$\rho_0 \ddot{u}_i = \partial_j P_{ij}, \tag{2.25}$$

where ρ_0 denotes the initial density and P_{ij} is one entry of the first Piola-Kirchhoff stress tensor $\boldsymbol{P}$ defined as:

$$\mathbf{P} = \rho_0 \boldsymbol{F} \cdot \frac{\partial W_s}{\partial \boldsymbol{E}}. \tag{2.26}$$

Here $\boldsymbol{E}$ denotes the Green strain tensor written as follows:

$$\mathbf{E} = \frac{1}{2}(\boldsymbol{F}^T \cdot \boldsymbol{F} - \boldsymbol{I}), \tag{2.27}$$

and W_s the strain energy density. The parameter W_s is expressed in terms of the three invariants $I_1 = tr(\boldsymbol{E}),\ I_2 = tr(\boldsymbol{E^2}),\ I_3 = tr(\boldsymbol{E^3})$ of the Green strain tensor, the Lamé constants λ and μ and, in this notation, the third-order elastic constants (TOEC) $A,\ B,\ C$ used by Landau and Lifshitz [21]:

$$W_s = \frac{1}{2}\lambda I_1^2 + \mu I_2 + \frac{1}{3} C I_1^3 + B I_1 I_2 + \frac{1}{3} A I_3 + O(E_{ij}^4), \tag{2.28}$$

where the last expression stands for terms higher than cubic order which are typically very small and can be neglected. If the Equations (2.25) to (2.28) are assembled a complex expression for the nonlinear wave equations results for the three dimensional case which can be found in [15]. For the simplified case of a longitudinal plane wave propagating in the x-direction Equation (2.29) results:

$$(\lambda + 2\mu)\frac{\partial^2 u_x}{\partial^2 x} - \rho \frac{\partial u_x^2}{\partial t^2} - (3(\lambda + 2\mu) + 2A + 6B + 2C)\frac{\partial u_x}{\partial x}\frac{\partial^2 u_x}{\partial x^2} = 0, \tag{2.29}$$

where we now introduce the acoustic nonlinearity parameter β:

$$\beta \stackrel{def}{=} -\left(\frac{3}{2} + \frac{A + 3B + C}{(\lambda + 2\mu)}\right) \tag{2.30}$$

and further simplify Equation (2.29) written as follows:

$$\frac{\partial u_x^2}{\partial t^2} = c_P^2 \left[1 - \beta\left(\frac{\partial u_x}{\partial x}\right)\right] \frac{\partial^2 u_x}{\partial x^2}. \tag{2.31}$$

2.2.1.1 *Practical Application in Nonlinear Rayleigh Wave Measurements*

Nonlinear ultrasonic measurements usually quantify the amplitudes of the fundamental (A_1) and created second harmonic (A_2) component. For the case of a harmonic P-wave excitation with amplitude A_1 and angular frequency ω the perturbation approach [27] leads to the solution:

$$u_x = A_1 sin(\omega t - kx) - \underbrace{\frac{1}{8}\beta k^2 A_1^2 x}_{A_2} sin(2\omega t - kx) \tag{2.32}$$

and finally to an expression that can be determined experimentally along the propagation distance x:

$$\beta = \frac{8A_2}{k^2 A_1^2 x}. \tag{2.33}$$

This expression of the nonlinearity parameter β is only valid for longitudinal waves. It has been shown that β vanishes for transverse waves associated with a plane of material symmetry [26]. In Section 2.1.4 it is discussed, that Rayleigh surface waves are a superposition of longitudinal and transversal waves, whereby only the out of plane displacement at the surface is detected in experimental measurements. Herrmann et al. prove [11] that the nonlinearity parameter of Rayleigh waves for that particular case can be written as:

$$\beta = \frac{8i\hat{u}_z(2\omega)|_{z=0}}{xk_l^2\hat{u}_z^2(\omega)|_{z=0}} \frac{K_p}{k_R}\left(1 - \frac{2k_R^2}{k_R^2 + K_s^2}\right), \tag{2.34}$$

which also shows $\beta \propto A_{2,z}/(A_{1,z}^2 x)$ as similarly expressed by Equation (2.33).

2.2.2 Nonlinear Rayleigh Wave Beams

Shull et al. [32] present an analytical description of nonlinear Rayleigh wave beams considering attenuation and diffraction effects. For a Gaussian source of half width a_0 and peak amplitude v_0, Equation (2.35) describes the first and Equation (2.36) the second harmonic component. Equation (2.35) expresses the diffraction by a parabolic approximation and the attenuation by an exponential decay with the attenuation

coefficient α_1. In both equations, x stands for the propagation distance and x_0 for the Rayleigh distance $x_0 = k_0 a_0^2/2$ which is dependent on the initial wave number k_0.

$$v_1(x,y) = \frac{v_0 e^{-\alpha_1 x}}{\sqrt{(1+\frac{ix}{x_0})}} \times exp\left(\frac{(y/a_0)^2}{1+\frac{ix}{x_0}}\right) \times exp\left[i(k_1 x - \omega_1 t + \varphi_0)\right] \tag{2.35}$$

$$\begin{aligned} v_2(x,y) = & \frac{i\sqrt{\pi}\beta v_0^2 k_0^2 a_0^2}{4c_R\sqrt{i(\alpha_2 - 2\alpha_1)(x_0+ix)}} \\ & \times exp\left(-\alpha_2 + \frac{2(y/a)^2}{1+\frac{i\times x}{x_0}} + i(\alpha_2 - 2\alpha_1)x_0\right) \\ & \times erf(\sqrt{i(\alpha_2 - 2\alpha_1)(x_0+ix)}) \\ & - erf(\sqrt{i(\alpha_2 - 2\alpha 1)x_0}) \times exp\left[i(k_2 x - \omega_2 t + \varphi_{0,2}^M)\right] \end{aligned} \tag{2.36}$$

where c_R is the Rayleigh wave speed and α_2 the attenuation coefficient of the second harmonic. The second is generated by the first harmonic component due to nonlinearities in the material. Material nonlinearity is expressed by the nonlinearity parameter β dependent on the Landau and Lifshitz constants [32], [49].

In addition to Equation (2.35) and (2.36), Thiele [44] proposes a modification of the second harmonic component which takes the nonlinearity of the source (electrical system nonlinearity, transducer nonlinearity, contact nonlinearity and material nonlinearity under the wedge) into account. The formula is written as follows:

$$v_{2,S}(x,y) = \frac{v_{0,2}\cdot e^{-\alpha_2 \cdot x}}{\sqrt{(1+\frac{i\cdot x}{x_{0,2}})}} \times exp\left(\frac{(y/a_{0,2})^2}{1+\frac{i\cdot x}{x_{0,2}}}\right) \times exp\left[i(k_2 x - \omega_2 t + \varphi_{0,2}^T)\right], \tag{2.37}$$

where the difference to Equation (2.35) is given by a Gaussian half width of the source $a_{0,2}$, a Rayleigh distance $x_{0,2} = k_{0,2} a_{0,2}^2/2$ and an exponential decay of the second harmonic peak source amplitude $v_{0,2}$ with the attenuation coefficient α_2. Thiele [44] concludes that the consideration of the source nonlinearity is essential to fit the presented equation with experimental results. Thus, the summarized expression for the second harmonic component is given by:

$$v_{2,Total}(x,y) = v_{2,S}(x,y) + v_2(x,y). \tag{2.38}$$

Figure 2.4 part a) depicts the one dimensional fit of the derived equations above (absolute values of the real part) to the final solution of the FE-model, where all amplitudes are normalized to the peak source amplitude v_0 of the fundamental component. The resulting parameters a_0, $a_{0,2}$, α_1, α_2 and β are subsequently used to plot the two dimensional wave beams in part b) of the figure. The fundamental amplitude decreases along the propagation distance whereby the second harmonic amplitude increases until a maximum value is reached. This behavior is also observed in experiments and considered more closely in Section 5.2.

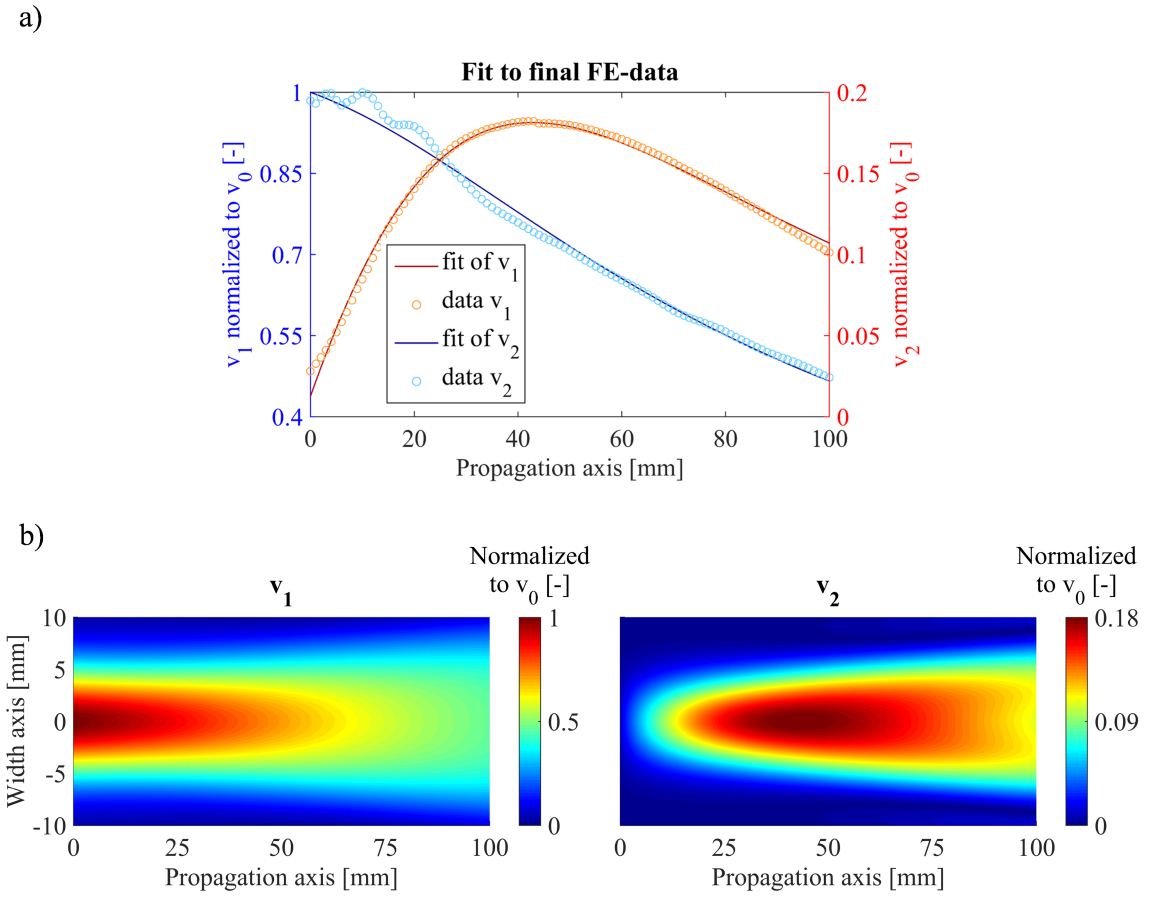

Figure 2.4: Fit of the final FE-data to the analytical solution for nonlinear Rayleigh wave beams (a) and resulting wave beams for fundamental and second harmonic components (b)

2.3 Leaky Rayleigh Waves

This section introduces the fundamentals of non-contact detection by an air-coupled receiver. It outlines the physical attributes and is of essential importance for the further understanding of this thesis.

2.3.1 Formation of Plane Angled Pressure Waves

In non-contact measurements, longitudinal pressure waves in air are detected by an air-coupled receiver [45]. Those pressure waves are excited by the leaking of the Rayleigh surface waves into air. Figure 2.5 shows the principle of pressure wave formation and propagation. The propagating surface wave sets local disturbances, which spread out with the sound speed of air, forming a circular wavefront [6]. Those wavelets combine to a plane wavefront propagating with an angle θ as indicated in the figure. Thus, the surface wave is leaked as angled pressure wave into the adjacent fluid.

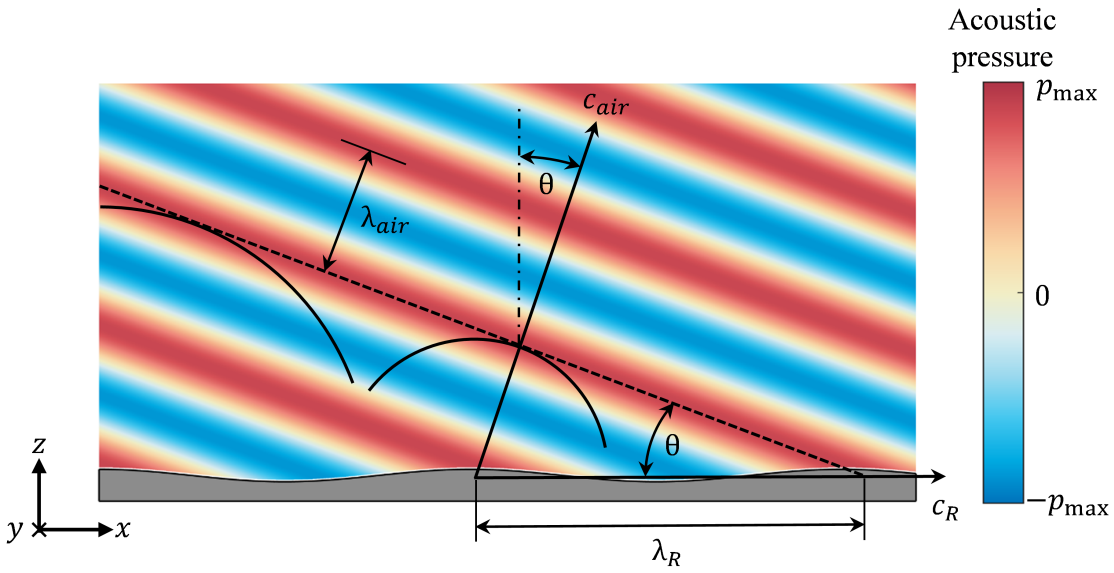

Figure 2.5: Conversion of Rayleigh waves to plane angled pressure waves at a solid-air interface

This angle of inclination θ is calculated as follows:

$$\theta = arcsin\left(\frac{\lambda_{air}}{\lambda_R}\right) = arcsin\left(\frac{c_{air}}{c_R}\right), \tag{2.39}$$

and shows to only depend on the material properties of solid and fluid. For the combination of stainless steel (Rayleigh wave speed $c_R \approx 2870$ m/s) and air (sound speed $c \approx 344$ m/s) a resulting angle $\theta \approx 6.88°$ can be calculated. The propagation of plane pressure waves in the time domain is expressed by Equation (2.40) [13] where ρ is the density of air and $k_z = \sqrt{k_{air}^2 - k_R^2}$ the wavenumber in the vertical z-direction. The amplitude relates to the out-of-plane velocity of the Rayleigh wave $v_{z,R}$ which is therefore taken as nodal output value in the modeling part (see Section 5.3).

$$p(x,z) = \frac{v_{z,R}\rho c_{air}k}{k_z} \times exp[i(\omega t - k_x x - k_z z)]. \tag{2.40}$$

Since the velocity of the pressure waves in air is considerably slower than the Rayleigh wave speed in steel (344.5 m/s to 2870 m/s), the wavelength of the pressure waves is much smaller than that of the Rayleigh waves. This is of big importance concerning the required mesh density (see Section 4.3.1).

The leakage of ultrasonic waves into air can lead to sound pressure levels far above 100 dB [7]. In the present research acoustic pressures of over $p = 8$ Pa are obtained for the given model configuration (compare Section 5.1). The equivalent sound pressure level L_p,

$$L_p = 20 \cdot log_{10} \cdot \frac{p}{\tilde{p}_{ref}}, \tag{2.41}$$

calculates to ≈ 112 dB, where $\tilde{p}_{ref} = 20$ μPa is the reference pressure [28].

2.3.2 Attenuation of Pressure Waves in Air

The equations described above do not consider the attenuation of the pressure waves. In the "classical" description the acoustic, or kinetic energy of the molecules is transformed into heat energy, dependent on the properties of the fluid, expressed by [2]:

$$\alpha_{classical} = \frac{\omega^2}{2\rho_0 c^3}\left[\frac{4}{3}\eta + \left(\gamma - 1\right)\frac{\kappa}{C_p}\right], \tag{2.42}$$

where ω is the angular frequency, η is the shear viscosity, ρ_0 the density, γ the ratio of the specific heats, C_p the heat capacity, c the wave speed and κ the thermal conductivity. The attenuation coefficient is proportional to ω^2 which leads to a four times higher value for the second harmonic component. For the given frequencies ($f_1 = 2.1$ MHz and $f_2 = 4.2$ MHz) and the standard values for air (see Table 4.2), attenuation coefficients of α_1= 61.61 Np/m and α_2 = 246.47 Np/m are calculated. However, Bond et al. [2] state that for high frequencies above 1 MHz, attenuation effects due to the rotational relaxation loss α_{rot} cannot be neglected anymore. Based on experimental data, Equation (2.43) is proposed:

$$\alpha_{high-frequency} = 1.83 \times 10^{-11}(T/T_0)^{1/2} f^2/(p/p_0), \tag{2.43}$$

where the measured temperature T and the measured pressure p is referenced to T_0 and p_0 respectively. This equation results in attenuation coefficients which are higher than those obtained above $\alpha_1 = 80.70$ Np/m and $\alpha_2 = 322.81$ Np/m).

The receiver is adjusted according to angle of inclination $\theta \approx 6.88°$ of the pressure waves. Therefore, the waves travel different distances until they arrive at the active receiver surface. Since attenuation strongly depends on propagation distance, the arriving amplitudes differ along the active receiver surface as sketched in Figure 2.6. Note, that for this plot the coefficients of high-frequency attenuation are used and that the fundamental acoustic sound pressure is named p_1 and the second harmonic acoustic sound pressure is named p_2.

Both parts of the figure are normalized to the initial sound pressure $p_{0,n}$, directly above the surface of the solid. The higher attenuation coefficient of the second harmonic component (p_2) leads to a considerably lower signal arriving at the receiver surface than for the fundamental component (p_1). On the highest point of the active receiver surface, 72 % of the initial sound pressure $p_{0,1}$ arrive in the case of p_1 and only around 30 % of $p_{0,2}$ in the case of p_2. At the lower point 82 % are received for the first and 48 % for the second harmonic component. Since nonlinear measurements relate the generated second harmonic to the fundamental component (see Section 3.2.2), the different attenuation behavior clearly affects experimental results, which is considered in Section 5.3.

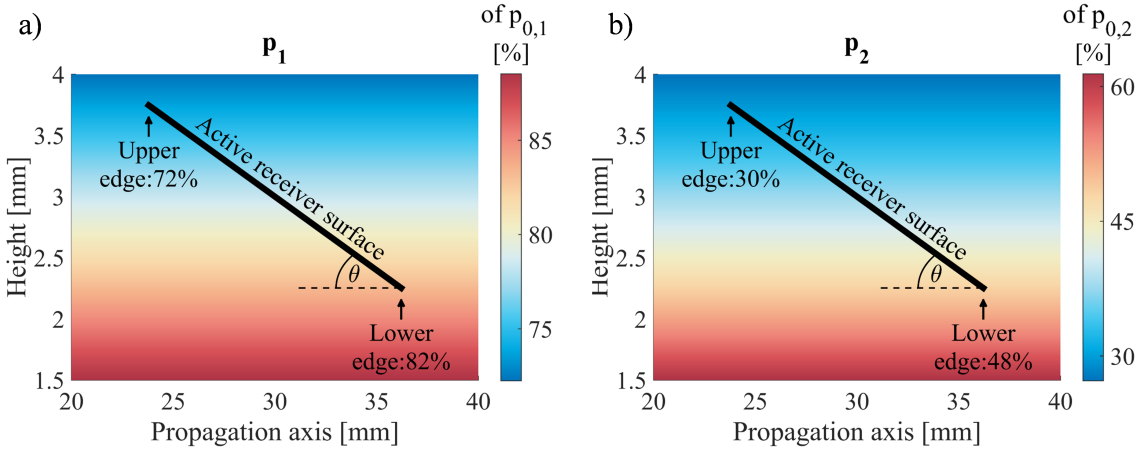

Figure 2.6: Acoustic sound pressure distribution of fundamental ($f_1 = 2.1$ MHz) (a) and second harmonic ($f_2 = 4.2$ MHz) (b) components along the active surface of the air-coupled receiver

Chapter III

NONLINEAR AIR-COUPLED RAYLEIGH WAVE MEASUREMENTS

3.1 Experimental Setup

Figure 3.1 shows a sketch of the experimental setup (top) used to perform the measurements as well as picture of the components finally considered in the model (bottom).

A function generator produces a signal with the specified properties. Subsequently the signal is amplified by a high power amplifier. The high-voltage signal is transferred to a narrowband piezoelectric transducer that excites longitudinal waves at the inclined surface of an acrylic wedge. Based on Snell's law of refraction, the longitudinal waves are transformed into Rayleigh surface waves at the wedge-specimen interface. Both the transducer-wedge interface, and the wedge-specimen interface are connected by applying a clamping force and using an oil couplant. The Rayleigh waves excited, propagate along the specimen surface leaking angled longitudinal pressure waves into the air which are detected by an air coupled receiver. The receiver is adjusted according to the angle θ of the pressure waves in air. To improve the signal to noise ratio the output signal is post amplified and then recorded and averaged by an oscilloscope [24], [44] and [22].

3.1.1 Components

The following sections briefly describe the single components depicted in the figure above. A more detailed description can be found in [44] or [24].

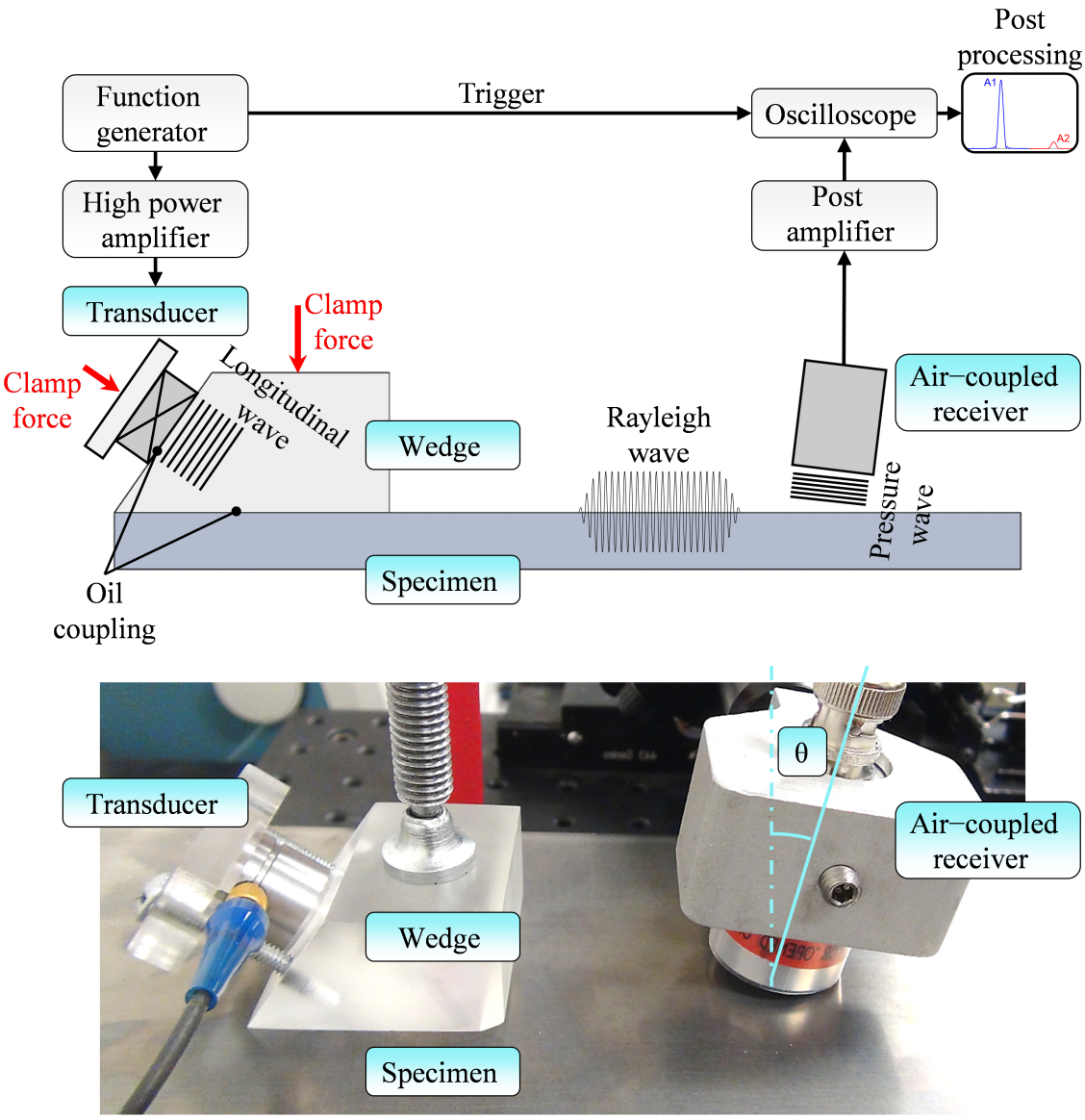

Figure 3.1: Experimental setup for nonlinear ultrasonic measurements

3.1.1.1 Function Generator

A 80 MHz 33250A function generator from Agilent generates the signal which is finally transferred to the transducer. A peak-to-peak voltage of 800 mV is adjusted and a sinusoidal tone burst of 2.1 MHz frequency is chosen. The signal length of 20 cycles ensures a sufficient steady state portion for the subsequent post processing. The internal trigger synchronizes the source with the amplifier and the oscilloscope.

3.1.1.2 High Power Amplifier

A RITEC GA-2500A gated amplifier is used to generate a high voltage signal essentially important for nonlinear ultrasonic measurements. The high acoustic energy is necessary to separate the generated second harmonic component from the signal noise. In order to ensure stable output values the amplifier has to be turned on 30 min before use [44].

3.1.1.3 Transducer and Wedge

A Panametrics X-type (custom narrow-band) contact transducer with center frequency 2.25 MHz and an active diameter of ∅12.7 mm is clamped to an acrylic wedge which itself is clamped to the surface of the specimen being measured. To ensure good coupling, the interfaces are covered with a light oil film. The exciting transducer transforms the amplified signal into longitudinal waves at the inclined wedge surface. The angle of the wedge is determined according to Snell's law as discussed in Section 2.1.3 and amounts to $\approx 55.1°$. This angle guarantees the transmission of Rayleigh surface waves at the wedge-specimen interface.

3.1.1.4 Air-coupled Receiver

A piezo electric circular Ultran NCT4-D13 air-coupled receiver with a center frequency of 4 MHz detects the angled pressure waves leaked by the Rayleigh surface waves. To ensure an accurate detection of the second harmonic component ($f_2 = 4.2$ MHz) the center frequency has to be in a comparable range. The active area of the non-contact receiver is ∅12.5 mm according to the manufacturer's specifications [43].

The central issue in ultrasonic measurements is the impedance difference of the piezo ceramic and air (Z_{PZT} = 30-32 MRayl to Z_{air} = 0.0004 MRayl [7]; compare to Equation (2.16)). In order to still get a good signal quality the impedance of the piezo material is lowered using so-called piezo composites. Those metamaterials consist of an active phase, defined by thin rods of piezo material and a passive phase given by

a soft and light matrix (e.g. epoxy resin or silicon). Thereby an acoustic impedance of $Z < 10$ MRayl can be achieved. Furthermore an inserted "anti reflex layer" of thickness $\lambda/4$ significantly improves the coupling of piezo material and surrounding air. The manufacturer Ultran speaks of "multi layered patented Z matching" [43]. Figure 3.2 shows a X-ray of an Ultran NCG50-D25-P76 air-coupled receiver. The housing, the connections and the piezo ceramic elements (rods) are observable.

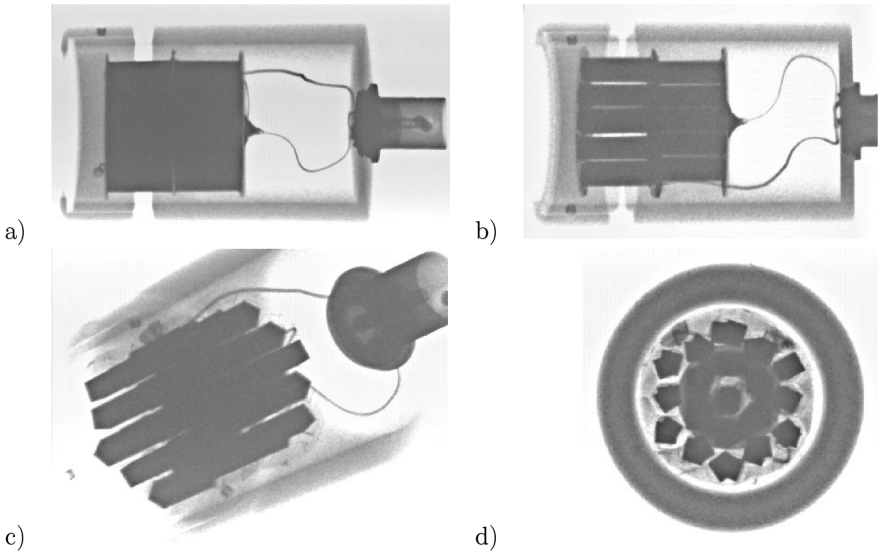

Figure 3.2: X-Ray of an Ultran NCG50-D25-P76 non-contact receiver [7]

3.1.1.5 Specimen

To evaluate boundary influence, three specimens of different width are considered experimentally. Thereby the materials investigated are assumed to be homogeneous, isotropic and sufficiently elastic. A large stainless steel plate (25 mm × 300 mm × 300 mm) defines the reference geometry, regarded as a quasi "infinite" without boundary influence. An intermediate stage of 25 mm width is investigated additionally. Since there is no stainless steel specimen available for the geometry described, an aluminum sample is used instead.

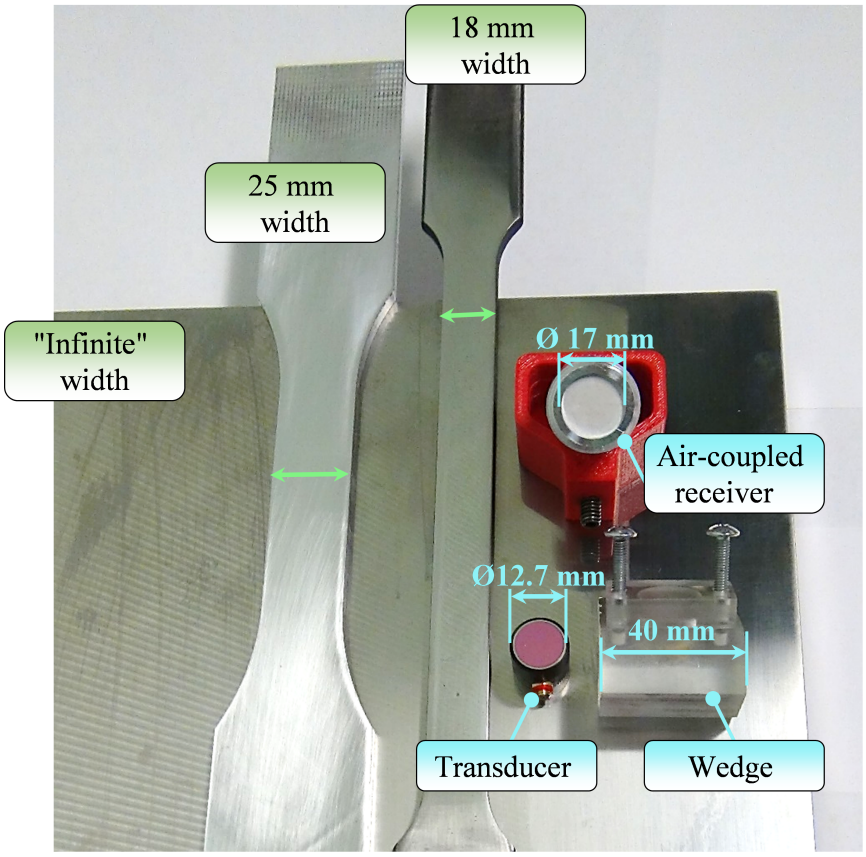

Figure 3.3: Investigated specimen with different widths and other dimensions of the experimental setup

The Rayleigh wave speed of aluminum ($c_{R,Al} \approx 2909.7$ m/s) and stainless steel ($c_{R,steel} \approx 2872.7$ m/s) are in the same range, why geometrically induced effects are assumed to be comparable. The problem causing stainless steel sample of 18.5 mm width defines the smallest geometry. Figure 3.3 shows the specimens described and the components used to perform experimental measurements. By comparison, the indicated dimensions of transducer and receiver diameter are in the range of the narrow sample with 18.5 mm width. The wedge exceeds the specimen's width by far. Note, that the "apparent opening" of the non-contact receiver (⌀17 mm) is not the active receiver surface. However, it is assumed that the receiver is sensitive to various effects over the whole narrow specimen's width, due to the "apparent opening's" dimension [16].

3.1.1.6 Post Amplifier

The Panametrics 5072PR post amplifier increases the signal-to-noise-ratio (SNR) of the detected signal. Although the air-coupled receiver is optimized to achieve a high transmission of the arriving pressure waves, the output signal without post amplification is around 1-2 mV but reaches values of 100-200 mV after an enhancement of 40 dB by the amplifier [22].

3.1.1.7 Oscilloscope

A TDS5034B Digital Phosphor oscilloscope of Tektronix records the amplified signal. A sampling rate of 250 MS/s is chosen, whereby the final output represents the average of 256 recorded sequences. The averaged signals decrease the noise level of the output, which is subsequently post processed in MATLAB.

3.2 Generation of Experimental Results

This section describes the determination of the relative nonlinearity parameter β' from the output signal. The parameter β' is used in experiments to evaluate material nonlinearity.

3.2.1 Calibration

Before the actual measurements are conducted, the experimental setup needs to be calibrated precisely. Thereby two parameters are adjusted ensuring consistent measurement quality. First the angle θ between the air-coupled receiver and specimen surface is to determined to get maximum signal strength. Although calculable analytically (see Section 2.3), it is approved in practice to change the angle θ in small increments finding a optimal output signal for the specific configuration of the present study. Second, it is observed that the wedge transducer assembly does not excite the Rayleigh wave beam perpendicularly and straight in the middle but with an angle and an offset, respectively. Thus, it is necessary to find the propagation path of the

waves, measuring the maximum signal parallel to the wedge tip for minimum (x_{min}) and maximum (x_{max}) propagation distance. A line connecting these two maximums defines the axis where the measurements will be made. It is shown by Thiele [44] that a misalignment adversely affects the quality of the results.

3.2.2 Relative Nonlinearity Parameter β'

After the calibration, the receiver is moved along this predefined line in increments of 1 - 2 mm. For each of the positions, an output signal is saved and processed afterwards, mapping the time-domain to the frequency-domain with a discrete Fourier transform (DFT) (see Section 4.5). The frequency domain allows the extraction of the electric output amplitudes for first (A_1^{el}) and second (A_2^{el}) harmonic frequency. The ratio:

$$\beta' \stackrel{def}{=} \frac{A_2^{el}}{(A_1^{el})^2 x} \tag{3.1}$$

is defined as the relative nonlinearity parameter β' and approximated by the slope of $A_2^{el}/(A_1^{el})^2$ along the propagation distance x in experiments.

Chapter IV

MODELING

4.1 Overview

Figure 4.1 shows an outline of the modeling process and the software used. The geometry is built in SolidWorks (a computer-aided design software) and subsequently imported into HyperMesh v13.0, a preprocessing software which generates high-quality meshes and conveniently exports *.inp files usable with ABAQUS v6.14. ABAQUS/Explicit solves the *.inp files and generates an output database (.*odb file). The final post-processing is performed in ABAQUS/Viewer to extract the desired data processed with MATLAB afterwards. This research prefers ABAQUS/Explicit as the commercial FE-solver because of its high efficiency. Morlock [24] uses COMSOL for nonlinear, two dimensional Rayleigh wave simulations and describes a computation time of 10-40 hours. This computation time corresponds to the computation time for a three dimensional model in ABAQUS/Explicit (see Section 4.4.3) when using comparable hardware.

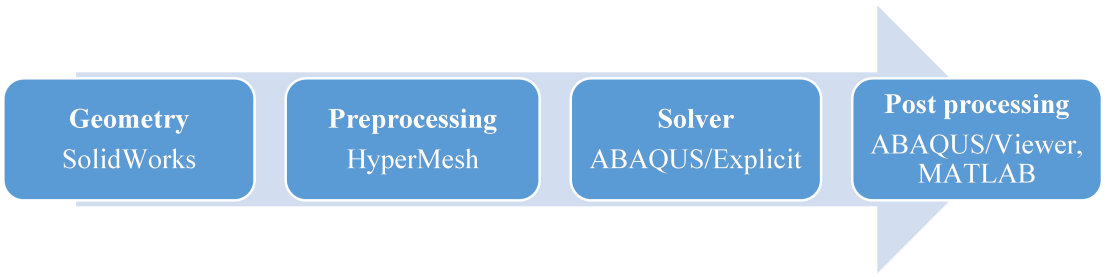

Figure 4.1: Overview of the FE-model generation

4.2 Geometry

The experimental setup (see Section 3.1.1) defines the geometry. In terms of modeling, this setup consists of two or three separate parts, and note that the clamps are not included. The resulting, relatively straightforward, geometry shown in Figure 4.2 consists of a wedge, a specimen, and a finite air volume (only if fluid-structure interaction is investigated).

4.2.1 Wedge Geometry

The most critical portion of the wedge is the angle between the transducer face and specimen surface which is determined by Snell's law (see Section 2.1.3). In this research a constant angle $\theta_{wedge} \approx 55.1\ ^\circ$ is calculated based on the material properties in Table 4.1. Due to simplifications discussed in the following Section 4.3.2, there is no space for fixations or boreholes (compare Figure 3.1) necessary. Thus the modeled volume only needs to be large enough to ensure an unaffected propagation of longitudinal waves in the wedge. The lateral dimension was halved from 40 mm (experimental size of the wedge) to 20 mm (10 mm if symmetry is applied), and the height slightly exceeds the upper edge of the projected transducer face. The vertical position of the transducer itself corresponds to the same position used in the experimental part of this research. The optimal excitation according to Victorov[47] defines the horizontal dimension, where the projection of the wedge tip onto the sloped wedge surface coincides with the upper edge of the transducer.

4.2.2 Specimen Geometry

A simple cuboid approximates the specimen as the second component in the model. Since the Rayleigh wave displacement nearly vanishes at a depth of $2\lambda \approx 2.8$ mm, this value is regarded to be sufficiently large for the specimen's thickness. In order to prevent unwanted reflections from the specimen's bottom, a layer of infinite elements

(see A.1) is included in all simulations. The modeled length is defined by the propagation distance, the length of the wedge (24.3 mm), and a run-off area (≈ 18 mm), which is necessary to prevent interference with reflected waves from the back face (despite infinite elements). Since the influence of the width is investigated within this research, two specimen geometry widths are modeled. One width is an "infinte" width (sufficiently large lateral extension), and the other width is for the narrow geometry which is 18.5 mm. Finally the definition of a surface grid ensures equal extraction points in every simulation.

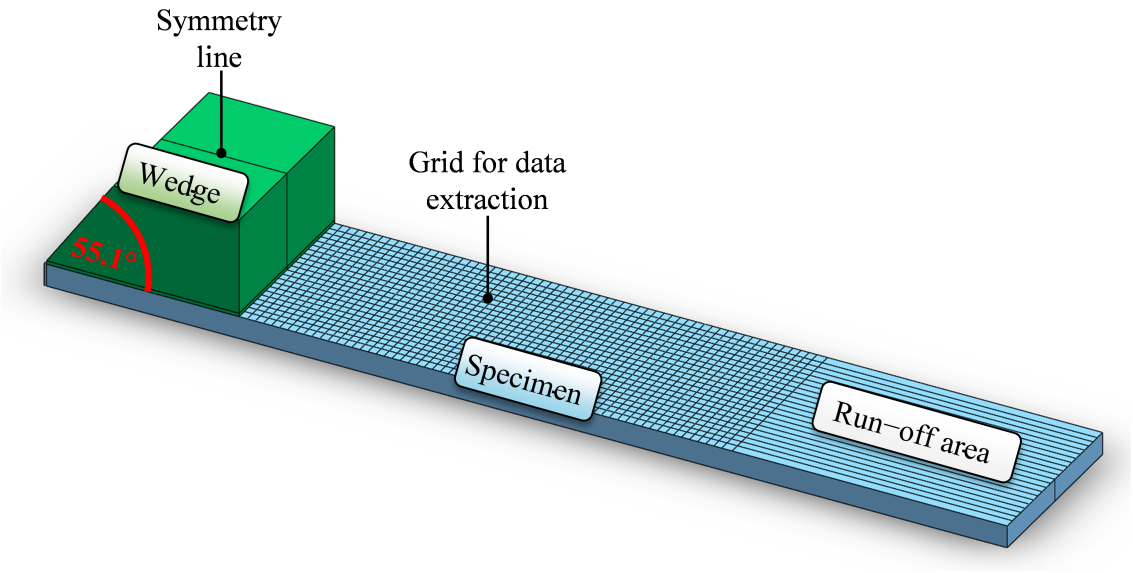

Figure 4.2: Geometry of the wedge and the specimen

4.2.3 Fluid Volume Geometry

For the coupled structural acoustic analysis, a fluid volume has to be included. The plane wave characteristic of the pressure waves allows a model of the fluid volume using rectangular edges, facilitating the subsequent meshing considerably. It is of high importance to consider the angle of inclination of the waves, adjusting the angle of the volume sides and thus, preventing reflections (compare Figure 5.1). If the fluid volume covers the edge of the narrow specimen, the "element-offset" feature of

HyperMesh proves to be useful in order to maintain a high quality mesh. An example of such a mesh can be seen in Figure 4.3.

4.3 Preprocessing

The following sections describe element selection and meshing steps performed to suitably resolve the geometry. Thereby, the performance of two analysis types allows to investigate the experimental setup numerically:

1. Coupled structural acoustic analysis
2. Transient dynamic analysis.

The first type refers to fluid-structure interaction and the leaking of the Rayleigh wave, whereby the second type considers the wave propagation itself in the given wave guides. To approximate experimental values, results of both parts have to be merged.

4.3.1 Element Selection and Meshing

The aspect ratio and Jacobian for model elements are considered as an important quality criterion during the mesh generation. Thereby only linear hexaedral elements with reduced integration are used.

4.3.1.1 Mesh Density

The application of a mesh to the model geometry has to ensure, that the waveform propagating through the model is captured accurately while maintaining reasonable run times. The size of a finite element is typically determined according to the smallest wavelength occurring during the analysis. Datta and Kishore suggest eight nodes per wavelength [5] which is taken as a value by Nucera [27]. Morlock [24] and Romer [29] use 10 nodes, and Moser et al. recommend even more nodes at twenty nodes per wavelength [25]. A convergence analysis on a 2D model, similar to the present 3D geometry, shows that 10 nodes per wavelength lead to results with

sufficient quality [20]. For the second harmonic component ($f_{A_2} = 4.2$ MHz) and the given Rayleigh wave speed of $c_R = 2872.7$ m/s (see Table 4.1), the maximum element edge length is $l_{max,steel} = c_R/(10 f_{A_2}) \approx 6.84{\times}10^{-5}$ m $= 68.4$ μm. However, since the sound speed in air (344 m/s) is is eight times smaller than the Rayleigh wave speed c_R in the specimen, the required element edge length $l_{max,air}$ reduces by the same factor leading to a value of 8.19 μm. Consequently, a very high mesh density is required anywhere the stress travels. This restricts the effect of element minimization techniques based on variable element sizes. However, the propagation direction of waves is known to a large extent. Along this direction a small mesh size is required but may be more coarse parallel to the wavefront. Thus, the adjustment of aspect ratios considerably reduces the number of elements, e.g an aspect ratio of 2 leads to a reduction in the number of elements of a factor 4 (2×2).

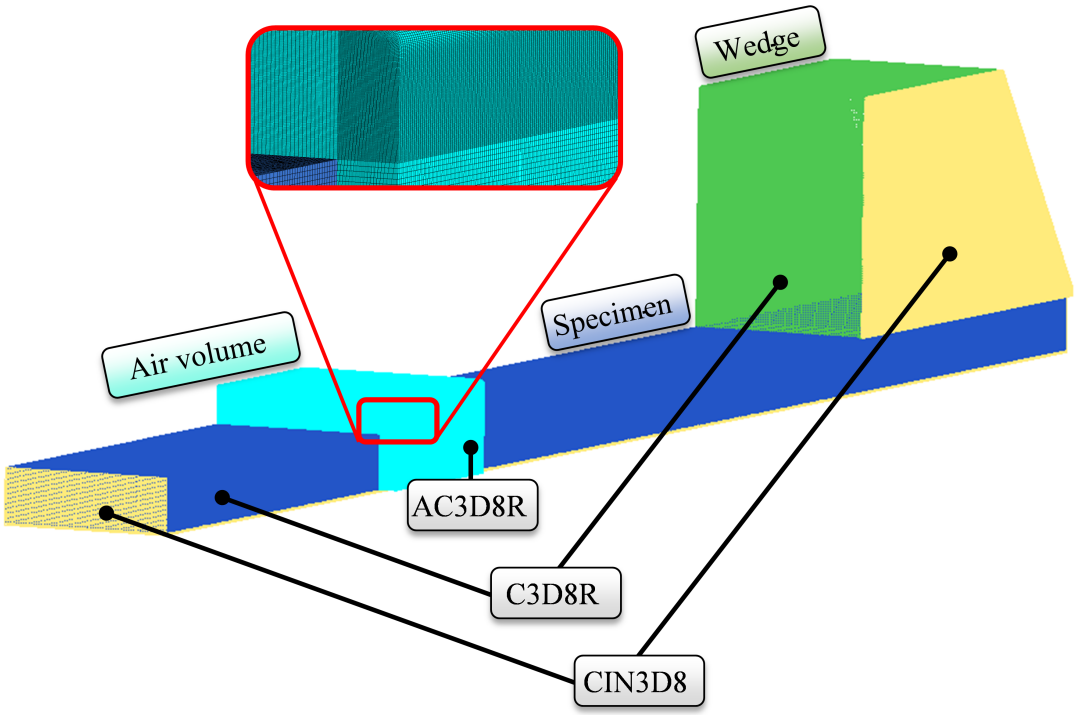

Figure 4.3: Element selection for different parts of the model

Element Types Figure 4.3 lists the different element-types (bottom labels) and the related model components (top labels). Note, that the symmetry plane is defined by the backside in this figure. The final mesh consists of the following element types:

• C3D8R (**C**ontinuum Element, **3D**, **8** Nodes, **R**educed Integration) is used to mesh the wedge and the steel specimen.

• AC3D8R (**A**coustic **C**ontinuum Element, **3D**, **8** Nodes, **R**educed Integration) is used to mesh the air-volume.

• CIN3D8 (**C**ontinuum one-way **In**finite Element, **3D**, **8** Nodes) is used to reduce the model size, generating "quiet" boundaries.

The elements presented are succefully used or investigated for similar applications. Nucera [27] models nonlinear wave propagation in railways with C3D8R elements. Hubenthal [12] investigates the accuracy of AC3D8R. Thereby he outlines, that AC3D8R is a suitable element for acoustic wave propagation in ABAQUS/Explicit and modeling of fluid-structure interaction. A detailed description of the element types and definition of the term "reduced integration" are given in A.1.

Node Sets After the mesh is generated it is necessary to define specific node sets for the subsequent steps. Those sets are required in order to apply loads and boundary conditions and to extract nodal output values for the post processing (see Section 4.5).

4.3.2 Loading and Boundary Conditions

The application of suitable boundary conditions reduces the complexity of the FE-model. Using a zero displacement boundary condition replaces fixations. Furthermore the assumption of a perfectly bonded wedge-specimen interface prevents the implementation of computationally expensive contact conditions. Additionally, the exciting transducer is simplified to a prescribed, transient displacement on an area representing the transducer-wedge interface (circle of ∅12.7 mm).

4.3.2.1 Prescribed Displacement

According to Morlock [24] and Romer [29] an oscillating displacement with amplitude of ± 1.5 nm is appropriate to represent the piezoelectric transducer. Instead of a uniform displacement distribution (perfect piston), the bending stiffness of the transducer contact surface is taken into account [18] (modeled by a Gaussian bell as shown in Figure 4.4 a). The shape of the bell is subject to an optimization as described in Section 4.5.2. The volume under the bell equals the volume of a piston with peak amplitude of 1.5 nm to implement the same "transducer power". In order to prevent transient effects caused by abrupt displacement changes, a ramp function is used to modify a pure sinusoidal signal (see Figure 4.4 b). The frequency of the input signal amounts to 2.1 MHz corresponding to the experimental investigations.

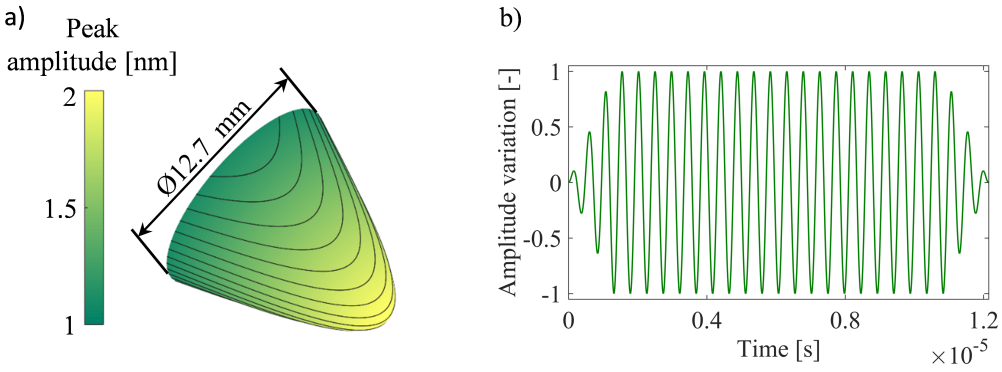

Figure 4.4: Properties of the prescribed displacement applied at the sloped surface of the wedge

Symmetry A mid-plane symmetry condition reduces the model size by 50 %. This is possible because all of the models meet the following criteria:

- Symmetric geometry.
- Isotropic material properties.
- Symmetric load and boundary conditions.

Figure 4.5 displays the boundary conditions and the symmetry plane. "Axial symmetry" indicates that nodal displacement in y-direction and nodal rotation around x- and z- axis are set to zero ($u_y = u_{Rx} = u_{Rz} = 0$), "fixed" signifies all displacements and rotations are 0, and "prescribed displacement" represents the excitation of the longitudinal waves at the sloped wedge surface.

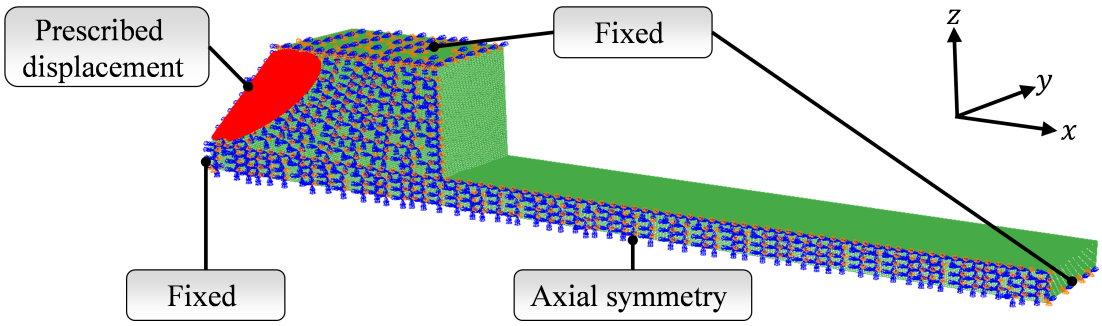

Figure 4.5: Boundary conditions in the FE-model

4.3.2.2 Fluid-Structure Interaction

In order to transform the out-of-plane displacement of the specimen surface into longitudinal pressure waves in the adjacent air-volume, the structural and acoustic meshes have to be coupled. In ABAQUS/Explicit the only available method to enforce coupling is a surface based tie constraint [42]. This requires the meshes to have separate nodes. Element based contact surfaces are defined for both the specimen and the air. In the contact pair, the solid is the "master" and the air element the "slave" surface, constraining the displacements of acoustic to structural nodes. To ensure accurate results, the meshes of the two surfaces are congruent, refining the solid mesh if contact to air is simulated. In order to avoid unwanted reflections at air volume faces, a non-reflecting impedance boundary condition (type: "improved" planar) [42] is applied on the outer skin of the finite volume. However, similar to

infinite elements at the specimen's faces, the boundary condition does not absorb the entire acoustic energy. Therefore, sufficient distance to the air volume "walls" is provided to prevent interference with reflected pressure waves.

4.3.2.3 Analytical Excitation of Rayleigh Waves

If suitable, the simulated Rayleigh waves are excited with prescribed, analytical displacement fields instead of the wedge technique. Especially the simulations of fluid-structure interaction are modeled with this approach because the fluid volume requires a high number of elements already (compare Section 4.3.1). The implemented fields are based on both numerical results and theoretical considerations. Figure 4.6 depicts extracted values (symbols) of the FE-wedge-specimen-model and corresponding analytical fields in part a) and part b). The coordinate system refers to the convention in this research. In the negative out-of-plane direction ($\widehat{=}$ depth-direction) the typical Rayleigh wave displacement is used for u_x and u_z as derived in Equations (2.22) and (2.23) (part a)) in the figure). The amplitude in the width direction has a maximum at the center of the waveguide and approaches zero further outside. The extracted profile is close to a Gauss curve (part b)). The curvature of a wavefront is considered geometrically. In the far field the center of a wavefront is typically slightly ahead of the outer parts. The shape of the wavefront corresponds to extracted model data (compare Section 5.4.2.2) which is approximated by a polynomial and implemented as an equation driven line in SolidWorks. With the first derivative of the polynomial and the application of trigonometric functions, it is possible to excite the waves perpendicular to the curved profile as the physics require [17]. The finally implemented displacements for all axis directions result from the superimposition of the single wave fields. Part c) shows the displacement in x-direction as an example.

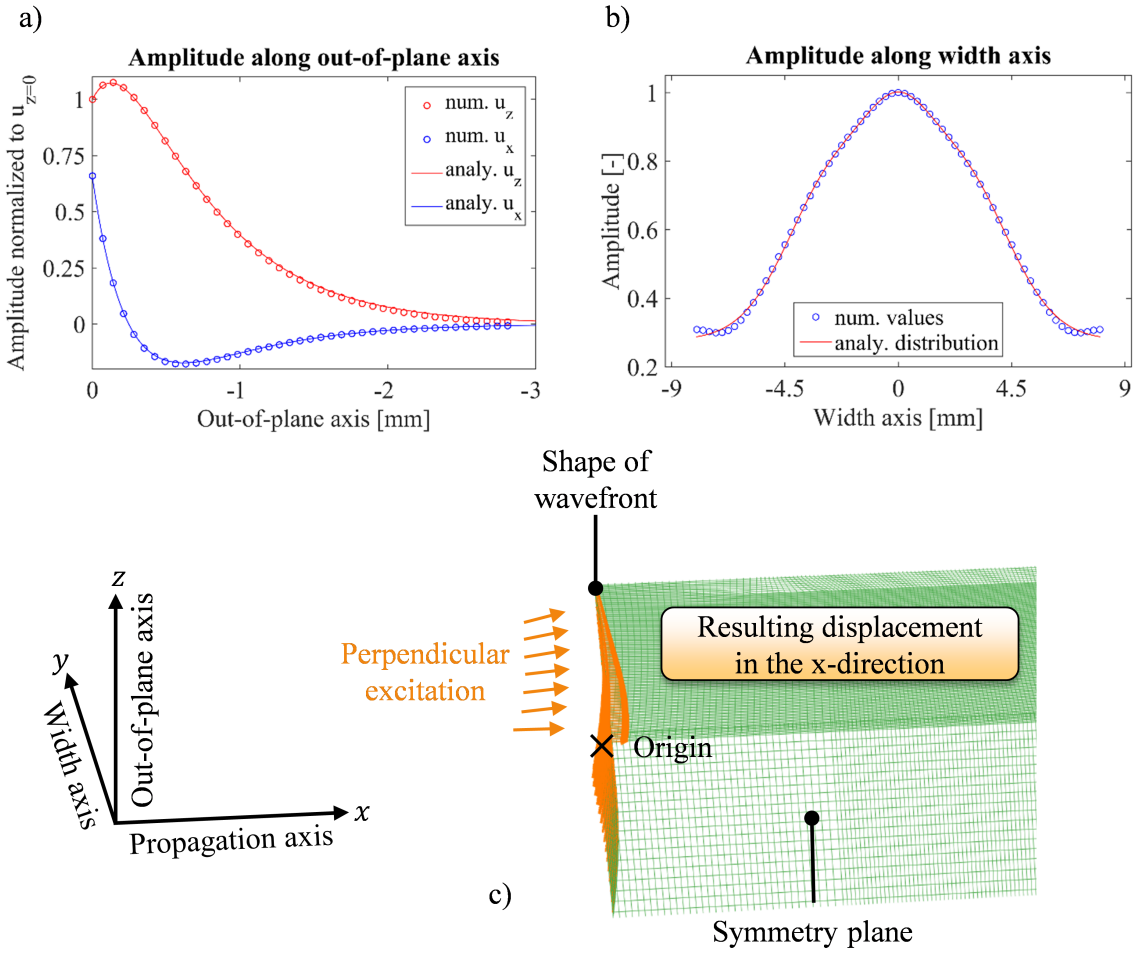

Figure 4.6: Analytical excitation of Rayleigh waves in the FE-model

4.3.3 Material Properties

As the geometry, material parameters refer to the given experimental setup. Thus, the wedge consists of Polymethylmethacrylat (PMMA), the specimen of 304 stainless steel, and typical values for air under standard conditions are implemented. Table 4.1 shows the assumed linear elastic material properties for the solids and Table 4.2 the properties of air. The experimentally measured P-wave speed of the wedge amounts to $c_{P,w}$ =2356 m/s [30], which is matched through the modification of the Young's modulus according to Equation (2.8). The linear elastic material properties of steel are the basis for the developed nonlinear material model presented in Section 4.3.3.1.

Table 4.1: Linear elastic material properties of solid components

Material	Density ρ [kg/m^3]	Young's Modulus E [MPa]	Poisson Ratio ν [-]	P-wave speed c_P [m/s]	S-wave speed c_S [m/s]	Rayleigh wave speed c_R [m/s]
Steel	8000.0	200,000.0	0.305	5842.9	3094.9	2872.7
PMMA	1190.0	4115.7	0.350	2356.0	1131.8	-

Table 4.2: Material properties of air

Material	Density ρ [kg/m^3]	Bulk Modulus K [MPa]	Sound speed c_{air} [m/s]	kinematic viscosity ν [Pas]	shear viscosity μ [Pas]
Air	1.2	0.142	344	110e-7	184.6e-7

Introducing the volumetric drag coefficient δ into the description of the acoustic medium, air, leads to attenuation of pressure waves along the propagation distance. The coefficient is calculated based on Equation (4.1) and expresses the loss of acoustic energy into heat energy:

$$\delta(\omega) = \frac{\omega^2}{c^2}\left(\nu + \frac{4}{3}\eta\right), \tag{4.1}$$

whereby ν stands for the kinematic viscosity and μ for the shear viscosity. As in Equations (2.42) and (2.43), the second harmonic attenuates with a coefficient that is four times larger than the fundamental component, which is due to squared frequency dependence of δ. For the values in Table 4.2 and the frequencies of $\omega_{A1} = 2\pi \times 2.1$ MHz and $\omega_{A2} = 2\pi \times 4.2$ MHz, a volumetric drag of $\delta(\omega_{A1}) = 53.06$ kNs/m^4 and $\delta(\omega_{A2}) = 221.24$ kNs/m^4 is calculated. However, the special characteristics of high-frequency wave attenuation as described in Section 2.3 are not considered in Equation (4.1).

4.3.3.1 Nonlinear Material

A nonlinear stress strain relationship allows the simulation of higher harmonic generation. In this research, a hyperelastic constitutive law models the nonlinearity of stainless steel.

The ABAQUS material library does not include the Landau-Lifshitz formulation (see

Section 2.2.1). Therefore, an adjustment of the parameters for a built-in material model is necessary, which leads to a comparable description of material nonlinearity. The isochoric invariants $\bar{I}_1, \bar{I}_2$ of the isochoric left Cauchy-Green strain tensor $\bar{\boldsymbol{B}}$ and the elastic volume change $J = det(\boldsymbol{F})$ are used to formulate an expression for the strain energy density W_s (further information are given in A.2). The formulation for the strain energy density W_s, implemented in this research, is a second order polynomial of the form [36]:

$$W_s(\bar{I}_1, \bar{I}_2, J) = C_{10}(\bar{I}_1 - 3) + C_{01}(\bar{I}_2 - 3) + C_{11}(\bar{I}_1 - 3)(\bar{I}_1 - 3) + \frac{1}{D_1}(J-1)^2, \quad (4.2)$$

where C_{10}, C_{01}, C_{11} and D_1 are the adjustable parameters of the constitutive law. Regardless of the polynomial order, the coefficients C_{10}, C_{01} and D_1 relate to the initial shear modulus μ_0 and the initial bulk modulus K_0 as shown in Equation (4.3) and (4.4):

$$\mu_0 = 2(C_{10} + C_{01}) \quad (4.3)$$

$$K_0 = \frac{2}{D_1}, \quad (4.4)$$

and thus can be calculated based on the material properties in Table 4.1. In order to approximate the Landau-Lifshitz material model, the polynomial expression of the strain energy (Equation (4.2)) is fitted to artificial test data generated in COMSOL, whose material library offers the typical description of acoustoelasticity. For the fit an uniaxial tension test, a plane strain test and a biaxial tension test are simulated according to [14]. The values of the strain energy density W_s, the isochoric invariants of the Cauchy Green strain tensor $\bar{I}_1$, $\bar{I}_2$, and the elastic volume ratio J are extracted from the results of the simulations. This data serves as the input for a multiple regression performed in MATLAB. The resulting coefficients define the basis for the material model optimization (see Section 4.5.2). The finally implemented parameters are given as: $C_{10} \approx 24.5$ GPa, $C_{01} \approx 13.8$ GPa, $C_{11} \approx$ -2.7$\times 10^7$ GPa and $D_1 \approx 1.17 \times 10^{-2}$ 1/GPa.

4.4 Solving

The simulation of high speed dynamics and structural-acoustics requires small times steps. Therefore, an explicit solver is the clear method of choice [33].

4.4.1 Time Increments

In explicit numerical simulations, the right choice of time step is critical to ensure numerical stability and properly resolve the dynamic event evolution. The step needs to be small enough to calculate the dynamic equilibrium. Thus, the stress wave should not propagate more than the minimum element length l_{min} within one time increment ($\triangle t < l_{min}/c_P$). Furthermore, Moser et al. [25] recommend a minimum of 20 points per cycle at the highest frequency for an appropriate temporal resolution. Additionally a sampling frequency, which is at least twice the highest frequency excited, fulfills Shannons principle and avoids aliasing in the subsequent DFT [27]. With a maximum frequency of $f_{max} = 4.2$ MHz for the second harmonic component, the time step has to meet the following criteria:

$$\triangle t_{min} \leq \begin{cases} \frac{l_{min}}{cP_{max}} \approx 8.7 \times 10^{-8} \text{ s} \\ \frac{1}{20 f_{max}} \approx 1.1 \times 10^{-8} \text{ s} \\ \frac{1}{2 f_{max}} \approx 1.2 \times 10^{-7} \text{ s}. \end{cases} \tag{4.5}$$

The time step finally chosen in the models is far below the values above and amounts between $4{\times}10^{-9}$ s to $2{\times}10^{-9}$ s in order to ensure accurate results.

4.4.2 Explicit Procedure

The explicit solver performs the analysis using a large number of inexpensive, small, time steps. This matches with the high temporal resolution required. Thereby, the calculation advances the kinematic state from the previous time increment. A state of the dynamic equilibrium is solved, using a lumped mass matrix to efficiently determine the nodal accelerations at a given time t. The nodal velocities and displacements

are updated using explicit dynamic integration (also known as the forward Euler or central difference algorithm), instead of iterating until convergence is achieved (implicit solver) [33].

4.4.3 Hardware and Computation

The tremendous requirements concerning spatial and temporal resolution lead to the need for large computational resources. On top of that the calculations are to run in double precision (DP) in order to prevent the accumulation of numerical errors. DP is required if the nodal displacements are less than 1×10^{-6} of the corresponding coordinates or if a hyperelastic material is included [41], and both are found in the present research. The use of DP leads to a 30 % higher CPU requirement compared to single precision.

All simulations are run on an Intel Core TM i7-4770 CPU @ 3.40 GHz, 8 core processor with 16 GB RAM. Shared memory parallelization is used to run the models on all available cores. The average computation time of the 3D models with up to 3×10^{7} degrees of freedom amounts between 12 and 40 hours.

4.5 Post Processing

This section considers the data processing of the FE-model output values. The first part describes the generation of two dimensional surface plots, based on nodal output data. The second part explains the approach in the development of the final model configuration.

4.5.1 Graphical Presentation of Output Data

Figure 4.7 shows the steps performed to graphically present the FE-model output. These considerations refer to the transient dynamic analysis.

4.5.1.1 Data Extraction

In the first step, nodal output values of predefined node sets are extracted from the generated ABAQUS output database (*.odb file). Thereby, the keyword *HISTORY OUTPUT tells ABAQUS to store the requested output values over simulation time. The upper part of Figure 4.7 highlights the nodes used and their distribution over the surface considered. Those nodes define a grid with a distance of 1 mm between the nodes in both the x-and the y-direction.

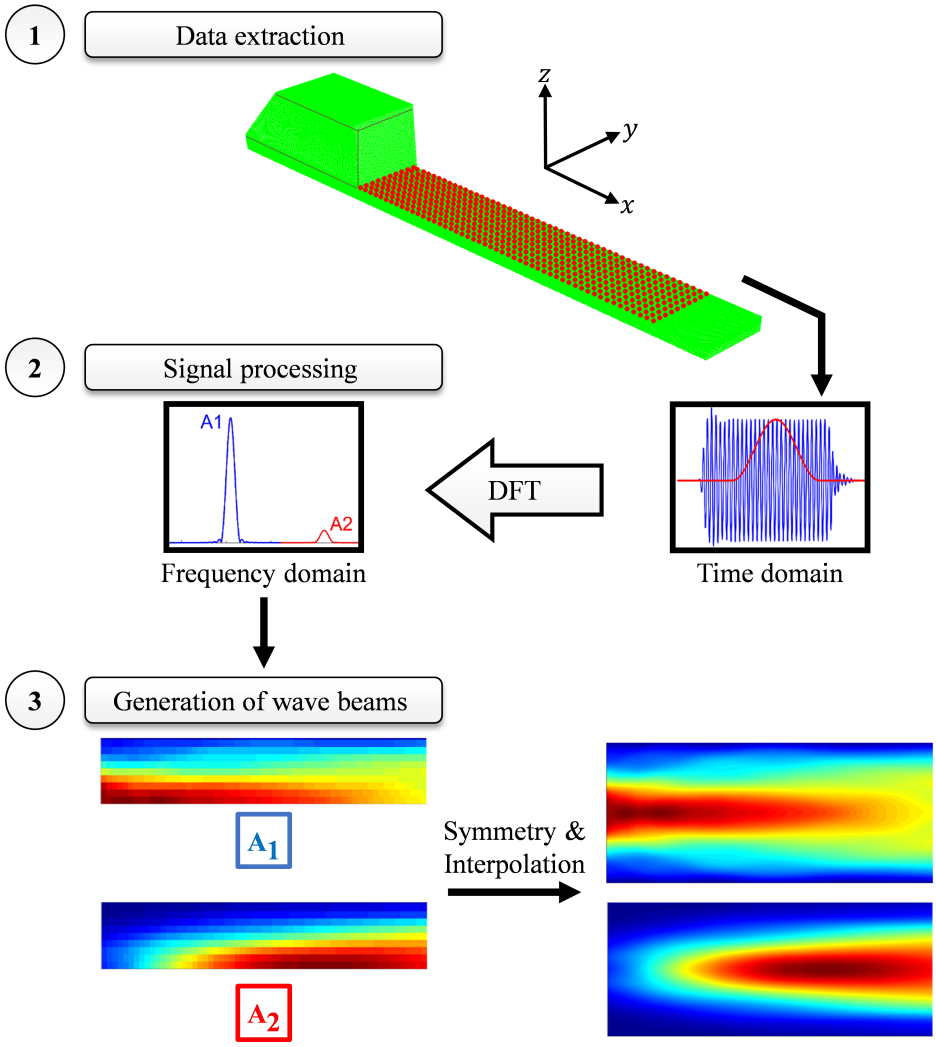

Figure 4.7: Steps performed to graphically present FE-model output data

4.5.1.2 Signal Processing

The amplitudes of the fundamental (A_1) and second harmonic (A_2) components are obtained by processing the time domain signal. The application of a Hanning window (red line in the right part of step 2) determines a steady state portion, which is mapped into the frequency domain by a DFT (left part of step 2). The maximums referring to the first (2.1 MHz) and second (4.2 MHz) harmonic frequency are extracted and related to the time domain amplitudes using Equation (4.6), as is done by Romer [29] and Morlock [24]:

$$\text{time domain amplitude} = \frac{4 \times \text{frequency domain amplitude}}{\text{number of data points used for Hanning window}}. \quad (4.6)$$

This procedure leads to a value for A_1 and A_2 at every node in the predefined grid.

4.5.1.3 Generation of Wave Beams

The figures in step 3 merge the information about amplitude and corresponding grid position of each node into single plot. The coarse resolution leads to a blurred image, which does not allow a satisfactory result interpretation. In order to draw a clearer picture, the output values are mirrored at the symmetry axis and interpolated on a finer grid using the MATLAB built-in "interp2()" function. Thus an informative picture is obtained to be used in further investigations.

4.5.2 Material Model and Excitation Source Optimization

The optimization of model parameters is an essential part of this research to approximate experimental observations (see Section 5.2). Figure 4.8 shows the flow chart of the proceedings. The starting point for the material model is the generation of auxiliary data with COMSOL, which are fit to a built-in material model of ABAQUS using MATLAB. After a simulation has completed, the results are evaluated against the experimental findings and modified accordingly. Thereby, it turns out that the implemented material parameter strongly influences the progression of fundamental

and second harmonic amplitudes. Furthermore, the diffraction of the components mainly relies on the properties of the source, more specifically the peak amplitude distribution as described in Section 4.3.2. This can be explained by different near field characteristics, because waves excited by a piston transducer need longer to reach the typical Gaussian profile (see Section 2.2.2) than waves already excited by a Gaussian source.

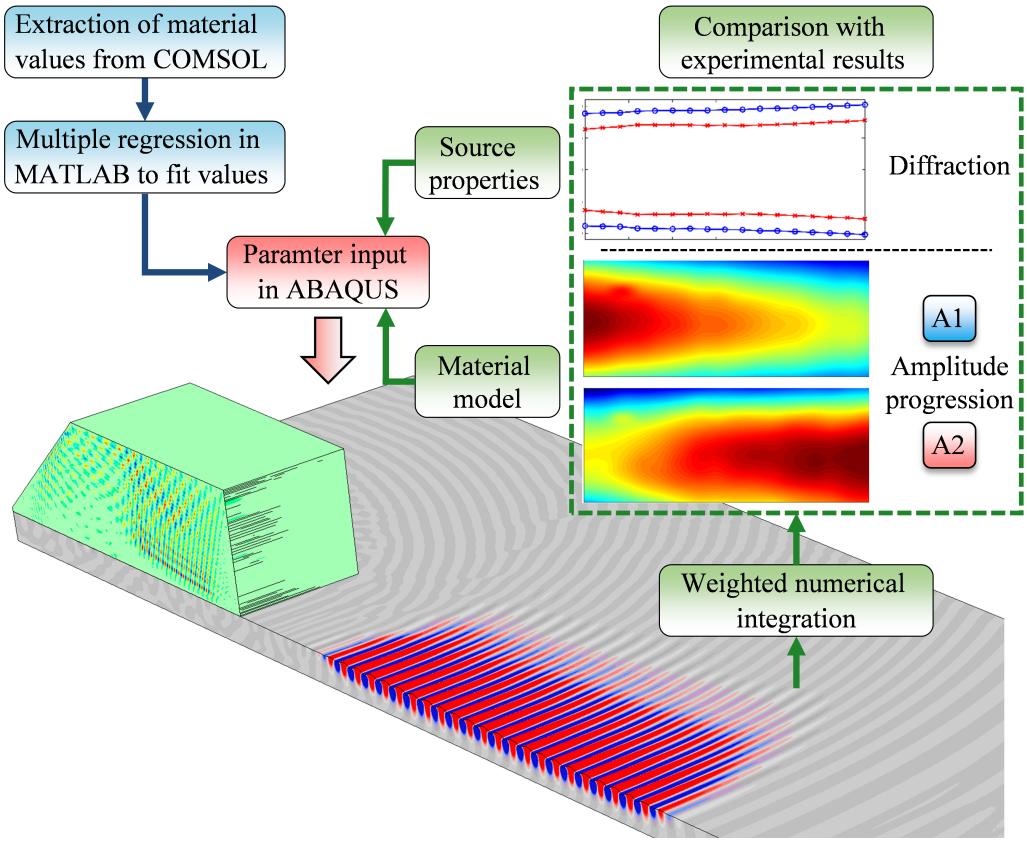

Figure 4.8: Optimization process of the material model and the excitation source properties

Chapter V

RESULTS AND DISCUSSION

This chapter presents the numerical results which are validated by experimental measurements. Subsequently, the FE-model generated is applied to a narrow geometry (18.5 mm) which causes inconsistencies in the experiments. Differences between "infinite" and narrow geometry are compared, and used to reach conclusions about the influence of a restricting boundary.

5.1 Numerical Description of Fluid-Structure Interaction

This section considers the propagation of the pressure waves and evaluates attenuation along the propagation distance from the specimen's surface to the air-coupled receiver's active surface. This leads to the derivation of component specific weight functions, implemented in a code transforming the numerical point-measurements into the receiver-"prespective".

5.1.1 Simulation of an Air-Column

Due to the very high mesh density required to resolve the pressure waves spatially, the Rayleigh waves are excited by an analytical displacement field (see Section 4.3.2.3). Thereby, a huge number of elements can be saved ($\approx$ 3,000,000) making it possible to investigate the entire propagation distance of the pressure waves until the arrival at the imaginary active receiver surface. Such an "air-column" model is shown in Figure 5.1. The Rayleigh waves propagate from left to right leaking angled pressure waves in the adjacent fluid volume. In this contour plot, the attenuation of the pressure waves is observable along the propagation axis as the color intensity decreases with distance to the specimen surface (see color bar of the acoustic pressure on the left).

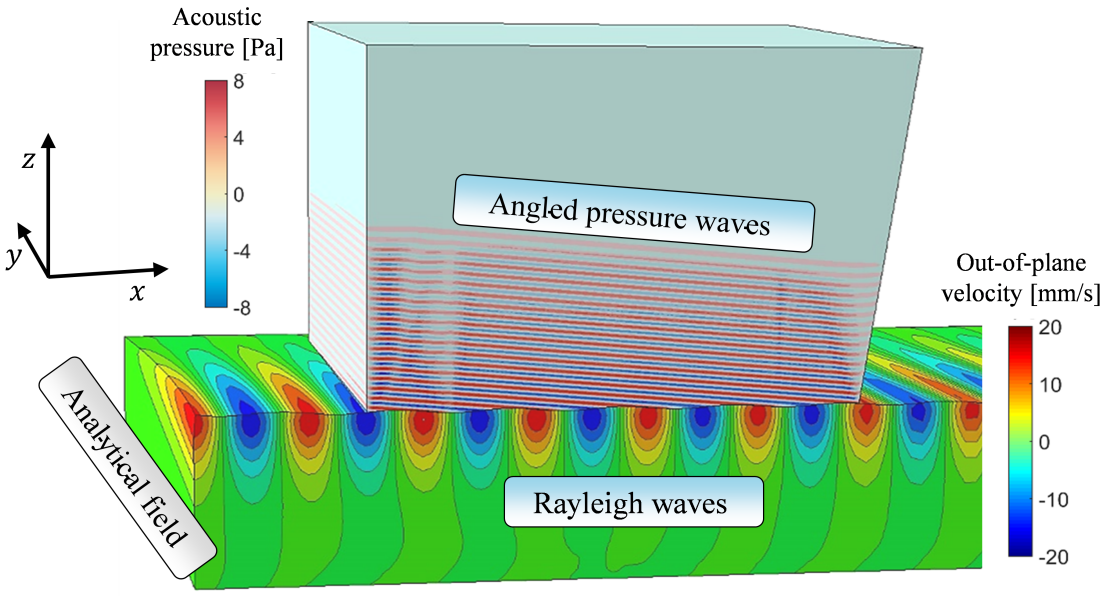

Figure 5.1: Simulation of an air column to determine attenuation effects

As in all of the other models, the symmetry condition is applied along the central plane. In order to get information about the two dimensional attenuation behavior, nodal output values are taken along the height and the width direction (z- and y-direction). This information allows the reconstruction of the actual pressure field at the receiver surface for both frequencies under investigation, which is shown in Figure 5.3. Due to the fact that ABAQUS/Explicit assumes a frequency independence of the volumetric drag coefficient δ within one simulation [37], the attenuation of the fundamental and the second harmonic component has to be investigated in two separate models.

The sound pressure profiles along the propagation distance l_{air} are shown in Figure 5.2 and compared to the analytical solution presented in Section 2.3. The initial pressure value at the surface of the solid ($z = 0$ mm) is calculated based on Equation (2.40) for the out-of-plane velocity $v_{z,R}$ extracted from a FE-model which uses the wedge excitation technique. The values correspond to a propagation distance x = 35 mm of the Rayleigh wave. For the fundamental velocity component a value

of 17.95 mm/s (at y = 0 mm) and for the second harmonic component 3.41 mm/s is obtained. This leads to initial sound pressures of $p_{0,1}^{analyt.} = 7.46$ Pa for the fundamental and $p_{0,2}^{analyt.} = 1.42$ Pa for the second harmonic component. Furthermore plots a) and b) both consider the Equations (2.42) and (2.43), presented for classical and high-frequency attenuation, as analytical reference. By comparison of the initial pressures at the surface, it can be seen that the FE-model predicts a slightly higher value for both the fundamental and second harmonic components ($p_{0,1}^{FE} = 7.73$ Pa and $p_{0,2}^{FE} = 1.52$ Pa). Concerning attenuation behavior, it is observed that the numerical values of both components decrease in a comparable range and fashion as the analytical solutions, and that the second harmonic decreases by far stronger than the fundamental frequency. The resulting attenuation coefficients α_1^{FE} and α_2^{FE} are calculated using the least square method in MATLAB to fit the numerical data. The values obtained are between the analytical references for each case. Table 5.1 summarizes the results of the coupled structural acoustic analysis, indicating a good agreement with corresponding analytical solutions.

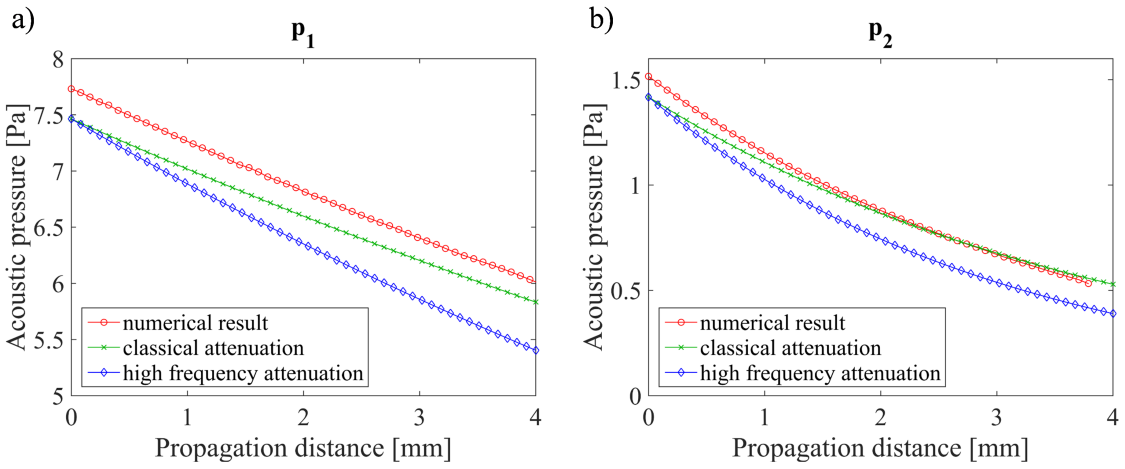

Figure 5.2: Attenuation of acoustic pressure for fundamental (a) and second (b) harmonic components

Table 5.1: Results of the coupled structural acoustic analysis and comparison to analytical values

	Analytical Result	Numerical Result
$p_{0,1}$(2.1 MHz) [Pa]	7.46	7.73
$p_{0,2}$(4.2 MHz) [Pa]	1.42	1.52
α_1 [Np/m]	classical 61.61 high freq. 80.70	62.78
α_2 [Np/m]	classical 246.47 high freq. 322.81	272.45
c_R [m/s]	2872.68	2865.33
c_{Air} [m/s]	344.00	344.80
θ [°]	6.88	6.90

5.1.2 Pressure Distribution at the Active Receiver Surface

Nodal output values along the $z-$ and the y-direction of the air column allow to approximate the arriving signal at the entire receiver surface in both the propagation and the width directions. Figure 5.3 depicts the resulting signal distribution of the receiver pressure $p_{rec,n}$. The dashed magenta line stands for the edges of the active receiver surface, showing a circle with a radius of 6.25 mm. It can be seen that the Gaussian shaped Rayleigh wave amplitude transforms into a Gaussian peak pressure profile at the receiver surface. As already shown in Figure 2.6, the angled adjustment of the receiver leads to an inconsistent distribution of the arriving pressure wave amplitudes along the propagation axis. In Figure 5.3, the origin is equivalent with the receiver center. The values of the propagation axis refer to this point, so that the largest positive value corresponds to the lowest point of the active receiver surface. There the highest pressure amplitudes are obtained because the propagation distance l_{air} is the smallest. Moving from this point into the negative direction means also gaining propagation distance and therefore a decreasing amplitude.

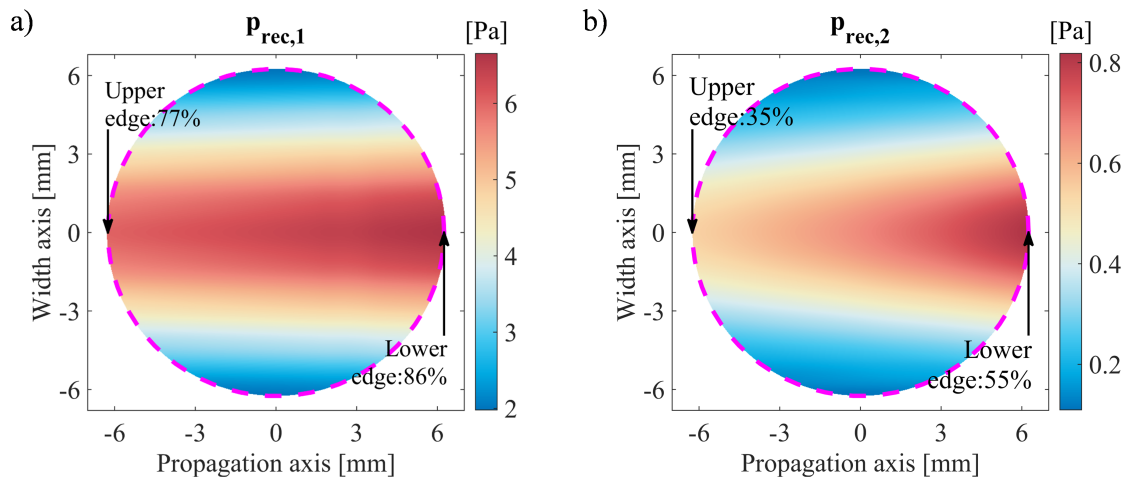

Figure 5.3: Arriving pressure amplitudes at the receiver surface for the fundamental (a) and second (b) harmonic component

The percent values in plots a) and b) of Figure 5.3 refer to the corresponding initial pressures $p_{0,1}$ and $p_{0,2}$. Since the attenuation of the second harmonic component is far higher than that of the fundamental, the discrepancy between the right edge in the figure (lower edge of the receiver) and left edge (upper edge of the receiver) is more significant (difference of 20 % in (b) compared to 9 % in (a)).

5.1.2.1 Weight Functions

For the correlation of experimental and numerical results the attenuation effects observed are taken into account. This is implemented by the use of weight functions, where the active receiver surface is projected onto the specimen surface, resulting in an elliptical profile. The referring weight ($W_n = p_{rec,n}/p_{0,n}$) for every discrete point within that ellipse is given by its ratio of pressure wave amplitude arriving at the receiver ($p_{rec,n}$) and the corresponding initial acoustic pressure ($p_{0,n}$) directly above the surface of the solid. Due to the short propagation distance and the plane character of the wavefronts, the diffraction of the leaked wave beam is neglected. This simplification means that the decrease of the pressure wave amplitude is not dependent on the width axis (y-direction).

5.2 Experimental Considerations

The main purpose of this research is to investigate experimental observations within the generated FE-model. Thus it is important to perform actual measurements to validate the model afterwards. This section considers the electrical output amplitudes A_1^{el} and A_2^{el} (see Section 3.2.2) which are called A_1 and A_2 for simplicity.

5.2.1 Amplitude Progression

In order to get information about both the one and two dimensional resolutions of the wave beams detected, the air-coupled receiver is moved along the propagation (2 mm increments) and the width axis (0.5 mm) (compare Figure 5.8 part b) and part c)). The generation of the final plots corresponds to the proceeding already described in Section 4.5. After the steady state portion of the time domain signal has been transformed into the frequency domain, the values for the fundamental harmonic (A_1) and the second harmonic (A_2) component are obtained. Those values are matched with their spatial position on the grid. Finally the results are interpolated on a finer grid to get a clearer picture.

Specimens with three different widths ("infinite", 25 mm and 18.5 mm) are investigated. To compare the results, all values are normalized to the corresponding fundamental amplitude at 25 mm propagation distance ($A_1(x$ =25 mm)), because the specimen of 25 mm width does not consist of stainless steel but of aluminum (see Section 3.1.1.5). Figure 5.4 depicts the wave beams of the fundamental (a) and the second harmonic (b) component. Furthermore, Figure 5.5 shows the corresponding profile of the ratio A_2/A_1^2. Note, that the color maps of the fundamental component are equal, while the color maps of the second harmonic component and of the ratio A_2/A_1^2 differ slightly. These figures clearly outline the influence of the specimen width.

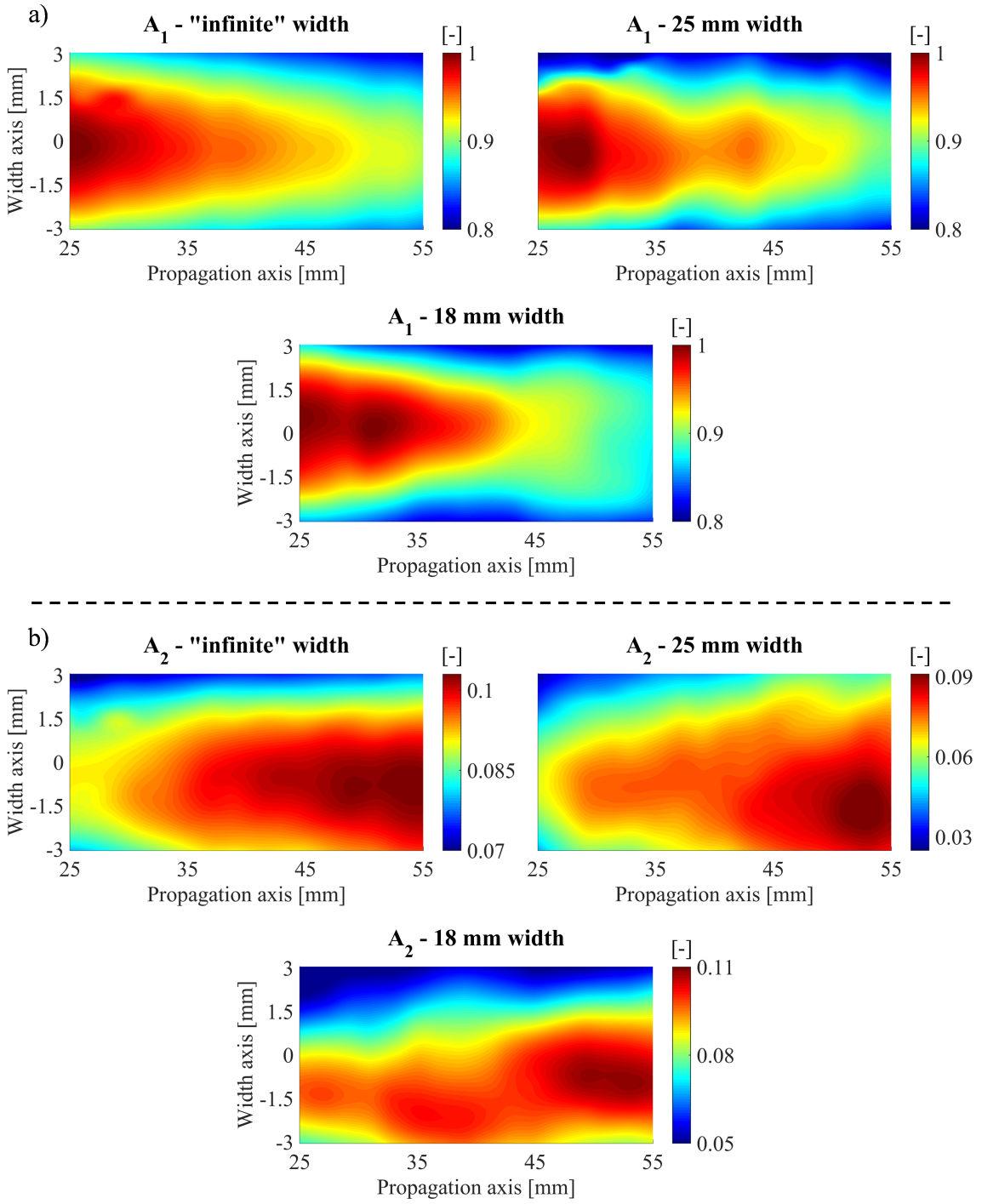

Figure 5.4: Experimental wave beams of fundamental (a) and second harmonic (b) components for specimen with different widths, normalized to the corresponding $A_1(x = 25 \text{ mm})$

For the "infinite" geometry a smooth profile for both A_1 and A_2 is obtained. The samples of 25 mm and 18.5 mm width respectively, show a variable behavior for both wave beam components. The diffraction of A_1 seems to be the most influenced, since the boundaries of the color scale do not decrease in the same linear fashion as in case of the "infinite" specimen. The 25 mm specimen indicates a more horizontal color boundary and the 18.5 mm sample does not show the classical Gaussian distribution along the width axis, but a double peak after a propagation distance of about 45 mm. Furthermore the amplitude decreases faster in case of the narrow sample, showing the smallest value at propagation distance of 55 mm.

The comparison between the two specimen of finite widths (25 mm and 18.5 mm) of the second harmonic wave beam A_2 imply a direction change in the case of the narrowest geometry which is not observed to that extent in the 25 mm sample. Furthermore the plot of the 18.5 mm width geometry shows, that A_2 does not increase consistently along the propagation axis but an oscillating behavior. This can be seen as the maximum values at around 30 mm and 40 mm are smaller than those at 25 mm and 35 mm.

The clearest evidence for the width influence is seen by comparison of the ratios A_2/A_1^2. The direction change of A_2 as well as the oscillations lead to two maxima in the contour plot of the 18.5 mm specimen which is not observable for the two other geometries. Thus, it is assumed that the smallest width considered, undergoes a critical value leading to inconsistent results in nonlinear ultrasonic Rayleigh wave measurements.

However, reflections of the specimen boundary cannot fully explain the oscillating profiles of A_1 and A_2 detected by the air-coupled receiver along the optical axis that are also observed by Morlock [23]. Furthermore Morlock shows, that there are considerably less oscillations when using another wedge for detection instead of the air coupled receiver [23]. In addition, the width of the specimen is still considerably larger

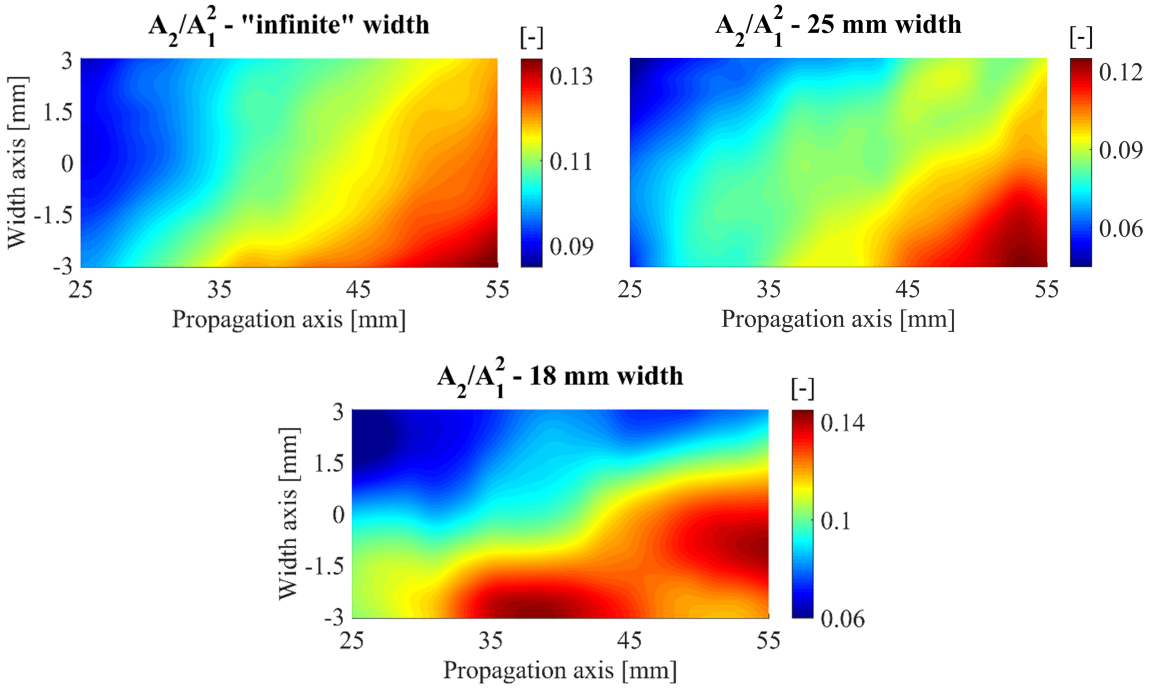

Figure 5.5: Resulting profile of the ratio A_2/A_1^2 of the experimental wave beams

than the width of the source (⌀12.7 mm transducer diameter) so that, theoretically, the influence of the boundary should be insignificant due to a energy concentration at the waveguide center for frequency-width products above 15 MHzmm as shown by Cegla [4]. In his paper he concluded, that for SH0 and A0 modes (the lowest order symmetric and antisymmetric lamb modes) nondispersive wave propagation without signal distortion is possible if a minimum width w_{min} of five times the shear bulk wavelength (λ_S) is exceeded (in the present case: $w_{min} = 5\lambda_S \approx 5(1.47\text{ mm}) \approx 7.37$ mm). Possible explanations for the experimentally observed behavior are derived from the numerical FE-model developed and presented in Section 5.4.2.

5.2.1.1 Angle between A_1 and A_2

The figures above show, that the maxima of the fundamental and the second harmonic components propagate along a different angle which contradicts the analytical

prediction (see Section 2.2.2), that the second harmonic is generated by the fundamental component. Coincidently the ratio A_2/A_1^2 in Figure 5.5 reaches its maximum value in the lower right corner in each case, resulting from a propagation path of the second harmonic component in the negative width direction compared to the fundamental component. A rotation of the data set of A_2 into the coordinate system of A_1 demonstrates the angle observation. Figure 5.6 shows the resulting plot for the specimen of "infinite" width.

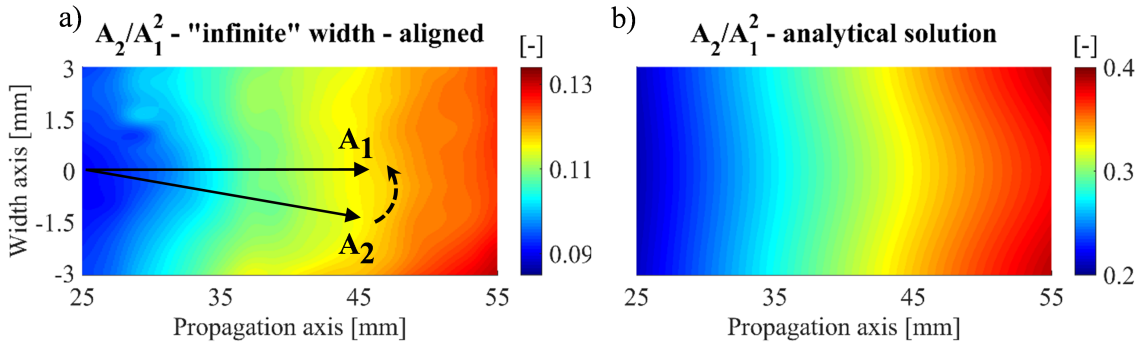

Figure 5.6: Resulting profile of the ratio A_2/A_1^2 after alignment of the propagation directions of the experimental wave beams (a) and analytical solution (b)

The alignment of the data sets, done with MATLAB, leads to a steady increase of the ratio A_2/A_1^2 along the entire specimen width, as predicted by the analytical solution (part b)) which is calculated based on the wave beams in Section 2.2.2. The reason for the phenomenon of the deviating angle is still unclear. There are theories that unsymmetrical effects, such as unsymmetrical clamping forces or an unsymmetrical pressure profile of the exciting transducer [18] could be the cause. Furthermore, unaligned source nonlinearities [17] should be considered, when trying to find an explanation.

5.2.2 Diffraction

An important part of the model derivation is the consideration of diffraction. Shull [32] proposes a parabolic approximation for small diffraction angles as shown in Section 2.2.2. Due to the two dimensional surface scan with the air-coupled receiver, it is possible to determine the Gaussian beam width of the detected wave beams. Figure 5.7 shows the results for two different experiments ("exp1" and "exp2") indicating a qualitatively similar diffraction pattern but quantitative differences. Apparently the values of experiment 1 are higher for both A_1 and A_2 along the propagation distance. This plot implies, that there is a strong dependence of A_2 on A_1 not only concerning the peak amplitudes of the wave beams along the propagation distance, but also on the width a. Furthermore it is clearly indicated, that the width of A_2 is considerably smaller than the width of A_1 lining up with Shull's analytical prediction (see Section 2.2.2). Besides the experimentally determined diffraction profiles, Figure 5.7 also shows a fit to the mathematical description of the Gaussian beam expansion written as follows:

$$a(x) = a_0\sqrt{1 + (x/x_0)^2}, \tag{5.1}$$

where $x_0 = k_0 a_0^2/2$ is the Rayleigh distance depending on initial source half width a_0. In order to reach a sufficient fitting quality, an additional offset value has to be introduced to Equation (5.1) as a parameter which is also given in Figure 5.7. The result of the best fitted curves are indicated in the legend. It shows, that the values are in the same range. The average Gaussian half width of the source a_0 of the two results is $a_{0,1} \approx 5.73$ mm for the fundamental and $a_{0,2} \approx 3.70$ mm for the second harmonic component. The observation of the required addition of an offset leads to the conclusion, that the width detected by the air-coupled receiver differs from the actual width of the wave beams in the sample. The assumed reason for this offset is most likely caused be the averaging of the non-contact receiver described in detail in Section 5.3.

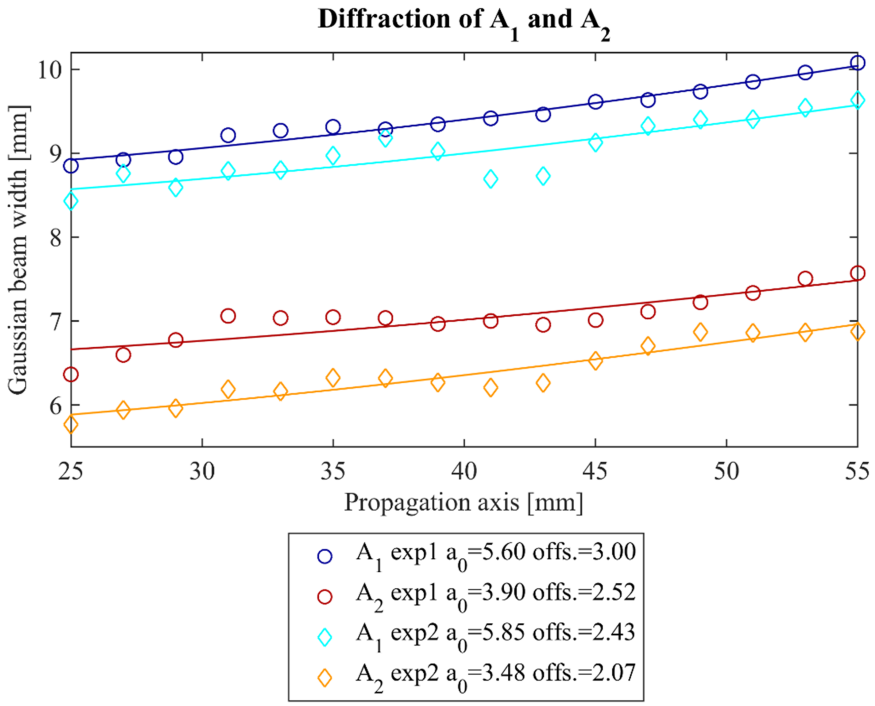

Figure 5.7: Diffraction of the experimental wave beams

5.3 Influence of the Air-Coupled Receiver

This section provides a link between the experimental results obtained by the air-coupled receiver, and FE-model data. To compare experimental results from the previous section with the numerical FE-results in Section 5.4, inherent properties of the air-coupled receiver have to be considered, such as:

1. The receiver averages the incoming signal; and
2. attenuation of the detected pressure waves is frequency dependent.

Convention Since the amplitude of the pressure waves depends on the out-of-plane particle velocity (see Section 2.3), this value is taken and interpreted in the case of the transient dynamic analysis. For reasons of simplicity the out-of-plane particle velocity amplitudes are named A_1 for the fundamental component and A_2 for the second harmonic component in the following sections.

5.3.1 Transformation into the Receiver "Perspective"

The non-contact receiver has an active surface of ∅12.5 mm and a planar beam configuration [43], meaning that it does not have an adjusted focal point. Thus, the output signal of the receiver reflects the sum of the arriving pressure waves at the active surface, and not that of a point measurement along the optical axis. Consequently, the output signal of a smaller receiver has a significantly smaller amplitude than that of a larger receiver, as observed in nonlinear measurements.

In order to compare and validate the numerical results with the experimental observations, it is essential to transform the wave fields obtained by the FE-model into the air-coupled receiver's "perspective" considering the effects mentioned above. This is done by a numerical integration performed with MATLAB, projecting the active receiver surface (∅12.5 mm) onto the specimen surface. Figure 5.8 shows this procedure. The resulting ellipse is moved forward (propagation axis) and sideways (width axis) over the wave field in discrete steps as performed during an experimental measurement. Thereby the values within the ellipse are integrated numerically and weighted by a specific weight function based on attenuation and diffraction effects of the pressure waves in air (see Section 5.1.2.1). Considering the bending stiffness of the receiver surface [18], it is assumed that the waves arriving at the receiver center have a higher influence on the output signal than the portions arriving close to the edge. This assumption is implemented by a second weight function in shape of a Gaussian bell leading to a factor of 1 in the center and 0.75 at the edges.

The specifically weighted values are averaged, resulting in a single point value for the fundamental and the second harmonic component (as indicated by the "×"-markers). Consequently one "×"-marker corresponds to one numerical integration with the air-coupled receiver centered at the specified axis position. The analytical reference wave fields (no markers) used to demonstrate the effect correspond to those presented in Section 2.2.2. The propagation distance considered in part b) is the same as in the

experimental measurements (see Section 5.2) and amounts to 25 - 55 mm (referring to the receiver center). The width axis (part c)) shows higher values than experimentally investigated due to purposes of presentation. All of the values depicted are normalized to the maximum of the corresponding fundamental (at 25 mm propagation distance) to outline the qualitative changes caused by the point-to-average transformation ("×") and to make a comparison to the experimental values later on, where only the information at the propagation distance of 25 mm is given. The curves of the fundamental wave components refer to the blue, primary y-axis and those of the second harmonic wave components to the red, secondary y-axis.

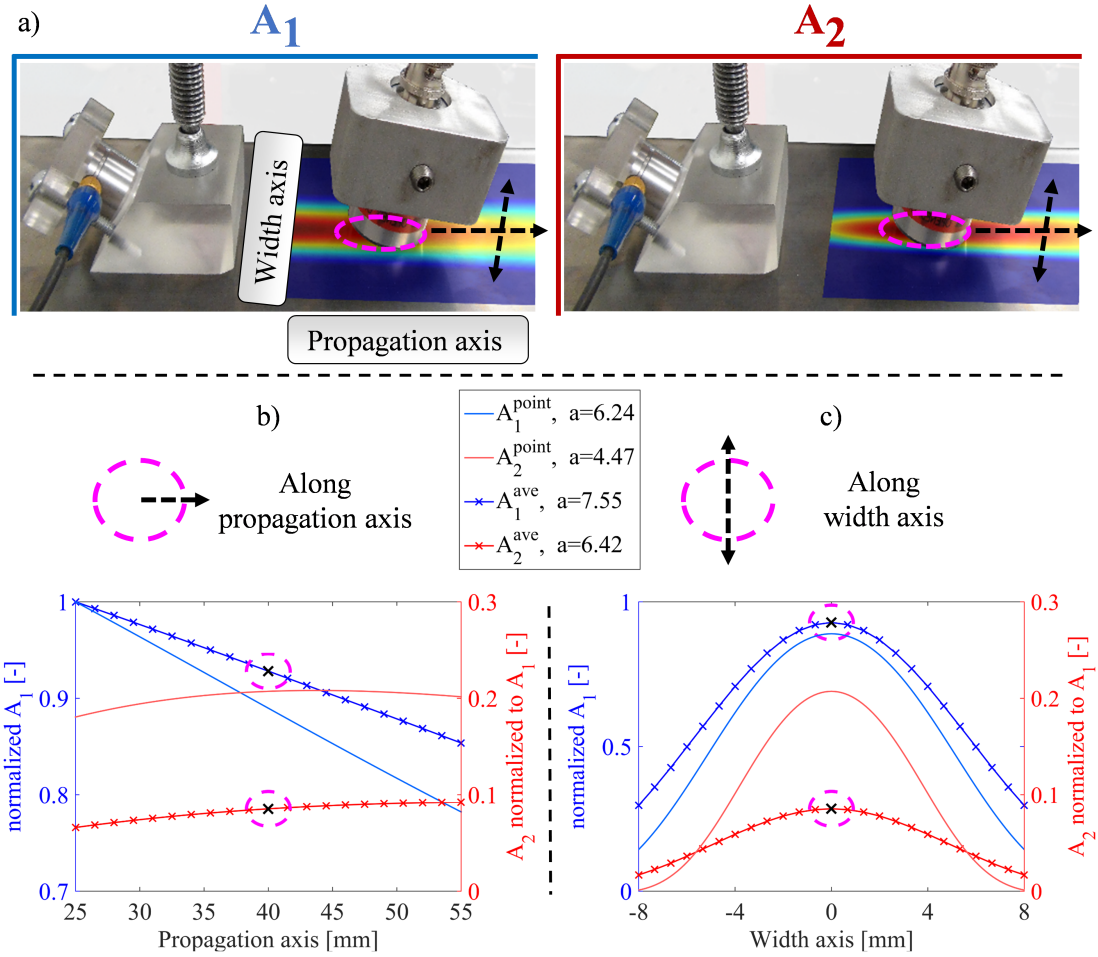

Figure 5.8: Influence of the air-coupled receiver on the measured amplitudes along propagation (a) and width (b) axis

Along the propagation axis (part b)) it is observed that the transformed, averaged fundamental component A_1^{ave} decreases more slowly than the analytical point solution A_1^{point}. For the second harmonic, the differences are even more pronounced, moving the maximum of the curve progression to a higher propagation distance in case of the transformed profile A_2^{ave}. Furthermore, the ratio of the fundamental (A_1^{ave}) to the second harmonic (A_2^{ave}) amplitude is influenced considerably as described in detail in Section 5.4.1.2. However, the shape of the wave beams are not only affected along the propagation axis, but also along the width axis. This is of essential importance for the investigation of the diffraction behavior as investigated in Section 5.4.1.1. The averaging of the air-coupled receiver leads to a significantly larger beam width a_n (1.3 mm for A_1 and nearly 2 mm for A_2) than the underlying wave beams actually have. This is considered with the offset, fitting the experimentally determined diffraction values to the analytical prediction (see Section 5.2.2).

Figure 5.9 shows the wave beams of the fundamental (part a)) and the second harmonic (part b)) components before and after the point-to-finite area transformation. The differences described above are highlighted by these two dimensional plots. The radius of the active receiver surface (6.25 mm) has to be subtracted from both sides in the width dimension of the "point" plots because the edge of the receiver does not exceed the boundaries of the underlying wave field. For the fundamental components A_1^{point} and A_1^{ave} the deviating decrease in amplitudes is observed again, since the point measurement decreases more strongly. In the case of the second harmonic components A_2^{point} and A_2^{ave}, the significantly higher values for the point measurement even require a different color scaling. Furthermore the fact that the maximum is reached at different propagation distances is outlined clearly. According to the color scale, the transformed profile A_2^{ave} shows a maximum at 55 mm, while the point profile reaches its highest value at 43 mm already.

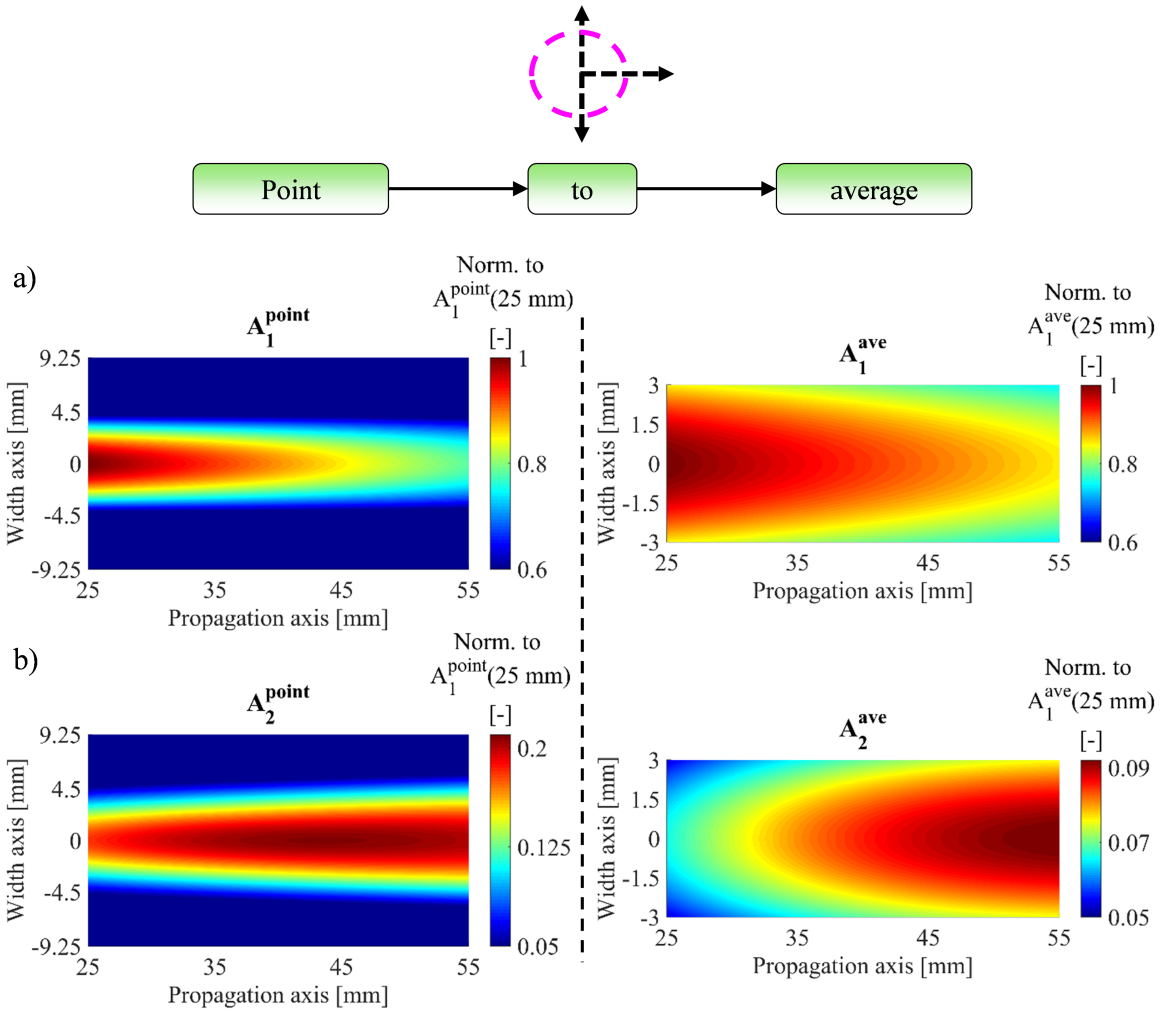

Figure 5.9: Influence of a point-to-average transformation on the wave beams of fundamental (a) and second harmonic (b) component

These results lead to the conclusion, that the air-coupled measurements performed for a given experimental setup, differ considerably from point measurements on the same specimen (of e.g a laser receiver). The difference between the point and averaged receiver is quantified in Section 5.4.1.2 for the case of the numerical FE-model. This derivations influence the material model implemented in ABAQUS, as described in Section 4.5.2.

Note, that if we apply the equation ($\mathrm{N} = r^2/\lambda_{air}$) for the near field distance N of a piston transducer with radius r, the given values lead to N = 238.463 mm which is

orders of magnitudes larger than the lift of distance $l_{off} = 3$ mm of the air-coupled receiver. Since the character of the leaked pressure waves is planar, near field effects are not as large as they would be for a point source [8]. Near field effects of the air-coupled receiver are not considered in the code developed in this research.

5.4 Numerical Description of Nonlinear Rayleigh Waves

This section considers the results of the nonlinear Rayleigh wave simulations. In the first part, the model is validated by the experimental observations using the tools developed above. In the next step the generated model is applied to the narrow sample, investigating differences in the behavior of the propagating Rayleigh surface waves.

5.4.1 Experimental Validation

The comparison between experiments and FE-model is done by diffraction behavior and amplitude progression of the first and the second harmonic components along the propagation distance of 25 - 55 mm corresponding to available experimental data. Those are the two Rayleigh wave attributes considered in the process of model optimization (see Section 4.5.2).

5.4.1.1 Diffraction

As previously pointed out in Section 5.2.2, diffraction or more specifically, the beam width detected with the air-coupled receiver differs from the analytical description of the Gaussian beam. Thus, it is necessary to transform the numerical values into the air-coupled receiver "perspective" to make a comparison. Figure 5.10 shows the Gaussian width of the wave beams dependent on the propagation distance, for the nodal ($\widehat{=}$point) FE-output values A_n^{point} (no markers), the transformed, averaged nodal values A_n^{ave} ("$\times$"-markers) and the experimental data A_n^{exp} (experiment 1 in Figure 5.7; "$\circ$-markers") for both fundamental and second harmonic components.

The influence of the transformation into the receiver "perspective" is clearly visible for both components. The profiles progress at considerably higher values after the point-to-average transformation ("×") than before, and are therefore closer to the experimental data ("○"). By comparison, it shows, that the fundamental amplitude A_1^{ave} is smaller than this experimental counterpart A_1^{exp}, whereby the data of the second harmonic components match well (A_2^{ave} and A_2^{exp}).

A comparison of the nodal (point) A_n^{point} (no markers) and the transformed, numerical A_n^{ave} values ("×"-markers) shows, that the averaging of the receiver also effects the "slope" of the profiles. The transformed curves increase less with propagation distance and thus, agree better with the experimental counterparts. Overall, the point-to-average transformation leads to a match of more than 90 % for both amplitudes. Consequently it is assumed that the diffraction of the simulated wave is close to the "real" wave captured in the measurements. This is an essential finding concerning the investigation of boundary influence in the subsequent steps (see Section 5.4.2).

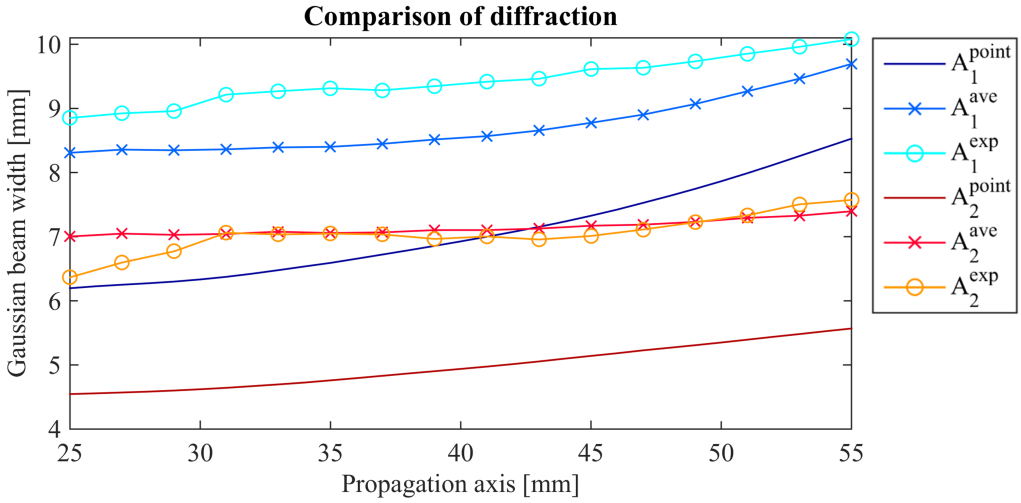

Figure 5.10: Comparison of diffraction of numerical point, averaged numerical and experimental wave beams

5.4.1.2 Amplitude Progression

The amplitude progression of the first and the second harmonic wave component is the other important Rayleigh wave attribute to predict with the numerical FE-model. The fundamental tool for the comparison is again given by the point-to-average transformation code, which considers the influence of averaging and attenuation of the pressure waves leaked by the specimen surface. Figure 5.11 shows the numerical values before (A_n^{point}; no markers) and after the transformation into the air-coupled receiver "perspective" (A_n^{ave}; "×"-markers). Part a) of Figure 5.11 considers the amplitudes and part b) the ratio $A_2/A_1^2 \propto \beta x$ and the corresponding slope which is taken to quantify the material nonlinearity in measurements. The experimental values ("∘"-markers) in Figure 5.11 refer to the "infinite" geometry in Section 5.2. In order to compare experimental (output in Volts) and numerical FE-data (output in mm/s), all of the profiles depicted are normalized to the maximum of the corresponding fundamental amplitude $A_1^i(25\ mm)$. Consequently the distributions for the first harmonic all start at a value of 1.

Again, the influence of the point-to-average transformation ("×") is clearly observable both quantitatively and qualitatively. For A_1^{point}, the absolute value of the slope is higher than for A_1^{ave} and for A_2^{point} the maximum is reached considerably earlier than for A_2^{ave} (43 mm compared to 51 mm). The quantitative difference manifests in the ratio of the fundamental and the second harmonic components. The "gap" between A_1^{ave} and A_2^{ave} is significantly larger than the "gap" between A_1^{point} and A_2^{point}, which is mainly explainable by the different attenuation coefficients in air for the fundamental and the second harmonic pressure waves (see Section 5.1.2.1). Thus, the signal of A_2 attenuates much stronger than that of A_1. As in the case of diffraction the point -to-average transformation is necessary to match experimental results. This statement is emphasized when considering part b) in Figure 5.11. Before the transformation, both absolute values and slope of the ratio $A_2^{point}/(A_1^{point})^2$ are far

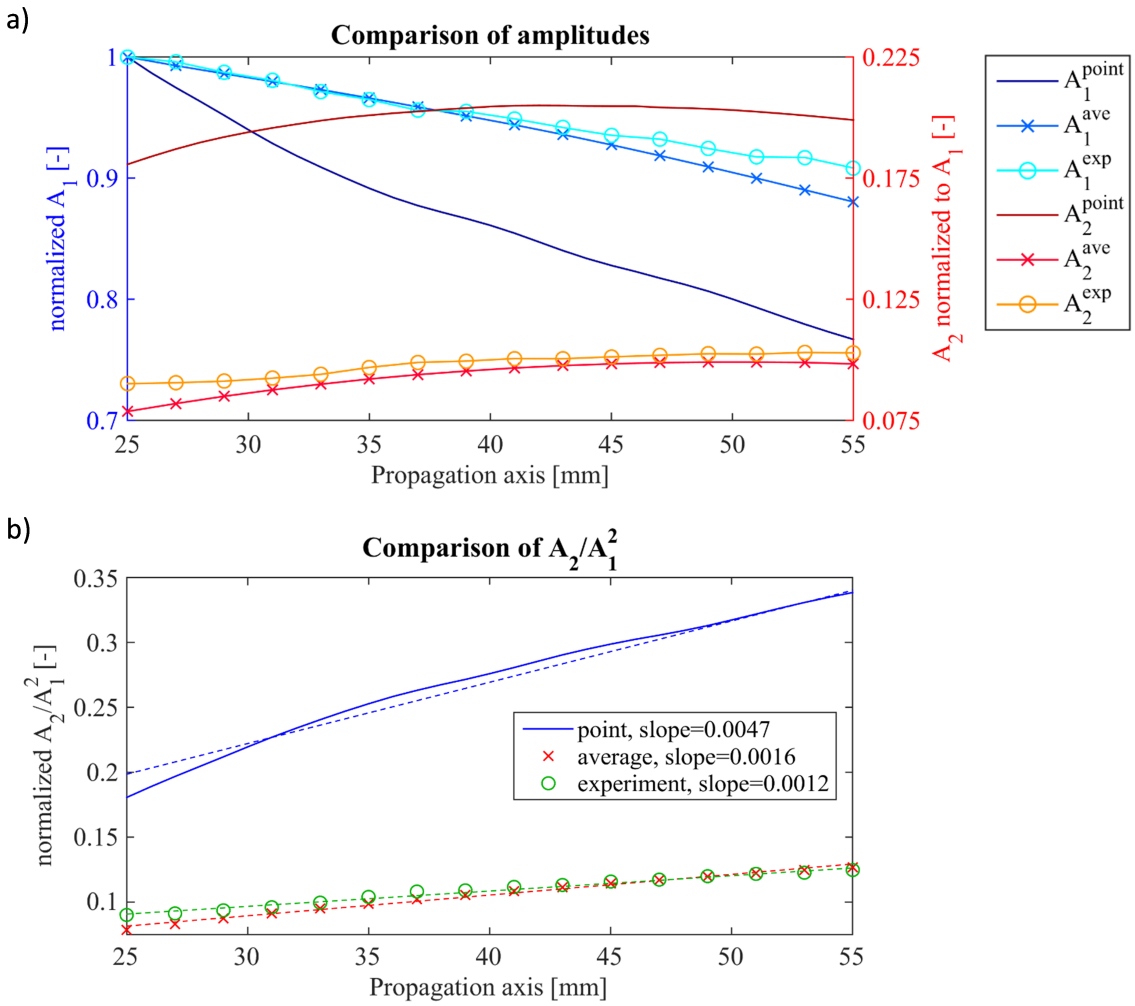

Figure 5.11: Comparison of amplitude profiles (a) and resulting ratio A_2/A_1^2 (b) of numerical point, averaged numerical and experimental values

higher than in the experiment ("○"). After the averaging ("×"), however, the values match to a large extent whereby the slopes still differ by about 25 %.

These results not only show that the numerical model as a whole is able to describe the nonlinear measurements, but also how important it is to consider the inherent characteristics of air-coupled measurements if absolute nonlinear values want to be taken. This is previously mentioned by Thiele [44].

5.4.2 Influence of the Specimen Width

The properties of the validated model for the quasi "infinite" lateral extension is now applied on the problem of inconsistent amplitudes identified in narrow specimens. Special focus is given on the oscillating effects which could explain the experimental observations with the air-coupled receiver, previously shown by Morlock [23].
Thereby two possible causes are investigated. The first is rather straight forward, and considers a change in the out-of-plane velocity which directly correlates with the leaked pressure waves. The second consideration evaluates the boundary influence on the shape of the Rayleigh wavefronts. This is based on the fact that the direction of the surface waves determines the normal vector of the leaked pressure waves. Thus, a plane wave along the entire propagation distance is desired in order to obtain plane angled pressure waves over the entire specimen width.

5.4.2.1 Influence on the Out-of-Plane Velocity

Consideration of the out-of-plane velocity clearly indicates differences between the specimen of "infinite" and narrow width (18.5 mm). Figure 5.12 shows the amplitude progression along the optical axis for both the fundamental (A_1) and the second (A_2) harmonic component. Minor variations for both amplitudes are observed as far as the narrow specimen is concerned, whereby there are more variations in case of A_2. This occurs immediately after the wedge tip (up to 15 mm propagation distance) and after the maximum value is achieved (> 50 mm propagation distance). Furthermore Figure 5.12 indicates that the maximum value for A_2 is reached at a smaller propagation distance in case of the narrow specimen (41 mm compared to 43 mm). Additionally there is a more significant decrease in amplitudes visible not only for A_2 but also for A_1 in case of the 18.5 mm width sample. This result matches that of experimental data. Apparently the restricting boundary even affects the wave propagation behavior along the optical axis, which has a distance of 9.25 mm from the edge. However,

Figure 5.12 shows, that the effect of a narrow width is minor for the propagation distance up to $\sim$ 50 mm, if the source coupling is perfect and the measurement along the optical axis is accurate.

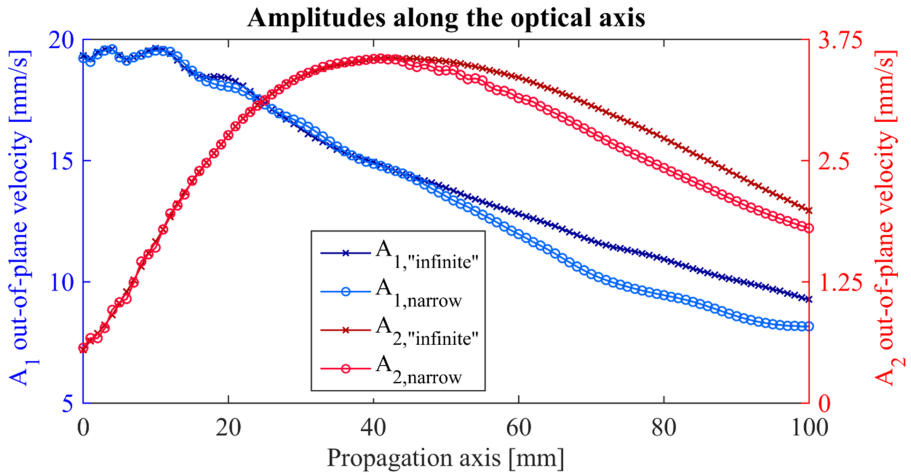

Figure 5.12: Amplitude progression of the first (primary y-axis) and second (secondary y-axis) harmonic components along the optical axis for "infinite" and narrow geometry

The contour plots in Figure 5.13 show the two dimensional progression of the wave components for A_1 (part a)) and for A_2 (part b)). The bottom of the figure (part c)) relates the amplitude profiles for the narrow and "infinite" models by a superimposition of the two datasets ($A_{i,narrow}/A_{i,\text{“}infinite\text{”}}$). The figures of each part a), b) and c) refer to the same color scale (on the right) and the same width axis (on the left). The comparison of the fundamental velocity amplitudes along the propagation distance (part a)) highlights a double peak in case of the narrow geometry, while the "infinite" counterpart shows the smooth Gaussian profile with a parabolic diffraction as predicted by the analytical solution in Section 2.2.2. The double peak for the fundamental amplitude $A_{1,narrow}$ directly mirrors the observed behavior in the second harmonic $A_{2,narrow}$ contour plot, which is a proof of the assumption that A_2 is generated by A_1. The phenomenon of the double peak was also observed in the experiments (see Figure 5.4) for the fundamental component, but could not be shown

for the second harmonic. A possible explanation is the averaging characteristic of the receiver which was presented in the previous Section 5.3. For the fundamental amplitude $A_{1,narrow}$, the two peaks are by far more pronounced than for the second harmonic $A_{2,narrow}$ and thus, also visible in the receiver "perspective". However, as the importance of an precisely aligned receiver head, according to the propagation axis of the wave is emphasized by Thiele [44], it is assumed that the double peak affects the calibration and thus the measurement quality adversely. On top of that, Thiele [44] shows, that an unaligned receiver causes oscillating experimental results in amplitude progression.

To quantify the differences along the entire propagation distance more precisely, the profiles of "infinite" and narrow specimen are superimposed, dividing the values of the narrow wave guide by the corresponding "infinite" data point ($A_{i,narrow}/A_{i,\text{“}infinite\text{”}}$). Consequently, a value larger than 1 indicates a higher out-of-plane velocity of the narrow sample. Note, that the color scale of the figures is not complete for presentation reasons. These superimpositions in Figure 5.13 c) highlight significant differences caused by the restricting boundary, which are not visible to that extent in the out-of-plane velocity amplitude plots above. Both superimpositions of the fundamental (left) and the second harmonic (right) components show a more than ± 40 % variation. The boundary influence is already observable at very small propagation distances, indicating that the wave field is immediately disturbed leaving the wedge. In the case of the ratio $A_{1,narrow}/A_{1,\text{“}infinite\text{”}}$, local near field like maxima are visible, and for the ratio $A_{2,narrow}/A_{2,\text{“}infinite\text{”}}$ the minor variations almost extent over the entire specimen width. The simplification of an equally distributed Gaussian line source along the wedge tip, as described in the analytical solution (see Section 2.2.2) and shown by laser point measurements of Torello [46], appears to be affected adversely by the narrow specimen geometry. This most likely has negative effects on the wave propagation in the entire specimen.

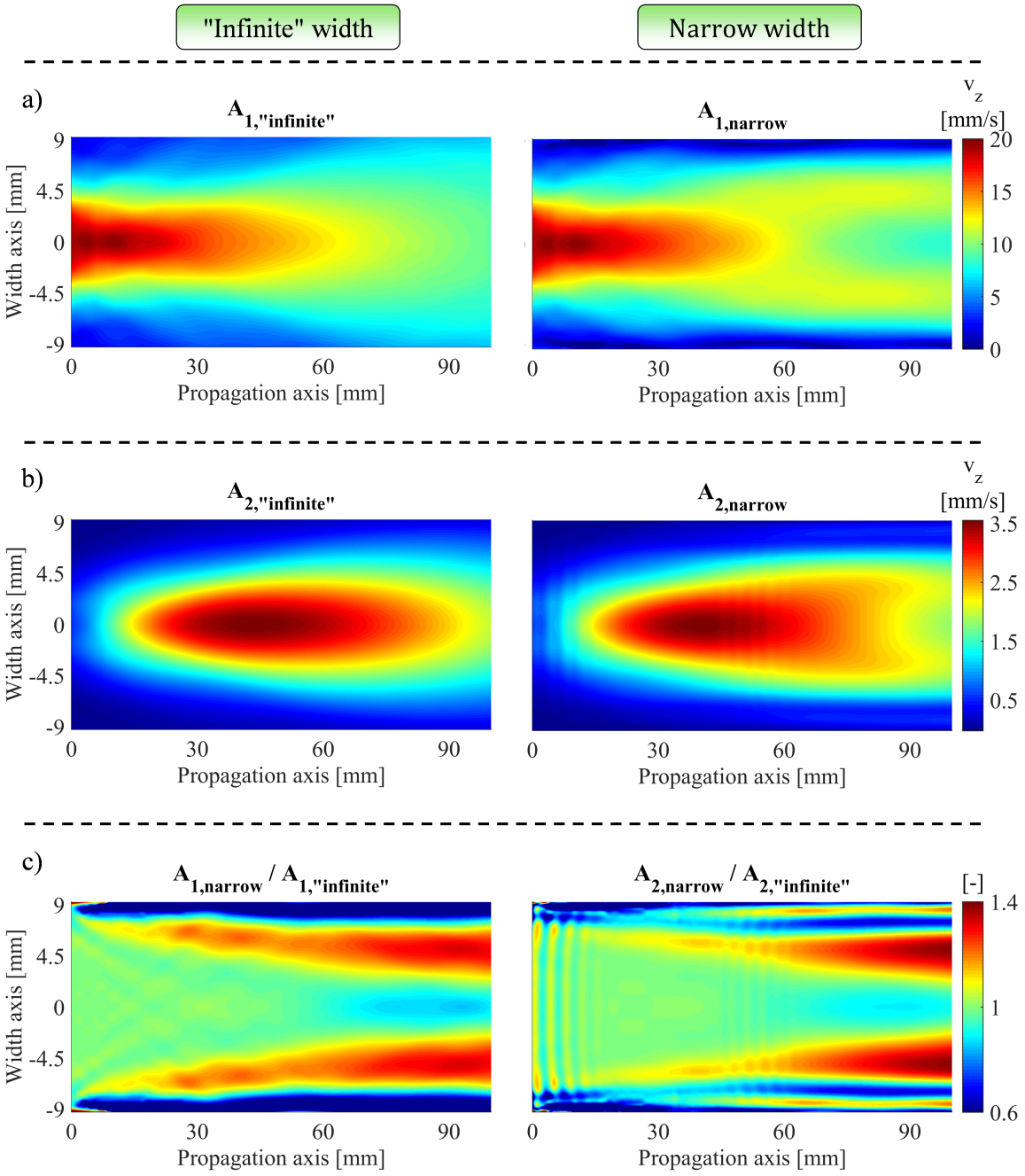

Figure 5.13: Amplitude profiles of the first (a) and the second (b) harmonic components and superimposition (c) for "infinite" and narrow geometry

The superimpositions also show the double peaks very clearly. These are observed as red stripes at a with of ± 5 mm, widening in propagation direction. Between those

peaks there is a local minimum (value < 1) identified along the optical axis for both of the plots in part c). This observation correlates with the amplitude progression at the center of the waveguide, as already shown in Figure 5.12. The double peaks are shown very clearly in part c) of the figure, as an increasing value larger than 1 along the propagation distance. Furthermore it shows, that there is a local minimum (value < 1) between the peaks (optical axis) which is quantified in Figure 5.12. Most important is the behavior close to the boundaries. The ratio $A_{1,narrow}/A_{1,\text{“}infinite\text{”}}$ shows a minimum extending along the entire propagation distance which cannot be observed in the ratio $A_{2,narrow}/A_{2,\text{“}infinite\text{”}}$ of the second harmonic out-of-plane velocity amplitudes. At around 50 mm propagation distance, a narrow orange-red stripe indicates a local maximum in the $A_{2,narrow}/A_{2,\text{“}infinite\text{”}}$ contour plot and thus a larger second harmonic amplitude for the 18.5 mm width specimen. This difference outlines that the restricting geometry affects the spatial causality of the first and its generated second harmonic which is an essential condition for consistent nonlinear ultrasonic measurements.

However, those differences described above, cannot be entirely responsible for the oscillating amplitudes observed in experimental results. Therefore, the plane wave approximation is investigated more closely in the following.

5.4.2.2 Influence on the Shape of the Rayleigh Wavefront

The shape of the Rayleigh wavefront is critical in air-coupled measurements because it determines the normal vector of the pressure waves leaked into the air. A flat or locally flat Rayleigh wavefront forms plane, uniform pressure waves detectable with the non-contact receiver which has a flat surface. Consequently any deviation from the plane wave approximation affects air-coupled measurements adversely. In order to determine the shape of the Rayleigh wavefronts the parameter $\Delta\tilde{x}$ which is derived in the next paragraph is used.

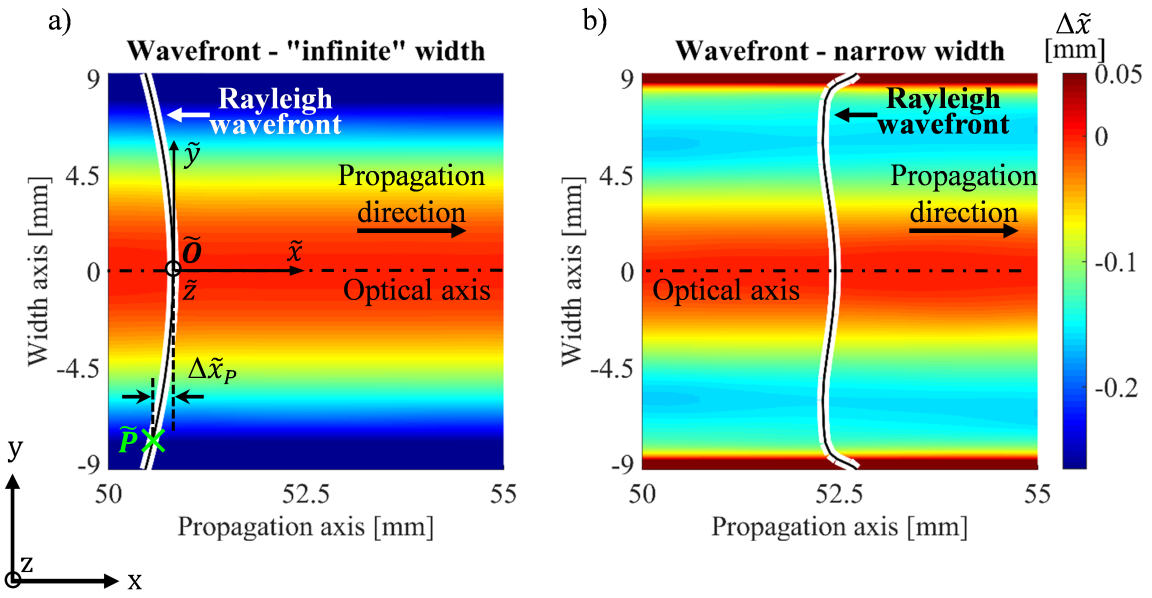

Figure 5.14: Relative distance in propagation direction $\Delta\tilde{x}$ of a single Rayleigh wavefront in the "infinite" (a) and the narrow (b) geometry

Figure 5.14 a) shows a single Rayleigh wavefront propagating in the positive, global x-direction without a restricting boundary. To get the relative distance in propagation direction $\Delta\tilde{x}_P$ of a point $\tilde{P}$ "on" the wavefront to the wavefront center $\tilde{O}$, a local reference coordinate system $(\tilde{x}, \tilde{y}, \tilde{z})$ is defined whose origin $\tilde{O}$ moves with the wavefront in the positive global x-direction. Thus, in the case of a plane wave $\Delta\tilde{x}_P$ equals zero for any point $\tilde{P}$, since $\tilde{P}$ is in line with $\tilde{O}$. However, Figure 5.14 a) indicates that the Rayleigh wavefront has a curved profile. Therefore, $\Delta\tilde{x}_P$ increases as the distance between $\tilde{P}$ and the optical axis increases. The color map quantifies this relative distance in propagation direction $\Delta\tilde{x}$ along the local $\tilde{y}$ axis. The color bar is given on the right of Figure 5.14. A color value of orange or darker stands for a part of the wavefront traveling behind its center ($\Delta\tilde{x} < 0 \rightarrow$ relative lag) and a color value of dark red means, that the corresponding part of the wavefront is ahead of its center ($\Delta\tilde{x} > 0 \rightarrow$ relative lead), which is usually only observed in the near field. Note, that the color map is not complete for presentation reasons. For the given

width position of $\tilde{P}$, a relative lag of ≈ 0.2 mm ($\Delta\tilde{x} \approx -0.2$ mm) to the wavefront center $\tilde{O}$ is indicated. For an increasing time t, the local coordinate system $(\tilde{x}, \tilde{y}, \tilde{z})$ moves along the propagation direction. Thus, the color map shows the quantitative evolution of the defined parameter $\Delta\tilde{x}$ and consequently the evolution of the shape of the Rayleigh wavefront along the propagation distance x.

The value $\Delta\tilde{x}$ is determined by the local time difference Δt which can be calculated from the difference in arrival times $\Delta t = t_{\tilde{O}} - t_{\tilde{P}}$ for a certain position $\tilde{O} = x$ referring to the global reference frame (x, y, z). From this, $\Delta\tilde{x}$ is obtained by multiplying the local time difference Δt by the Rayleigh wave speed c_R. For the signal processing the "findpeaks" function of MATLAB is used. Note, that the maximum positive value is defined by $\Delta\tilde{x}_{max} = 1/4\lambda_R \approx 1.36$ mm$/4 \approx 0.34$ mm. Any larger distances represent the next wavefront in the propagating tone burst.

Besides the wavefront in the "infinite" geometry, Figure 5.14 b) also shows the corresponding wavefront at a similar propagation distance for the narrow 18.5 mm width waveguide. The comparison highlights significant differences. The wavefront in the narrow geometry is considerably distorted and does not show a homogeneous decrease (increasing negative values) of $\Delta\tilde{x}$ as the "infinite" reference does. At the specimen's edges, there is even a relative lead ($\Delta\tilde{x} > 0$) observed which implies a strong wavefront-boundary interaction. The color scaling shows that the wavefronts are not strongly influenced within a specimen width of $y \approx \pm$ 3.5 mm. In this area plots of the"infinite" and the narrow width geometry display nearly no relative distance in propagation direction ($\Delta\tilde{x} \approx 0$) and thus indicate locally flat, plane wavefronts. Moving further outside the color scaling indicates a progressively greater affected shape of the wavefront.

Figure 5.15 shows the contour plot of the evolution of $\Delta\tilde{x}$ along the entire propagation distance of 100 mm (without wavefronts). The color scale corresponds to that in Figure 5.15. In both cases near field effects are observable in form of a $\Delta\tilde{x} > 0$

which can be seen between 0 - 15 mm propagation distance. As can be observed, the near and far field transition happens around a 30 - 40 mm propagation distance only, since a steady state is reached for the "infinite" geometry. The near field effects are far more pronounced in the narrow geometry (part b)), as a result of the already influenced wave field beneath the wedge. As described above, the smooth (red) profile is considerably thinner between 30 - 70 mm propagation distance but widens tremendously at the end, which most likely corresponds to the double peaks observed in the previous section. This observation agrees with the minor influence of the restricting boundaries along the optical axis up to a certain propagation distance, as already found in the amplitude progression. Overall, the contour plot of the narrow geometry shows by far more variations than the "infinite" reference, indicating that the boundaries considerably hinder the propagating waves. Additionally, major oscillating disturbances extend along the entire narrow specimen's edges. A frequently changing lead and lag is observed (oscillating red and blue areas along the edges of Figure 5.15 b).

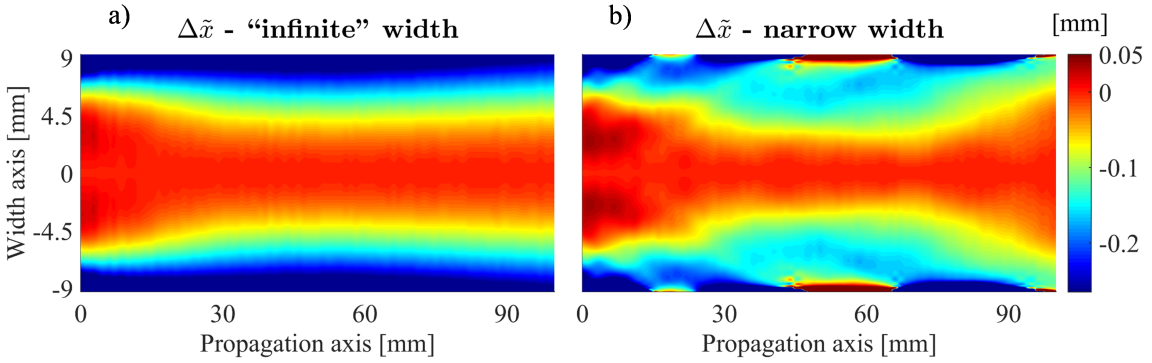

Figure 5.15: Evolution of the relative distance in propagation direction $\Delta\tilde{x}$ of a Rayleigh wavefront in the "infinite" (a) and the narrow (b) geometry

These oscillations originate from a recurring "attaching" and "releasing" of the wavefronts from the sample edge, which is seen in Figure 5.16. This figure shows a simulated tone burst with a steady state of 20 waves propagating in positive $x-$direction

in the narrow geometry. The color scale refers to the out-of-plane velocity. Within the tone burst there are three different Rayleigh wave-boundary interactions observed:

1. A relative lag, $\Delta\tilde{x} < 0$;
2. a transition zone with no wavefront-edge connection; and
3. a relative lead, $\Delta\tilde{x} > 0$.

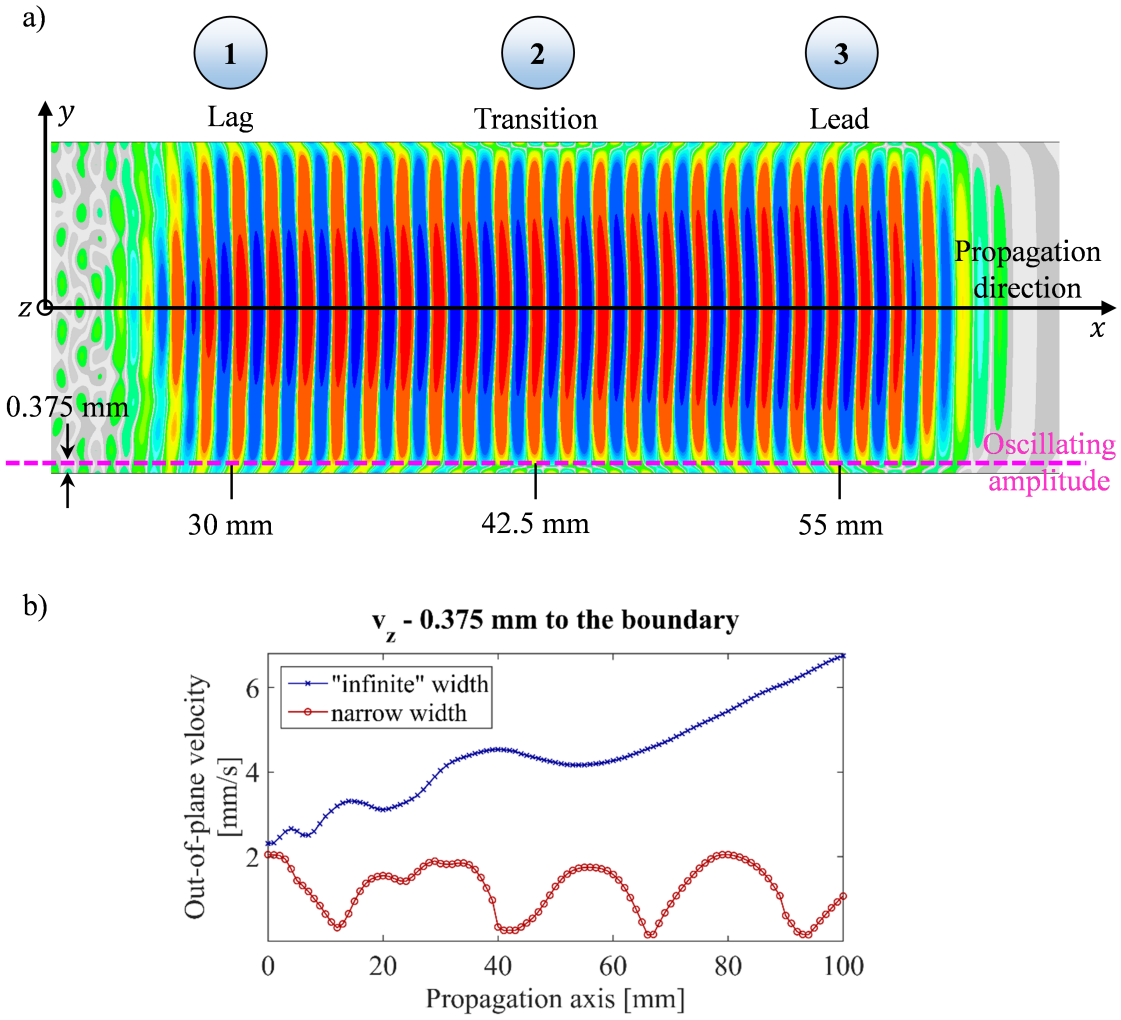

Figure 5.16: Oscillating interaction with the specimen's edges in the case of the narrow width geometry

Part a) of Figure 5.16 furthermore implies an oscillating amplitude close to the edge, because the out-of-plane velocity is $v_z \approx 0$ mm/s in the transition area. The plot in part b) shows the out-of-plane velocity v_z along the indicated magenta line

which is at a distance of 0.375 mm from the edge. The corresponding out-of-plane velocity values in the case of the "infinite" geometry are shown as a reference. The comparison shows major differences. While the "infinite" reference indicates the classical diffraction behavior with an increasing amplitude after the near and far field transition, the narrow sample shows oscillating amplitudes over the entire propagation distance. This effect indicates that guided waves are formed due to the boundary on both sides.

Correlation to Leaked Pressure Waves To connect the oscillating shape of the wavefronts and the oscillating amplitudes of the out-of-plane velocity v_z with the pressure waves leaked into the adjacent air, a fluid volume is modeled around the edge of the narrow specimen. Figure 5.17 shows the resulting contour plots. It is important to notice, that the color scale only refers to the out-of-plane velocity in the $z-$direction v_z and thus, only lines up with the vertically propagating pressure waves. Furthermore the color scale of v_z is not uniform in order to improve visibility. For the same reason a gray color interval is inserted at a value of 0 for both, acoustic pressure and v_z scaling.

The three boxes describe the fluid-solid interactions for each of the three Rayleigh wave-boundary interactions ("lag", "transition", "lead") shown above. The vertical projection of the magenta line ("oscillating amplitude"; see Figure 5.16) is sketched in the box of case 2 in Figure 5.17. The oscillating Rayleigh wavefront changes are directly mirrored in the oscillating leaked pressure wavefront changes in the form of a difference in height. For the "lag" seen in case 1 the height of a wavefront decreases towards the edges ($\Delta z < 0$) whereas the height increases towards the edges for case 3, the "lead" ($\Delta z > 0$). The "transition" seen in case 2 verifies the zero amplitude occasion (initial pressure $p_0 = 0$ Pa) and furthermore outlines a phase difference $\Delta\varphi$ of exactly π for pressure waves left and right of the 0.375 mm line.

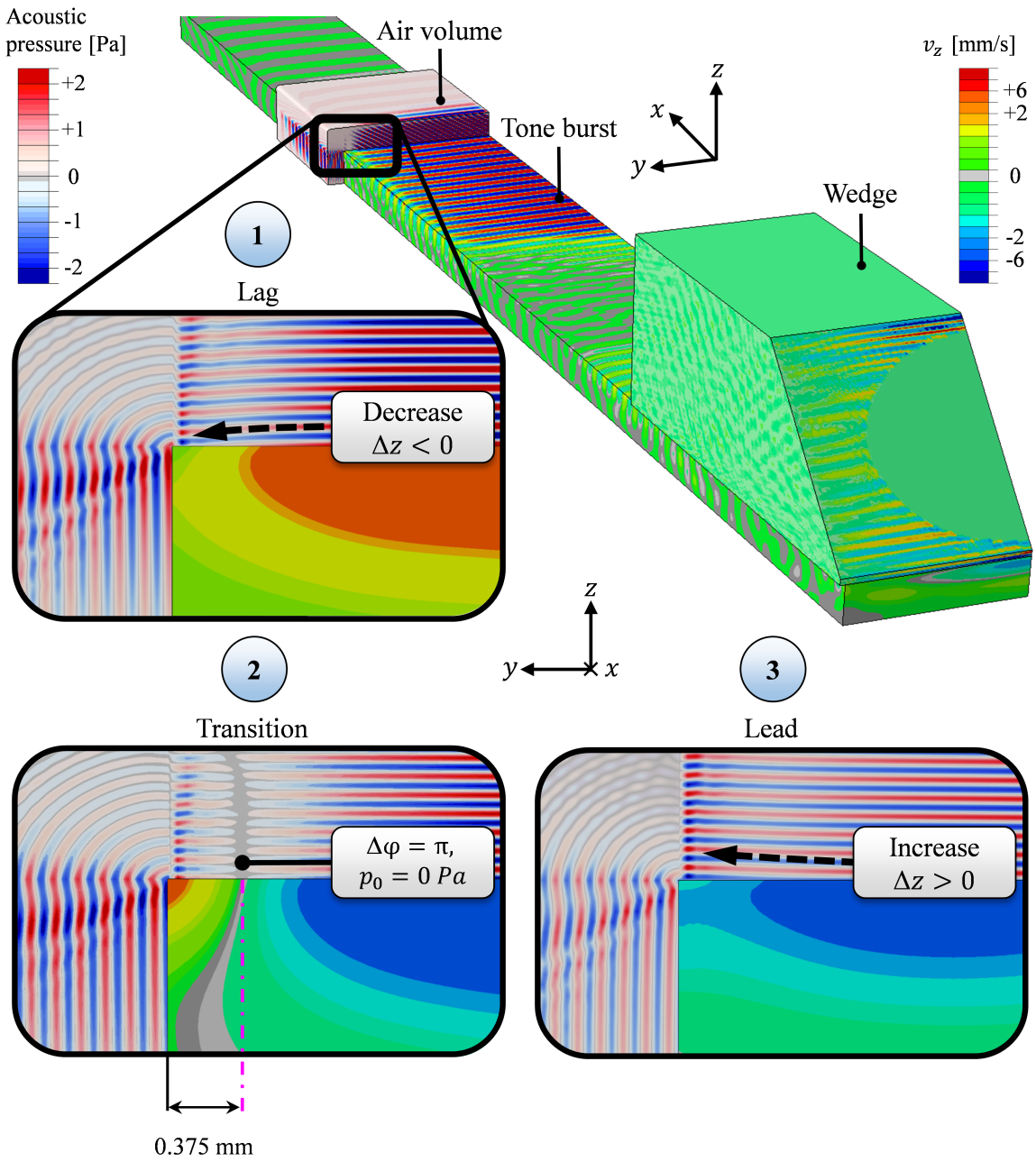

Figure 5.17: Oscillating pressure waves leaked into adjacent air in the case of the narrow width geometry

Referring to the color scale, there are still considerably high amplitudes of the acoustic sound pressure in the edge area with values above 1 Pa more than 10 % of the maximum pressure along the optical axis (see Section 5.1).

An additional phenomenon is pressure waves are also leaked in the $y-$direction which implies that there is an additional surface wave propagating along the lateral face. This effect was not further investigated in the present research.

Considering the sensitivity of high-frequency air coupled measurements (above 1 MHz) [7] (also stressed by the manufacturer [43]), disturbances in the leaked pressure field are assumed to influence the measurement quality. Although the active receiver surface (⌀12.5 mm) still has a distance of 3 mm to the edge. However, the edges of the "apparent opening" of the receiver (⌀17 mm; compare Figure 3.3) is very close the narrow specimen's boundaries. It is assumed that pressure waves arriving within that dimension still have an influence on the output signal of the air-coupled receiver [16]. The arrangement of the piezo sticks (compare the X-Ray in Figure 3.2) strengthen this assumption. Therefore the oscillating edge effects most likely impair the non-contact receiver signal output.

Chapter VI

CONCLUSION AND FUTURE WORK

6.1 Conclusion

This research demonstrates the development of a Finite Element (FE) model which simulates non-contact, air-coupled measurements of nonlinear Rayleigh waves. Findings from experiments conducted, especially diffraction and amplitude progression of the fundamental and second harmonic wave components, define parameters such as the hyperelastic constitutive law and the excitation source configuration which are implemented in the commercial FE-solver ABAQUS. The inherent properties of an air-coupled non-contact receiver are used to match experimental and numerical data. A MATLAB code is developed which considers frequency dependent pressure wave attenuation and averaged signal detection, based on output values of a coupled structural acoustic FE-analysis. This code shows that the technical features associated with the air-coupled receiver strongly influence the characteristic ratio A_2/A_1^2 and its slope over propagation distance, which is used to determine material nonlinearity in experiments. Accordingly, consideration of pressure wave attenuation and inherent averaging detection of the air-coupled receiver is of high importance if absolute nonlinear measurements are desired.

In the second part of this research, the experimentally validated FE-model is applied to a narrow specimen.This geometry causes an oscillating amplitude progression in both the first and second harmonic wave components in previous experimental research. The present investigation compares critical Rayleigh wave attributes observed in a narrow wave guide to an "infinite" width reference. This study shows that the constraining boundary significantly influences the Rayleigh wave propagation in the

entire sample. The amplitudes of the fundamental and second harmonic components decrease more rapidly at the center of the waveguide after a propagation distance of $\sim$ 50 mm. Furthermore, minor variations in the amplitude progression and the development of a double peak instead of the typical Gaussian profile characterize the deviating behavior. In addition, the spatial causality of the fundamental and generated second harmonic is affected at the edges of the narrow width geometry. Numerical results suggest that the boundary also influences the excited waves under the wedge because near field effects are more pronounced.

The restricting boundary hinders the wavefront expansion, which leads to an alternating change of Rayleigh wavefront shape. A recurring "attaching" and "releasing" interaction of the Rayleigh wave with the specimen's edges generates relative lags and leads along a single wavefront. This is associated with oscillating amplitudes near the boundary. These oscillations leak into the adjacent air and result in height differences of the pressure waves. Because the air-coupled receiver has a finite width comparable to that of the specimen, it is sensitive to edge effects which alter the observed signal. The accumulation of all the influences leads to severely affected Rayleigh waves in the solid and pressure waves in the air. Thus, the complexity of an already highly sensitive experimental procedure is aggravated by a narrow geometry, which adversely affects key factors needed for consistent measurement of material nonlinearity with an air-coupled, non-contact receiver.

6.2 Future Work

The numerical model in this research contains several simplifications and only considers perpendicular propagating waves excited by a symmetric source. However, experimental observations suggest that there are several unbalances that cannot be explained entirely. Moreover, the coupling of wedge and specimen most likely generates higher harmonics due to contact nonlinearities. Additionally, the nonlinearity of

the system and the source are only investigated superficially, promising an interesting field for further research. Unfortunately, increasing the complexity of the model generally increases the demand on computational resources, e.g. the simulation of an unsymmetrical model prevents application of a symmetry condition, doubling the model size.

Another extension might be to examine Rayleigh wave propagation in a non-planar geometry, such as "U-bend" samples. These specimens pose an upcoming research question in the NDE laboratory aiming to investigate stress corrosion cracking using nonlinear ultrasonic measurement techniques.

Appendix A

MODELING DETAILS

A.1 Element Description

This section describes the characteristics of the elements used in this research (as shown in Figure 4.3). Additionally the term reduced integration is defined.

Reduced Integration ABAQUS /Explicit element library mainly contains first order elements with reduced integration (with the exception of quadratic triangular and tetrahedral elements) [34]. Reduced integration refers to the use of lower order integration to form the element stiffness. This reduces the amount of time necessary to run the analysis but may have a negative effect on the accuracy of the solution for certain problems. The elements only have one Gauss point which can lead to hourglassing. Hourglassing describes the problem that a linear element with reduced integration can distort in a way, that the strains calculated at the integration point are all zero leading to an uncontrolled distortion of the mesh. Linear elements with reduced integration have hourglass control in ABAQUS, however it is recommended by the User's manual to use them in fine meshes only [39].

Acoustic Elements Acoustic elements are used to model an acoustic medium which undergoes small pressure changes. In an acoustic medium the solution is defined by a single pressure variable the acoustic sound pressure. This single degree of freedom is described by the ABAQUS output variable POR. Coupled acoustic structural elements (constrained to the surface) additionally have displacement degrees of freedom [38].

Infinite Elements In experimental measurements boundaries produce reflections which disturb results. Therefore measurements are usually taken at a sufficiently far distance from any boundaries. In order to simulate this distance in the reduced-size model, infinite elements are used to absorb waves arriving at the faces of the model. According to the ABAQUS User's Manual infinite elements provide quiet boundaries in dynamic analysis. In this type of analysis ABAQUS automatically adds viscous boundaries between finite-infinite element interface to better attenuate incident waves and avoid reflections [9]. However, present modeling results show, that there are still reflections if the simulated waves arrive at the "infinite" boundary. Especially the out-of-plane displacement underlies this effect. Therefore, sufficiently large run-off areas have to be provided, in order to prevent interference of reflected waves.

Since the infinite elements model the far field whose solution is assumed to be linear, only linear elastic material properties can be assigned. These have to match the material properties of the adjacent finite elements [40]. Therefore, a linear elastic element layer is included between the hyperelastic material (see Section 4.3.3.1) and the infinite elements. This prevents the rise of error messages during the analysis. The infinite elements require exact node numbering to calculate the element normal automatically and thus define the one-way infinite direction.

A.2 Coefficients of the Hyperelastic Material Model

This section describes the underlying equations of the hyperelastic material law implemented to model material nonlinearity. For nearly incompressible materials it is more convenient to express the strain energy density W_s as a function of isochoric invariants [3]. The deformation gradient without volume change is given as:

$$\bar{\mathbf{F}} \stackrel{def}{=} J^{-\frac{1}{3}}\mathbf{F} \tag{A.1}$$

which leads to the isochoric deviatoric strech matrix (left Cauchy-Green strain tensor):

$$\bar{\mathbf{B}} \stackrel{def}{=} \bar{\mathbf{F}}\bar{\mathbf{F}}^T. \tag{A.2}$$

The first (Equation (A.4)) and second (Equation(A.3)) isochoric invariants calculate to:

$$\bar{I_1} \stackrel{def}{=} trace(\bar{\mathbf{B}}). \tag{A.3}$$

$$\bar{I_2} \stackrel{def}{=} \frac{1}{2}(\bar{I_1}^2 - trace(\bar{\mathbf{B}}\bar{\mathbf{B}})). \tag{A.4}$$

These invariants enable the expression of the Cauchy stress tensor $\boldsymbol{\sigma}$ as the derivative of the strain energy density W_s according to Equation (A.5) [19], [3].

$$\boldsymbol{\sigma} = \frac{2}{J}\left[\frac{1}{J^{2/3}}\left(\frac{\partial Ws}{\partial \bar{I_1}} + \bar{I_1}\frac{\partial Ws}{\partial \bar{I_2}}\right)\bar{\mathbf{B}} - \frac{1}{3}\left(\bar{I_1}\frac{\partial Ws}{\partial \bar{I_1}} + 2\bar{I_2}\frac{\partial Ws}{\partial \bar{I_2}}\right)\boldsymbol{I} - \frac{1}{J^{4/3}}\frac{\partial Ws}{\partial \bar{I_2}}\bar{\mathbf{B}}\bar{\mathbf{B}}\right] + \frac{\partial Ws}{\partial J}\boldsymbol{I} \tag{A.5}$$

An accurate description of the theoretical background and further derivations can be found in [3], [35] and [19].

Appendix B

ADDITIONAL RESULTS

B.1 Source Nonlinearity

B.1.1 Source Properties

As mention in Section 2.2.2 it is to assume that the nonlinearity of the source (system, transducer, material) $\varphi_{0,2}^{T}$ influences nonlinear measurements, which is investigated in the following. A small portion of nonlinearity was introduced in the input signal. Since it is not possible to define two different prescribed displacements at the same node set, nonlinearity was included into the varying amplitude. Thereby it is assumed that the Gaussian source half width $a_{0,2}$ of the second harmonic component is half of the size of the Gaussian source half width a_0 of the fundamental component (compare [46]).

This assumption was implemented by dividing the transducer-wedge interface into four sections. To each of the resulting circles, a different excitation amplitude with varying nonlinear share is assigned. Thus, the assumed distribution is approximated by four cylinders as shown in Figure B.1. A similar approach is performed by Romer [29] for the fundamental harmonic in a 2D model. To investigate the phase influence, the initial phase $\varphi_{0,2}^{T}$ of the source nonlinearity is varied. Thereby the difference of first and second harmonic phase $\varphi_{0,1}^{T}$ and $\varphi_{0,2}^{T}$ in the input signal is adjusted according the extracted initial phase difference of the material $\varphi_{0,1}^{M}$ and $\varphi_{0,2}^{M}$ along the wedge tip, which is calculated from the DFT output. Simulations are performed for two cases:

1. Source nonlinearity is in phase with material nonlinearity $\varphi_{0,2}^{T} = \varphi_{0,2}^{M}$.
2. Source nonlinearity has opposite phase as material nonlinearity $\varphi_{0,2}^{T} - \pi = \varphi_{0,2}^{M}$.

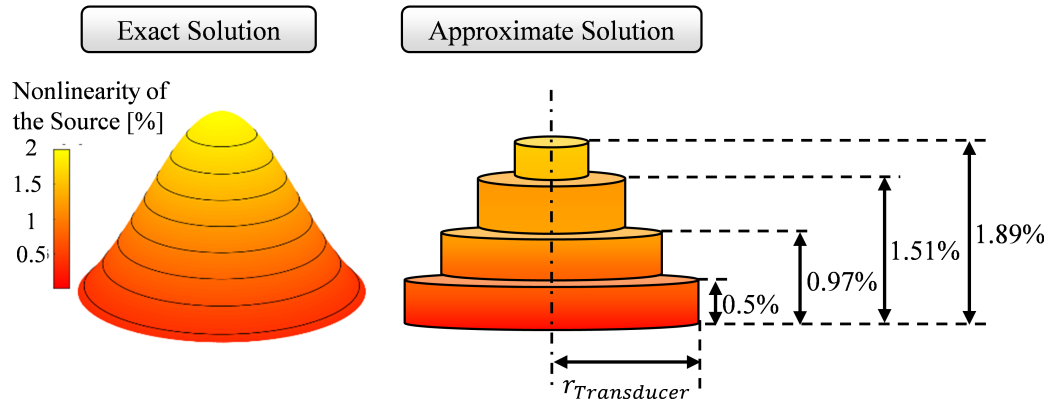

Figure B.1: Approximation of source nonlinearity (in percent of the fundamental amplitude)

B.1.2 Results

Figure B.2 shows the results of the simulations with additional source nonlinearity $v_{0,2}^T$. Both plots a) and b) refer to the legend in plot a). Part a) considers the amplitude progression of the second harmonic component along the propagation distance. Thereby, the blue curve is used as a reference showing the progression without additional source nonlinearity. Obviously the phase $\varphi_{0,2}^T$ plays an essential role in the consideration of the phenomenon. If the phase difference between fundamental and second harmonic matches with the phase difference of the material, nonlinearity adds up, whereby it is the other way around in the opposite case. With increasing propagation distance the curves approach each other nearly reaching the same values at the maximum distance considered. The influence of $v_{0,2}^T$ is higher if the phase differences match. The green (in phase) curve differs more significant from the reference (blue) than the opposite phase profile (red). In part b) the values along the wedge tip are given in order to investigate the simplification of the nonlinear line source as proposed by Torello [46]. The observations described above are even more pronounced in this plot. Not only the absolute values, but also the shape of the profile is influenced due to the modification of the input signal.

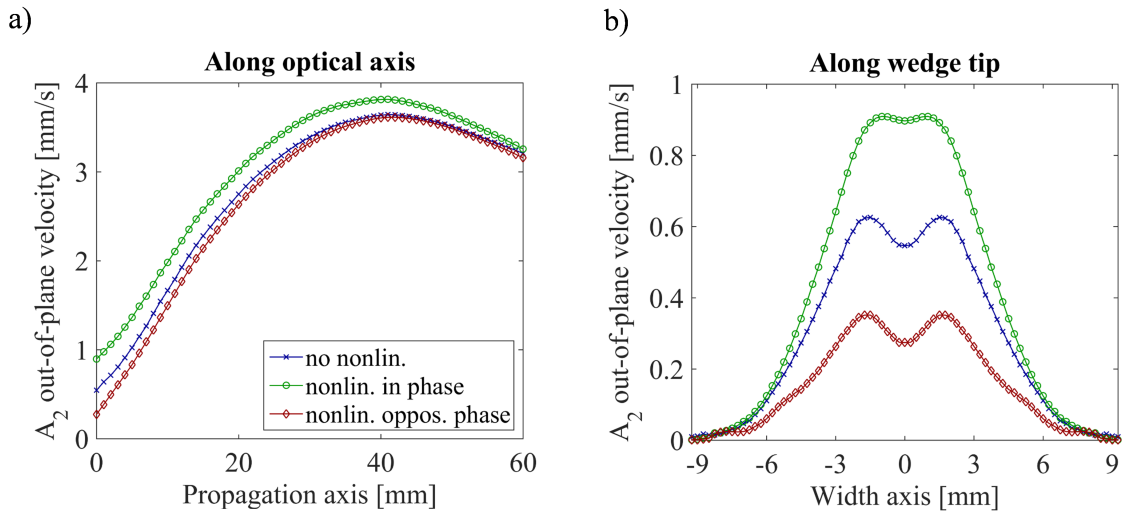

Figure B.2: Influence of source nonlinearity dependent on the initial phase difference of the fundamental and second harmonic component

The in phase case does only show a weak pronunciation of the double peak which is associated with the near field. This proves that the approximated Gaussian profile is added to the material nonlinearity. The opposite phase profile even shows a more distinctive double peak which further underlines the assumption. These results outline, that the consideration of phase difference is very important if it is tried to separate source nonlinearity from material nonlinearity in order to achieve absolute measurements.

However, source nonlinearity is not further considered in the main part of this research because there is only little knowledge about amplitude distribution and phase difference between first and second harmonic components. Thus, a lot of assumptions have to be made, modifying the output considerably. Furthermore a nonlinear signal, applied on the sloped surface of the wedge requires this model part to be meshed according to the second harmonic frequency (4.2 MHz), tremendously increasing the number of elements (compare Section 4.3.1). On top of that, the amplitude of second harmonic component only caused by the hyperelastic material under the wedge is already in the range of experimental values determined with a laser vibrometer [46].

REFERENCES

[1] Achenbach, J., *Wave Propagation in Elastic Solids.* Amsterdam: North-Holland Publishing Company, 1973.

[2] Bond, L., Chiang, C.-H., and Fortunko, C., "Absorption of ultrasonic waves in air at high frequencies (10-20 MHz)," *Acoustic Society of America*, vol. 92, no. 4, 1992.

[3] Bower, A. F., *Applied Mechanics of Solids.* Boca Raton: CRC Press, 2009.

[4] Cegla, F., "Energy concentration at the center of large aspect ratio rectangular waveguides at high frequencies," *Journal of the Acoustical Society of America*, vol. 123, no. 6, 2008.

[5] Datta, D. and Kishore, N. N., "Features of ultasonic wave propagation to identify defects in composite materials modelled by finite element method," *NDT&E International*, vol. 29, no. 4, pp. 213–223, 1996.

[6] Deighton, M., Gillespie, A., Pike, R., and Watkins, R., "Mode conversion of Rayleigh and Lamb waves to compression waves at a metal-liquid interface," *Ultrasonics*, pp. 249–258, 1981.

[7] Döring, D., *Luftgekoppelter Ultraschall und geführte Wellen für die Anwendung in der Zerstörungsfreien Werkstoffprüfung.* Dissertation, University of Stuttgart, Stuttgart, 2011.

[8] Gaal, M., "personal communication." QNDE Conference in Minneapolis, MN, July 2015.

[9] G.Kouroussis, Parys, L. V., Conti, C., and Verlinden, O., "Prediction of environmental vibrations induced by railway traffic using a three-dimensional dynamic finite element analysis," *Proceedings of the Thirteenth International Conference on Civil, Structural and Environmental Computing*, no. 7, 2001.

[10] Hamilton, M. F. and Blackstock, D. T., *Nonlinear Acoustics*. San Diego: Academic Press, 1998.

[11] Herrmann, J., Kim, J.-Y., Jacobs, L. J., Qu, J., Littles, J. W., and Savage, M. F., "Assessment of material damage in a nickel-base superalloy using nonlinear rayleigh surface waves," *Journal of Applied Physics*, vol. 99, no. 12, 2006.

[12] Hubenthal, M., *A Verification Study of ABAQUS AC3D8R Elements for Acoustic Wave Propagation*. Master's thesis, Rensselaer Polytechnic Institute, Hartford, 2010.

[13] Jacobsen, F. and Juhl, P., *Radiation of Sound*. Publication, Technical University of Denmark and University of Southern Denmark, 2011.

[14] Jakel, R., "Analysis of hyperelastic materials with Mechanica - theory and application examples," 2nd SAXSIM, April 2010.

[15] Jones, G. L. and Kobett, D. R., "Interaction of elastic waves in an isotropic solid," *Journal of the Acoustical Society of America*, vol. 235, no. 1, pp. 5–10, 1962.

[16] Kim, J.-Y., "personal communication." July 2015.

[17] Kim, J.-Y., "personal communication." May 2015.

[18] Kreutzbruck, M., "personal communication." QNDE Conference in Minneapolis, MN, July 2015.

[19] Lakes, R., *Strain Energy Density and Hyperelasticity.* BME 615 Tissue Biomechanics, lecture notes, University of Wisconsin, Madison, 2014.

[20] Lakocy, A., Lenhardt, E., and Uhrig, M., *Finite Element Modeling of Ultrasonic Rayleigh Surface Waves.* ME 6124 Finite-Element-Method, course project, Georgia Institute of Technology, Atlanta, 2015.

[21] Landau, L. D. and Lifshitz, E. M., *Theory of Elasticity, Course of Theoretical Physics.* Pergamon Press, 1970.

[22] Marino, D., *Using Nonlinear Ultrasound Measurements to Assess the Stage of Thermal Damage in Modified 9 %CR Ferritic Martensitic Steel.* Master's thesis, Georgia Institute of Technology, Atlanta, 2014.

[23] Morlock, F., *Evaluation of Stress Corrosion Cracking in Sensitized 304 Stainless Steel Using Nonlinear Rayleigh Waves.* Master's thesis, Georgia Institute of Technology, Atlanta, 2014.

[24] Morlock, M. B., *Nonlinear Mixing of Two Collinear Rayleigh Waves.* Master's thesis, Georgia Institute of Technology, Atlanta, 2013.

[25] Moser, F., Jacobs, L. J., and Qu, J., "Modeling elastic wave propagation in waveguides with the finite element method," *NDT&E International*, vol. 32, pp. 225–234, 1999.

[26] Norris, A., "Symmetry conditions for third order elastic moduli and implications in nonlinear wave theory," *Journal of Elasticity*, vol. 25, pp. 247–257, 1991.

[27] Nucera, C., *Propagation of Nonlinear Waves in Waveguides and Application to Nondestructive Stress Measurement.* Dissertation, University of California, San Diego, 2012.

[28] Pierce, A. D., *Acoustics, An Introduction to Its Physical Principles and Applications*. Acoustical Society of America, 1989.

[29] Romer, A., *The Second Harmonic Generation in Reflection Mode - an Analytical, Numerical and Experimental Study*. Master's thesis, University of Stuttgart, Stuttgart, 2014.

[30] Scott, K., "personal communication." February 2015.

[31] Shearer, P., *Introduction to Seismology, 2nd Edition*. New York: Cambridge University Press, 1999.

[32] Shull, D. J., Kim, E. E., Hamilton, M. F., and Zabolotskaya, E. A., "Diffraction effects in nonlinear Rayleigh wave beams," *Acoustical Society of America*, vol. 97, pp. 2126–2137, 1995.

[33] Simulia (Dassault Systems), Abaqus, "ABAQUS/Explict: Advanced topics, lecture 1, overview of ABAQUS/Explicit," 2005.

[34] Simulia (Dassault Systems), Abaqus, "ABAQUS/Explict: Advanced topics, lecture 2, elements," 2005.

[35] Simulia (Dassault Systems), Abaqus, "ABAQUS v6.7 analysis theory manual, section 4.6.1, hyperelastic material behavior," 2007.

[36] Simulia (Dassault Systems), Abaqus, "ABAQUS v6.7 analysis user's manual, section 17.5.1, hyperelastic behavior of rubberlike materials," 2007.

[37] Simulia (Dassault Systems), Abaqus, "ABAQUS v6.7 analysis user's manual, section 20.3.1, acoustic medium," 2007.

[38] Simulia (Dassault Systems), Abaqus, "ABAQUS v6.7 analysis user's manual, section 21.1.3, choosing the appropriate element for an analysis type," 2007.

[39] Simulia (Dassault Systems), Abaqus, "ABAQUS v6.7 analysis user's manual, section 22.1.1, solid (continuum) elements," 2007.

[40] Simulia (Dassault Systems), Abaqus, "ABAQUS v6.7 analysis user's manual, section 22.2.1, infinite elements," 2007.

[41] Simulia (Dassault Systems), Abaqus, "ABAQUS v6.7 analysis user's manual, section 6.1.1, procedures: overview," 2007.

[42] Simulia (Dassault Systems), Abaqus, "ABAQUS v6.7 analysis user's manual, section 6.9.1, acoustic, shock and coupled-acousitc-structural analysis," 2007.

[43] The Ultran Group, "Non-contact ultrasound (NCU) - phenomenally high efficiency transducers – 50 kHz to $>$ 5.0 MHz," 2015.

[44] Thiele, S., *Air-Coupled Detection of Rayleigh Surface Waves to Assess Material Nonlinearity Due to Precipitation in Alloy Steel.* Master's thesis, Georgia Institute of Technology, Atlanta, 2013.

[45] Thiele, S., Kim, J.-Y., Qu, J., and Jacobs, L. J., "Air-coupled detection of nonlinear Rayleigh surface waves to assess material nonlinearity," *Ultrasonics*, vol. 54, pp. 1470–1475, 2014.

[46] Torello, D., Thiele, S., Matlack, K. H., Kim, J.-Y., Qu, J., and Jacobs, L. J., "Diffraction, attenuation, and source corrections for nonlinear Rayleigh wave ultrasonic measurements," *Ultrasonics*, 2014.

[47] Viktorov, I., *Rayleigh and Lamb Waves: Physical Theory and Applications.* Plenum Press, 1967.

[48] Walker, S. V., Kim, J.-Y., Qu, J., and Jacobs, L. J., "Fatique damage evaluation in A36 steel using nonlinear rayleigh surface waves," *NDT&E International*, vol. 48, pp. 10–15, 2012.

[49] Zabolotskaya, E. A., "Nonlinear propagation of plane and circular Rayleigh waves in isotropic solids," *Acoustic Society of America*, vol. 91, no. 5, 1992.

[50] Zeitvogel, D. T., *Characterization of Damage due to Stress Corrosion Cracking in Carbon Steel Using Nonlinear Surface Acoustic Waves.* Master's thesis, Georgia Institute of Technology, Atlanta, 2012.